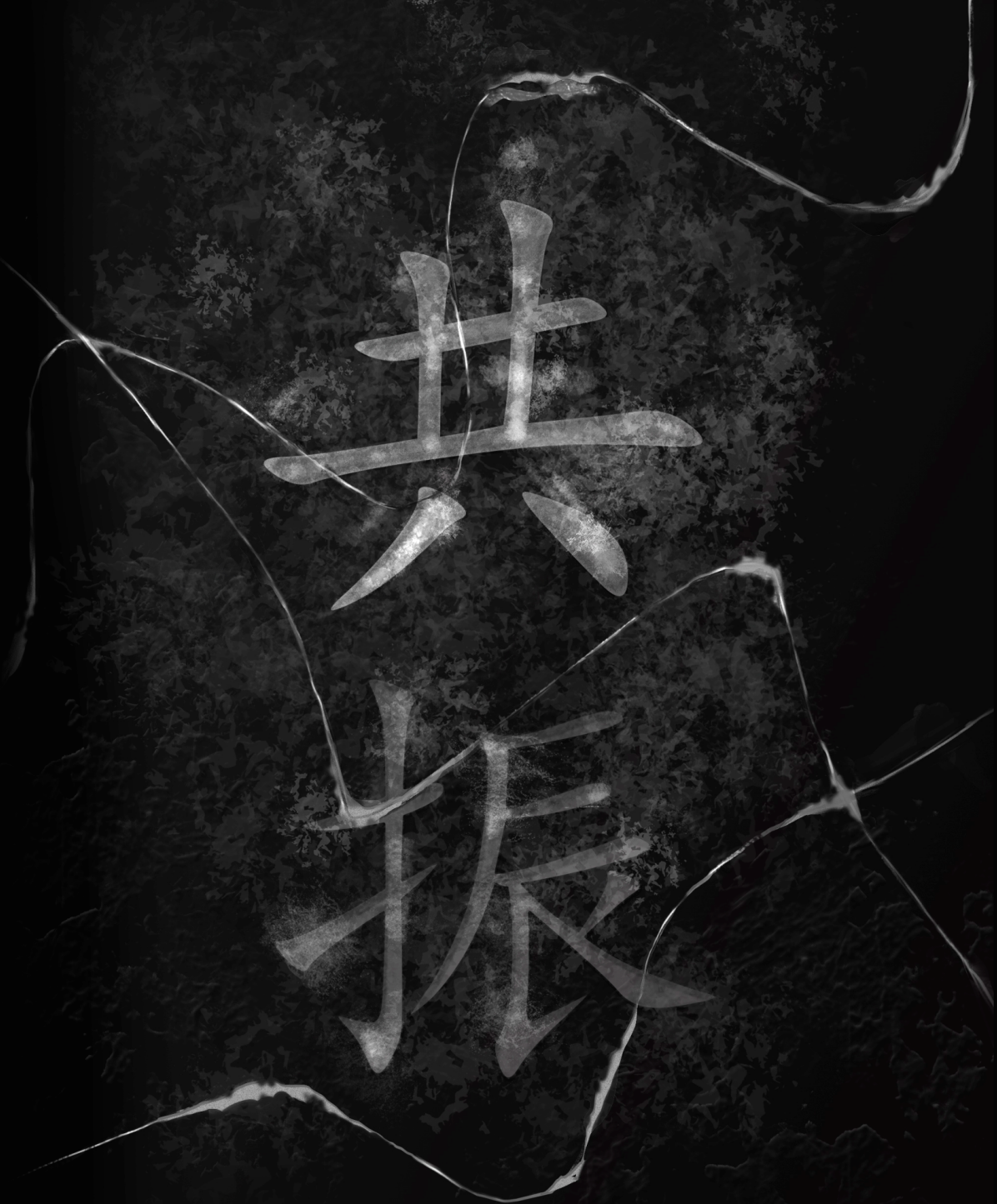


Control of Resonances in Photonic Crystal Waveguides



Jin Lian

CONTROL OF RESONANCES IN PHOTONIC CRYSTAL WAVEGUIDES

BEHEERSEN VAN RESONANTIES IN
FOTONISCHE KRISTAL
GOLFGELEIDERS

Promotiecommissie

Promotor Prof. Dr. A. P. Mosk

Overige leden Prof. Dr. K. J. Boller
Prof. Dr. C. Conti
Dr. A. De Rossi
Dr. E. Verhagen
Prof. Dr. W. L. Vos

The work described in this thesis is financially supported by the
'European Research Council' (ERC) grant 279248.

It was carried out at the
Complex Photonic Systems Group,
Department of Science and Technology
and MESA+ Institute for Nanotechnology,
University of Twente, P.O. Box 217,
7500 AE Enschede, The Netherlands.

and in part at *Debye Institute for Nanomaterials Science, Utrecht University.*

Cover: "Resonance" in Chinese

CONTROL OF RESONANCES IN PHOTONIC CRYSTAL WAVEGUIDES

PROEFSCHRIFT

ter verkrijging van
de graad van doctor aan de Universiteit Twente,
op gezag van de rector magnificus,
prof. dr. H. Brinksma,
volgens besluit van het College voor Promoties
in het openbaar te verdedigen
op woensdag 13 juli 2016 om 12.45 uur

door

Jin Lian

geboren op 16 juli 1987
te Baoji, China

Dit proefschrift is goedgekeurd door:

Prof. Dr. A. P. Mosk

Contents

1	Introduction	9
1.1	Photonic crystal waveguide	10
1.2	Mode gap cavity - intentional defect in photonic crystal waveguide	11
1.3	Unavoidable disorder in photonic crystal waveguide	12
1.4	Coupled resonator optical waveguide (CROW)	13
1.5	In this thesis	14
2	Multi-scale description of the coupled-cavity system	23
2.1	Introduction	23
2.2	Device-scale model of the CROW	24
2.2.1	Hamiltonian formalism	24
2.2.1.1	Two coupled cavities	24
2.2.1.2	CROW	25
2.2.2	Coupled mode formalism	25
2.2.2.1	Two coupled cavities	25
2.2.2.2	CROW	26
2.2.3	Summary	26
2.3	Calculation of the coupling factor	26
2.3.1	Field integral method	27
2.3.2	Direct numerical method	27
2.3.3	Bloch method	28
2.3.4	Comparison of three methods	29
2.4	Optimization of the optical delay and transmission of the CROW band	30
2.4.1	Time dependent coupled mode model of direct coupled CROW and waveguide systems	31
2.4.2	Optimization of the optical delay and transmission	33
2.5	Conclusion	34
3	Dispersion of coupled mode-gap cavities	37
3.1	Introduction	37
3.2	The physical cause of the asymmetric dispersion	39
3.3	Dispersive Mode (DM) model	41
3.4	Conclusion	44
4	Measurement of the profiles of disorder-induced localized resonances by local tuning	47
4.1	Introduction	47

4.2	Sample and Apparatus	48
4.3	Transmission spectra	49
4.4	Thermal profile and extracted intensity profile	50
4.5	Numerical Validation	52
4.6	Conclusion	54
5	Hybridization of disorder-induced localized modes in photonic crystal waveguides by adaptive tuning	59
5.1	Introduction	59
5.2	Sample and experimental setup	60
5.3	Extraction of the profiles of overlapping random modes	61
5.4	Reconstruction of the mode profiles of hybridized resonances	63
5.5	Conclusion	65
6	Fano lines of waveguide-cavities systems: measurements, modeling and manipulation of the Fano lineshapes	69
6.1	Introduction	69
6.2	Theoretical model	71
6.2.1	Process I: coupling between the measurement device and waveguide	71
6.2.2	Process II: propagation in the photonic crystal waveguide .	72
6.2.3	Process III: light coupling between the waveguides and cavities.	72
6.3	Experimental setup and reflection spectra	73
6.4	Analysis of reflection spectra	75
6.5	Direct manipulation of the Fano lineshape	77
6.6	Conclusion	78
7	Polarization conversion in photonic crystal cavities	81
7.1	Introduction	81
7.2	Experimental setup and transmission spectra	82
7.3	Physical processes of the system	83
7.4	Transfer matrices of the system	84
7.5	Analysis of experimental data	87
7.6	Conclusion	89
7.7	Appendix	89
8	Experimental demonstration of strong control of the Q factor of a disorder-induced resonance	95
8.1	Introduction	95
8.2	Sample and Experimental setup	97
8.3	Experimental results	98
8.4	Conclusion	102
8.5	Outlook	102
9	Summary	105

Algemene Nederlandse samenvatting	107
Dankwoord	109

CHAPTER 1

Introduction

The superposition of coherent waves in space results in interference phenomena. Most people must have seen the interference pattern caused by two ripples passing each other on the water in the lake or sea. Interference of waves in periodic structures is the interference among multiple scattered or reflected waves, and is a bit more complicated than when two water ripples meet each other. Nevertheless, the physics is the same. A fascinating feature of the interference in periodic structures is that waves in certain directions and within certain ranges of wavelengths cannot propagate since the reflected or scattered waves add up destructively. The well-known example of wave interference in periodic structure is the formation of the band structure of electrons in semiconductors [1]. Knowledge of the band structure of electron wave-packets enables people to control electrons in nanoscale devices, which has revolutionized our lives in recent decades [2]. Similarly, interference of photons in structures with periodically distributed refractive index with periodicities comparable to wavelengths of photons leads to the formation of band structures of photons. These structures are photonic crystals [3–5].

In photonic crystals, as in the electronic states in semiconductors, interference of waves forms Bloch modes [1]. Most amazingly, in some three dimensional photonic crystals, there are band gaps [6–10] which are ranges of photon frequency in which no mode exist in any propagating direction and with any polarization. This is similar to the band gap of a semiconductor, in which no state can be occupied. Thus, photonic crystals are the direct photonic analog of semiconductors [11].

Photonic crystals offer a wide range of opportunities to control the creation and propagation of light [12–17], and to accelerate the progress of realizing integrated photonic circuits with high efficiency nanolasers [18, 19], high capacity optical memories [20] and other fascinating functional components. Furthermore, a strong coupled cavity-quantum dots system is one of the candidates to be the basic unit of quantum networks [21, 22], and the realization of such systems in photonic crystals offers the possibility for on-chip quantum networks [23, 24].

Photonic crystal membrane structures are thin layers with periodic holes, in which the periodic distribution of refractive index is only in two dimension [5]. Due to their dimensionality limitation, instead of band gaps, they exhibit stop gaps which are ranges in frequency that light propagation is forbidden only in certain directions, and these stop gaps are for TE-like light¹. With the com-

¹The membrane structure dose not have continuous translation symmetry in the direction

bination of stop gaps and total internal reflection, photonic crystal membranes have a strong capability to control light. They are the most widely used photonic crystal structures, because of their excellent properties and the fact that they are much easier to fabricate compared to 3D photonic crystals. Many fancy components which are important for the optical quantum information processing, such as ultrahigh Q cavities [25–30], slow light waveguides [31–33], optical memories [20, 34] and microwatt threshold lasers [19], are implemented in photonic crystal membrane structures. The most amazing point is that all these components are in fact intentional defects in the photonic crystal membranes, which create modes in the stop gaps. This is analogous to semiconductor devices, since almost all functional semiconductor devices require dopants or other defects, which create states in energy gaps.

Photonic crystal waveguides (PhCWG) are line defects in photonic crystals [5], for instance they can be created by removing one row of the holes (Fig. 1.1(a)) in structures. In contrast to normal dielectric waveguides in which light is guided by the total internal reflection, PhCWG support modes which are guided by the stop gaps of the photonic crystal [5, 15, 32, 33]. Large group delay [32] and low loss at sharp bends [35] have been demonstrated in photonic crystal waveguides. Photonic crystal waveguides with intentional defects [28] and unavoidable disorder [36–39] exhibit high Q resonances. Single- and multi-resonance systems based on them are suitable for applications such as optical memories, delay lines [20, 40] and cavity QED [38]. Therefore, characterization, control and investigation of the optical properties of these resonances will pave the way to their applications. The aim of this thesis is to provide theories and models to explain the transmission, reflection and dispersion spectra of these resonances, and to develop experimental methods to probe and control these resonances.

In this chapter we first give a short introduction to the photonic crystal waveguides and all the resonances we study in this thesis. We then provide the overview of this thesis.

1.1 Photonic crystal waveguide

We show a schematic representation of a photonic crystal waveguide embedded in a membrane structure in Fig. 1.1(a). The membrane structure is usually made of semiconductor materials, since semiconductor materials usually have high refractive indices and low losses in the telecom wavelength at which functional devices of photonic crystals operate. In our experiments we use structures made of GaInP [41]. This material has two favorable properties. First, its band gap is very large (1.85 eV), as a result two-photon absorption is forbidden at the telecom wavelength in this material. Second, the thermal conductivity of this

perpendicular to the membrane. Therefore, the modes cannot be separated into TE (transverse electric) and TM (transverse magnetic) modes. However, a membrane structure does possess mirror symmetry in the direction perpendicular to the membrane. Using this symmetry, the modes in a photonic crystal membrane can be separated into TE-like modes of which most of the electric fields are parallel to the membrane and TM-like modes of which most of the magnetic fields are parallel to the membrane [5].

material is very low compared to other semiconductors, its value is $4.9 \text{ W}/(\text{m} \cdot \text{K})$. This is a great property for laser thermal tuning, since the ambient gas surrounding the membrane has a substantial influence the heat diffusion profile inside the membrane. Therefore, the temperature profile can be tailored by using different ambient gases [42]. The membrane structure shown in Fig. 1.1(a) has an air hole pattern in triangular lattice. The geometry opens up a stop gap for TE-like light. In the middle of the membrane, a line defect is introduced to create a waveguide. The band diagram of this waveguide calculated by the plane wave expansion method [43, 44] is shown in Fig. 1.1(b). In the diagram, there are three shaded parts. The purple triangle part is the light cone. Any mode inside the light cone cannot be confined by the total internal reflection (TIR) in the membrane, and it leaks out to the free space. The red part represents the bulk modes, they are photonic crystal modes. These modes are extended Bloch modes which are guided by TIR within the membrane. The yellow part is the stop gap. In the stop gap, no mode exist. Above the stop gap, we see a strongly dispersive mode which is flat at the boundary of the reduced Brillouin zone, it is the waveguide mode. In the direction perpendicular to the membrane, this mode is guided by the total internal reflection, and inside the membrane the mode is confined in the line defect by the stop gap. The flat dispersion at the band edge indicates the group velocity vanishes. The low group velocity close to the band edge is suitable for applications such as optical delay lines [32] and efficient single photon sources [45].

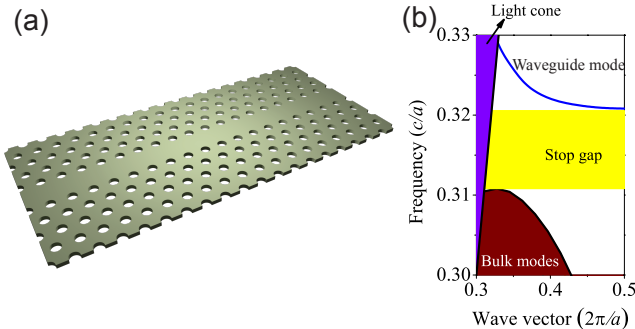


Figure 1.1: (a) Schematic representation of a photonic crystal waveguide embedded in a membrane structure. The parameters of the photonic crystal waveguide is the following. The lattice constant is $a = 485 \text{ nm}$, the radius of hole is $r = 0.28a$, the thickness h of the membrane is 180 nm , and the refractive index of the membrane is 3.17 . (b) Band diagram of TE-like light of a photonic crystal waveguide.

1.2 Mode gap cavity - intentional defect in photonic crystal waveguide

It is remarkable that a cavity resonance can be created by introducing intentional defects in a photonic crystal waveguide, this type of cavities is named as mode-

gap cavity [28, 46]. The first design [28] of the mode-gap cavity was made by E. Kuramochi *et al.*, and in this design they introduced tapered shifts of the holes around the waveguide [28]. The structure is shown in Fig. 2.1(a) and the mode field of this cavity is shown in Fig 2.2(b). We see that the field decays from the center to both sides of the waveguides.

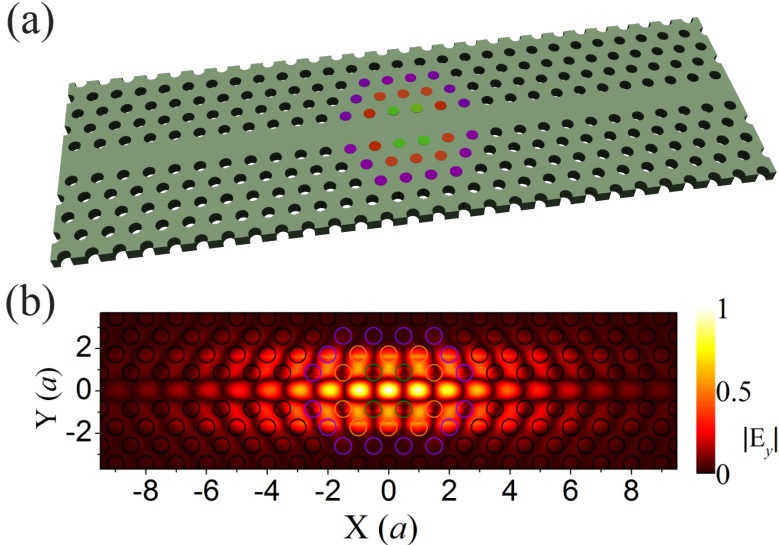


Figure 1.2: (a) Schematic representation of a mode-gap cavity. The colored holes indicate the holes that are shifted in a tapered way. (b) Amplitude of the y component of the electric field of the resonant mode in the mode-gap cavity calculated by the finite difference time domain (FDTD) method [47, 48]. It is normalized to the maximum of the field.

This type of cavity has a high quality factor (Q) and small mode volume which make it suitable for large scale integration [40, 49].

1.3 Unavoidable disorder in photonic crystal waveguide

One of the attractive properties of photonic crystal waveguides is the possibility of slow light propagation. However, there is an unavoidable limitation to this property, the unavoidable fabrication disorder [50, 51] (Fig. 1.3(a)). With the existence of the unavoidable disorder which are typically in the scale of few nanometer, light transport close to the band edge is suppressed and disorder-induced resonances form around the band edge [37]. An example of disorder-induced resonances in the band diagram is shown in Fig. 1.3(b). Due to their disordered nature, the frequency and spatial information of these resonances is not predictable. Remarkably, these resonances inherently have high quality

factors, and they are great platforms to study cavity QED [38] and adaptive filters [52].

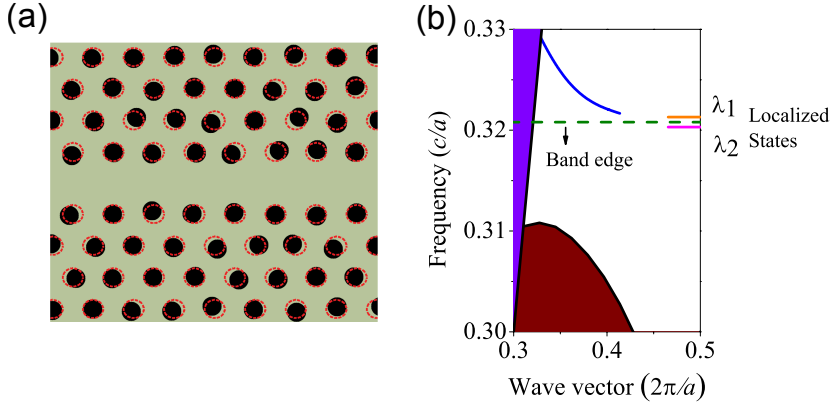


Figure 1.3: (a) Schematic representation of a photonic crystal with the position disorder. (b) Illustration of disorder-induced resonances in the band diagram, $\lambda_{1,2}$ indicate the localized states appearing around the waveguide band edge.

1.4 Coupled resonator optical waveguide (CROW)

A coupled resonator optical waveguide (CROW) is a linear chain of cavities [53]. In such a structure, light transport occurs via evanescent field coupling between the cavities [53, 54]. It has very promising applications as slow light devices[40, 55–58]. Among all types of CROW structure, CROWS composed of mode-gap cavities (Fig. 1.4) attract much interest [40, 49], since they are compact and low loss structures. Thus, to understand the dispersion of CROWS composed of mode-gap cavities is crucial for their applications.

The realization of a CROW structure requires high Q cavities [25–30, 59], this is very challenging due to the unavoidable fabrication disorder. Although a small amount of disorder does not noticeably influence the Q of each cavity especially for mode-gap cavities, it considerably shifts the resonant frequency of each cavity since the linewidth of each cavity is very narrow. As a consequence, the transmission of a CROW is suppressed tremendously. At the first glance, the slow light transport of a CROW and a photonic crystal waveguide have the same weakness that they are vulnerable to disorder. However, there is a huge difference from the point of view in restoring the functionality. The restoration of the slow light transport of a photonic crystal waveguide requires to counteract the exact fabrication disorder which is almost impossible to know. Whereas it is much simpler to restore the functionality of a CROW, since to shift the resonance of each cavity to the intended frequency does not require the knowledge of the microscopic distribution of the disorder. Thus, in the slow light application, adaptive CROWS are much more promising than photonic crystal waveguides.

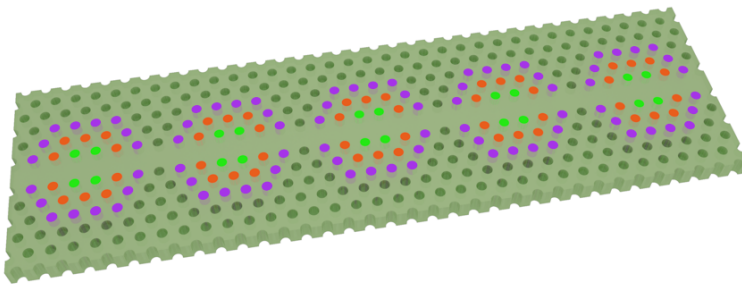


Figure 1.4: Schematic representation of a CROW structure composed of mode-gap cavities

1.5 In this thesis

In this thesis, an experimental, numerical and theoretical study of resonances in photonic crystal waveguides is presented. These resonances arise from intentional and unavoidable disorder. We study the coupling between these resonances and the interference between them and the environment. We also study how to probe and control the resonances arising from the inherently unavoidable disorder.

In chapter 2, we develop a detailed multi-scale description of the coupled cavities system. There are two levels of this description, device-scale modeling and microscopic modeling. At the device-scale, the coupled mode model [5, 60] is chosen for the modeling. At the microscopic level, the finite difference time domain (FDTD) [47, 48] method is used. The connection between these scales is the coupling factor. We perform the calculation of the coupling factor using three different methods and give a comprehensive comparison of these methods. Finally, we show an optimization procedure to obtain a flat transmission and smooth optical delay of a finite CROW with the help of a time dependent coupled model.

In chapter 3, we theoretically investigate the dispersion of a CROW made of photonic crystal mode-gap cavities. In the tight-binding approximation, the dispersion of a CROW is perfectly symmetric. However, a CROW composed of mode-gap cavities has a pronounced asymmetric dispersion. We show that the cavity mode profile is inherently dispersive, i.e., the mode wave function depends on the driving frequency and not the eigenfrequency, which is the fundamental cause of the asymmetric dispersion. This originates from the fact that the photonic crystal cavity resonances do not form a complete set. A dispersive mode coupling model that accurately describes the asymmetric dispersion is presented.

In chapter 4, we discuss a new method to elucidate the spatial profile of the localized modes in a photonic crystal waveguide with unavoidable disorder. In this method, we first use precise local tuning to obtain the wavelength shift of the resonance as a function of position. Secondly, using deconvolution with the known

thermal profile, we reconstruct the mode profiles of the disorder-induced modes. We present the result of the reconstruction of the spatial profile a localized mode with quality factor (Q) $> 10^5$ with a resolution of $2.5 \mu\text{m}$.

In chapter 5, our experimental result of the hybridization of disorder-induced localized modes in a photonic crystal waveguide are shown. The avoided crossing of two localized modes as a signature of full the hybridization of the modes is observed. Furthermore, we measure the mode profiles of the hybridized resonances.

In chapter 6, we analyze our reflection measurements of a waveguide-cavities system. The reflection spectra exhibit a set of asymmetric Fano lineshapes [61, 62] instead of symmetric Lorentzian lineshapes. We provide an analytical model to explain and reproduce the observed Fano lineshapes in the spectra. Based on our model, we propose and experimentally demonstrate a scheme to manipulate the Fano lineshape of the resonance.

In chapter 7, we investigate the polarization conversion in coupled photonic crystal cavity and waveguide systems. In such systems, light transmission is via the coupling between the cavity and the waveguides. When the coupling is asymmetric, one expects low transmission signal even on resonances. However, we experimentally observe a high transmission signal with an oscillating background. It is remarkable that this signal is TM-like light instead of TE-like light since theoretically the cavity resonance only supports the TE-like mode. We attribute this transmission to TE/TM conversion and present an effective model which successfully describes the physical processes and agrees with our experimental data. The importance of the analysis in this chapter is that it uncovers the fact that TE/TM conversion is a substantial loss channel of the cavity resonance, and it suggests that in the asymmetric coupling case, the transmission detection may be more efficient by addressing the cavity resonance with TM-like light.

In chapter 8, experimental results of the increase of the Q of a disorder-induced resonance by one order of magnitude are shown. This increase is achieved by introducing large refractive index change in the photonic crystal waveguide using thermal tuning. Experimentally, we observe the confinement of this mode in the transversal direction of the waveguide is increased as we increase the amplitude of the local index change.

Finally, in chapter 9, a brief summary of this thesis is given.

Bibliography

- [1] N. Ashcroft and N. Mermin, *Solid State Physics* (Saunders College, Philadelphia, 1976). — p.9.
- [2] Donald A. Neamen , *Semiconductor Physics And Devices: Basic Principles* (McGraw-Hill, New York, 2011). — p.9.
- [3] E. Yablonovitch, *Inhibited Spontaneous Emission in Solid-State Physics and Electronics*, Phys. Rev. Lett. **58**, 2059 (1987). — p.9.
- [4] S. John, *Strong localization of photons in certain disordered dielectric superlattices*, Phys. Rev. Lett. **58**, 2486 (1987). — p.9.
- [5] J. D. Joannopoulos, S. G. Johnson, J. N. Winn, and R. D. Meade , *Photonic Crystals: Molding the Flow of Light* (Princeton University Press, Princeton, 2008). — p.9, 10, 14.
- [6] E. Yablonovitch, T. Gmitter, and K. Leung, *Photonic band structure: The face-centered-cubic case employing nonspherical atoms*, Phys. Rev. Lett. **67**, 2295 (1991). — p.9.
- [7] K. M. Ho, C. T. Chan, and C. M. Soukoulis, *Existence of a photonic gap in periodic dielectric structures*, Phys. Rev. Lett. **65**, 3152 (1990). — p.9.
- [8] H. S. Sözüer and J. W. Haus, *Photonic bands: simple-cubic lattice*, JOSA B **10**, 296 (1993). — p.9.
- [9] K. M. Ho, C. T. Chan, C. M. Soukoulis, R. Biswas, and M. Sigalas, *Photonic band gaps in three dimensions: New layer-by-layer periodic structures*, Solid State Commun. **89**, 413 (1994). — p.9.
- [10] S. R. Huisman, R. V. Nair, L. A. Woldering, M. D. Leistikow, A. P. Mosk, and W. L. Vos, *Signature of a three-dimensional photonic band gap observed on silicon inverse woodpile photonic crystals*, Phys. Rev. B **83**, 205313 (2011). — p.9.
- [11] E. Yablonovitch, *Photonic Crystals: Semiconductors of Light*, Scientific American **285**, 46 (2001). — p.9.
- [12] P. Lodahl, A. Floris van Driel, I. S. Nikolaev, A. Irman, K. Overgaag, D. Vanmaekelbergh, and W. L. Vos, *Controlling the dynamics of spontaneous emission from quantum dots by photonic crystals*, Nature **430**, 654 (2004). — p.9.
- [13] M. D. Leistikow, A. P. Mosk, E. Yeganegi, S. R. Huisman, A. Lagendijk, and W. L. Vos, *Inhibited spontaneous emission of quantum dots observed in a 3D photonic band gap*, Phys. Rev. Lett **107**, 193903 (2011). — p.9.
- [14] D. Englund, D. Fattal, E. Waks, G. Solomon, B. Zhang, T. Nakaoka, Y. Arakawa, Y. Yamamoto, and J. Vucković, *Controlling the spontaneous emission rate of single quantum dots in a two-dimensional photonic crystal*, Phys.

- Rev. Lett. **95**, 2 (2005). — p.9.
- [15] S. McNab, N. Moll, and Y. Vlasov, *Ultra-low loss photonic integrated circuit with membrane-type photonic crystal waveguides*, Opt. Express **11**, 2927 (2003). — p.9, 10.
- [16] B. Corcoran, C. Monat, C. Grillet, D. J. Moss, B. J. Eggleton, T. P. White, L. O'Faolain, and T. F. Krauss, *Green light emission in silicon through slow-light enhanced third-harmonic generation in photonic-crystal waveguides*, Nat. Photonics **3**, 206 (2009). — p.9.
- [17] C. Conti, S. Trillo, and G. Assanto, *Energy localization in photonic crystals of a purely nonlinear origin*, Phys. Rev. Lett. **85**, 2502 (2000). — p.9.
- [18] P. Hamel, S. Haddadi, F. Rainieri, P. Monnier, G. Beaudoin, I. Sagnes, A. Levenson, and A. M. Yacomotti, *Spontaneous mirror-symmetry breaking in coupled photonic-crystal nanolasers*, Nat. Photonics **9**, 311 (2015). — p.9.
- [19] Y. Takahashi, Y. Inui, M. Chihara, T. Asano, R. Terawaki, and S. Noda, *A micrometre-scale Raman silicon laser with a microwatt threshold*, Nature **498**, 470 (2013). — p.9, 10.
- [20] E. Kuramochi, K. Nozaki, A. Shinya, K. Takeda, T. Sato, S. Matsuo, H. Taniyama, H. Sumikura, and M. Notomi, *Large-scale integration of wavelength-addressable all-optical memories on a photonic crystal chip*, Nat. Photonics **8**, 474 (2014). — p.9, 10.
- [21] H. J. Kimble, *The quantum internet*, Nature **453**, 1023 (2008). — p.9.
- [22] J. P. Reithmaier, G. Sek, A. Löffler, C. Hofmann, S. Kuhn, S. Reitzenstein, L. V. Keldysh, V. D. Kulakovskii, T. L. Reinecke, and A. Forchel, *Strong coupling in a single quantum dot-semiconductor microcavity system*, Nature **432**, 197 (2004). — p.9.
- [23] T. Yoshie, A. Scherer, J. Hendrickson, G. Khitrova, H. M. Gibbs, G. Rupper, C. Ell, O. B. Shchekin, and D. G. Deppe, *Vacuum Rabi splitting with a single quantum dot in a photonic crystal nanocavity*, Nature **432**, 9 (2004). — p.9.
- [24] A. Faraon, A. Majumdar, D. Englund, E. Kim, M. Bajcsy, and J. Vučković, *Integrated quantum optical networks based on quantum dots and photonic crystals*, New J. Phys **13**, 055025 (2011). — p.9.
- [25] K. J. Vahala, *Optical microcavities*, Nature **424**, 839 (2003). — p.10, 13.
- [26] Y. Akahane, T. Asano, and B.-S. Song, *High- Q photonic nanocavity in a two-dimensional photonic crystal*, Nature **425**, 944 (2003). — p.10, 13.
- [27] B.-S. Song, S. Noda, T. Asano, and Y. Akahane, *Ultra-high- Q photonic double-heterostructure nanocavity*, Nat. Mater. **4**, 207 (2005). — p.10, 13.
- [28] E. Kuramochi, M. Notomi, S. Mitsugi, A. Shinya, T. Tanabe, and T. Watanabe, *Ultrahigh- Q photonic crystal nanocavities realized by the local width modulation of a line defect*, Appl. Phys. Lett. **88**, 041112 (2006). — p.10, 12, 13.
- [29] T. Tanabe, M. Notomi, E. Kuramochi, A. Shinya, and H. Taniyama, *Trapping and delaying photons for one nanosecond in an ultrasmall high- Q photonic-crystal nanocavity*, Nature Photonics **1**, 49 (2007). — p.10, 13.
- [30] Y. Takahashi, H. Hagino, Y. Tanaka, T. Asano, and S. Noda, *High- Q photonic nanocavity with a 2-ns photon lifetime*, Conference on Quantum Electronics and Laser Science (QELS) - Technical Digest Series **15**, 17206 (2008).

- p.10, 13.
- [31] T. Baba, *Slow light in photonic crystals*, Nat. Photonics **2**, 465 (2008). — p.10.
- [32] M. Notomi, K. Yamada, A. Shinya, J. Takahashi, C. Takahashi, and I. Yokohama, *Extremely large group velocity dispersion of line-defect waveguides in photonic crystal slabs*, Phys. Rev. Lett. **87**, 253902 (2001). — p.10, 11.
- [33] T. F. Krauss, *Why do we need slow light?*, Nat. Photonics **2**, 448 (2008). — p.10.
- [34] T. Tanabe, M. Notomi, S. Mitsugi, A. Shinya, and E. Kuramochi, *Fast bistable all-optical switch and memory on a silicon photonic crystal on-chip*, Optics letters **30**, 2575 (2005). — p.10.
- [35] A. Mekis, J. Chen, I. Kurland, S. Fan, P. Villeneuve, and J. Joannopoulos, *High Transmission through Sharp Bends in Photonic Crystal Waveguides*, Phys. Rev. Lett. **77**, 3787 (1996). — p.10.
- [36] M. Patterson, S. Hughes, S. Combrié, N.-V.-Q. Tran, A. De Rossi, R. Gabet, and Y. Jaouën, *Disorder-Induced Coherent Scattering in Slow-Light Photonic Crystal Waveguides*, Phys. Rev. Lett. **102**, 253903 (2009). — p.10.
- [37] S. R. Huisman, G. Ctistis, S. Stobbe, A. P. Mosk, J. L. Herek, A. Lagendijk, P. Lodahl, W. L. Vos, and P. W. H. Pinkse, *Measurement of a band-edge tail in the density of states of a photonic-crystal waveguide*, Phys. Rev. B **86**, 155154 (2012). — p.10, 12.
- [38] L. Sapienza, H. Thyrrstrup, S. R. Stobbe, P. D. Garcia, S. Smolka, and P. Lodahl, *Cavity quantum electrodynamics with Anderson-Localized Modes*, Science **1027**, 1352 (2010). — p.10, 13.
- [39] R. Faggiani, R. Baron, X. Zang, L. Lalouat, S. A. Schulz, K. Vynck, B. Regan, B. Cluzel, F. De Fornel, T. F. Krauss, and P. Lalanne, *Lower bound for the spatial extent of localized modes in photonic-crystal waveguides with small random imperfections*, Sci Rep. **6**, 27037 (2016). — p.10.
- [40] M. Notomi, E. Kuramochi, and T. Tanabe, *Large-scale arrays of ultrahigh-Q coupled nanocavities*, Nat. Photonics **2**, 741 (2008). — p.10, 12, 13.
- [41] S. Combrié, Q. V. Tran, A. De Rossi, C. Husko, and P. Colman, *High quality GaInP nonlinear photonic crystals with minimized nonlinear absorption*, Appl. Phys. Lett. **95**, 221108 (2009). — p.10.
- [42] S. Sokolov, J. Lian, E. Yüce, S. Combrié, G. Lehoucq, A. De Rossi, and A. P. Mosk, *Local thermal resonance control of GaInP photonic crystal membrane cavities using ambient gas cooling*, Appl. Phys. Lett. **106**, 171113 (2015). — p.11.
- [43] P. T. Leung, S. Y. Liu, S. S. Tong, and K. Young, *Time-independent perturbation theory for quasinormal modes in leaky optical cavities*, Phys. Rev. A **49**, 3068 (1994). — p.11.
- [44] S. G. Johnson and J. D. Joannopoulos, *Block-iterative frequency-domain methods for Maxwell's equations in a planewave basis*, Opt. Express **8**, 173 (2001). — p.11.
- [45] T. Lund-Hansen, S. Stobbe, B. Julsgaard, H. Thyrrstrup, T. Sünder, M. Kamp, A. Forchel, and P. Lodahl, *Experimental Realization of Highly Efficient Broadband Coupling of Single Quantum Dots to a Photonic Crystal*

- Waveguide, Phys. Rev. Lett. **101**, 113903 (2008). — p.11.
- [46] M. Notomi and H. Taniyama, *On-demand ultrahigh-Q cavity formation and photon pinning via dynamic waveguide tuning*, Opt. Express **16**, 18657 (2008). — p.12.
- [47] A. F. Oskooi, D. Roundy, M. Ibanescu, P. Bermel, J. Joannopoulos, and S. G. Johnson, *Meep: A flexible free-software package for electromagnetic simulations by the FDTD method*, Comput. Phys. Commun. **181**, 687 (2010). — p.12, 14.
- [48] A. Taflove and S. C. Hagness, *Computational Electrodynamics: The Finite-Difference Time-Domain Method, Third Edition* (Artech House, Boston, 2005). — p.12, 14.
- [49] N. Matsuda, E. Kuramochi, H. Takesue, and M. Notomi, *Dispersion and light transport characteristics of large-scale photonic-crystal coupled nanocavity arrays*, Opt. Lett. **39**, 2290 (2014). — p.12, 13.
- [50] A. F. Koenderink, A. Lagendijk, and W. L. Vos, *Optical extinction due to intrinsic structural variations of photonic crystals*, Phys. Rev. B **72**, 153102 (2005). — p.12.
- [51] S. Hughes, L. Ramunno, J. F. Young, and J. E. Sipe, *Extrinsic optical scattering loss in photonic crystal waveguides: Role of fabrication disorder and photon group velocity*, Phys. Rev. Lett. **94**, 033903 (2005). — p.12.
- [52] S. Fan, P. Villeneuve, J. Joannopoulos, and H. Haus, *Channel drop filters in photonic crystals*, Opt. Express **3**, 4489 (1998). — p.13.
- [53] A. Yariv, Y. Xu, R. K. Lee, and A. Scherer, *Coupled-resonator optical waveguide: a proposal and analysis*, Opt. Lett. **24**, 711 (1999). — p.13.
- [54] M. J. Hartmann, F. G. S. L. Brandão, and M. B. Plenio, *Quantum many-body phenomena in coupled cavity arrays*, Laser Photon. Rev. **2**, 527 (2008). — p.13.
- [55] C. Taddei, L. Zhuang, M. Hoekman, A. Leinse, R. Oldenbeuving, P. van Dijk, and C. Roeloffzen, in *Microwave photonics (mwp) and the 2014 9th asia-pacific microwave photonics conference (apmp) 2014 international topical meeting on* (IEEE, Sendai, 2014), pp. 44–47. — p.13.
- [56] C. Taddei, L. Zhuang, M. Hoekman, C. Roeloffzen, and K.-J. Boller, in *2015 european conference on lasers and electro-optics - european quantum electronics conference* (Optical Society of America, Munich, 2015). — p.13.
- [57] M. L. Cooper, G. Gupta, M. A. Schneider, W. M. J. Green, S. Assefa, F. Xia, Y. A. Vlasov, and S. Mookherjea, *Statistics of light transport in 235-ring silicon coupled-resonator optical waveguides*, Opt. Express **18**, 26505 (2010). — p.13.
- [58] F. Xia, L. Sekaric, and Y. Vlasov, *Ultracompact optical buffers on a silicon chip*, Nat. Photonics **1**, 65 (2007). — p.13.
- [59] E. Verhagen, S. Deléglise, S. Weis, A. Schliesser, and T. J. Kippenberg, *Quantum-coherent coupling of a mechanical oscillator to an optical cavity mode*, Nature **482**, 63 (2012). — p.13.
- [60] H. A. Haus and W. Huang, *Coupled-mode theory*, Proc. IEEE **79**, 1505 (1991). — p.14.
- [61] U. Fano, *Effects of configuration interaction on intensities and phase shifts*,

- Physical Review **124**, 1866 (1961). — p.15.
- [62] A. E. Miroshnichenko, S. Flach, and Y. S. Kivshar, *Fano resonances in nanoscale structures*, Rev. Mod. Phys. **82**, 2257 (2010). — p.15.

CHAPTER 2

Multi-scale description of the coupled-cavity system

2.1 Introduction

In this chapter, we present a detailed multi-scale description of the system of coupled cavities. In applications, the most well known example of a coupled cavity system is the coupled resonator optical waveguide (CROW) [1], in which case the coupled cavities are arranged in one dimension. Many fancy devices based on CROWs have been proposed and demonstrated experimentally such as optical delay lines [2–4] and optical memory [5]. CROWs are typically analyzed in the tight binding (TB) approximation [1, 6, 7], which assumes the basis wave functions of each cavity are tightly confined, and the overlap of the eigen wave functions between neighboring cavities causes coupling between the cavities. In this approximation, the Hamiltonian of coupled cavities is similar to the Hubbard model [8] which is of fundamental importance in condensed matter physics. Many intriguing concepts from the condensed matter physics have been imported to the coupled cavities systems such as artificial gauge fields and quantum hall effects [9–11]. These bring new opportunities to control light transport in different ways.

Ideally the optical properties of coupled cavity systems, such as dispersion, transmission and group delay, can be calculated from first principles numerically. However, due to the fact that systems of coupled cavities are generally complicated and with relative big systems sizes [2], direct simulation of field equations on the coupled cavities is difficult and time consuming. Thus we choose a multi-scale modeling approach in which we use a widely used coupled mode model [1, 12–14] for the device-scale ($10 \mu\text{m}$ to $< 1\text{mm}$) modeling, then evaluate the key parameters by microscopic numerical modeling. We explore three different methods [1, 12] to evaluate the coupling factor that connects the device-scale modeling in terms of coupled resonances and the microscopic modeling of field equations.

This chapter is organized as follows. In Sec. 2.2, we introduce a semi-analytic physical model [1, 7, 12] of coupled cavities using two coupled cavities and one dimensional coupled-cavity system as examples. In Sec. 2.3, we discuss the physical meaning of the coupling factor and explore the methods to calculate it. In Sec. 2.4, we extend the physical model to systems composed of a finite number of cavities coupled to input and output waveguides. Using the extended model, we investigate the optimization of the optical delay and transmission of the CROW band.

2.2 Device-scale model of the CROW

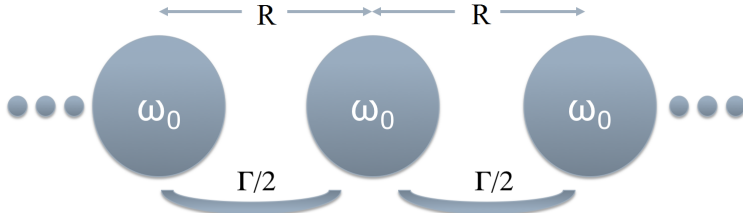


Figure 2.1: Schematic representation of a CROW structure. Each round disc in the graph represents a cavity with frequency ω_0 , and the coupling rate is Γ . Here R indicates the heart to heart distance between the cavities.

In Fig. 2.1, we schematically represent a CROW with cavity resonance frequency ω_0 and coupling constant $\Gamma/2$. This coupling constant describes how strongly the cavities interact with each other and Γ is the coupling rate (only nearest neighbor coupling is considered here). There are two equivalent formalisms [12, 15] to describe this model which we briefly discuss in the following paragraphs.

2.2.1 Hamiltonian formalism

The Hamiltonian formalism is one of the most used formalism for coupled cavities, since it gives direct analog between coupled cavities and electronic systems in condensed matter physics.

2.2.1.1 Two coupled cavities

We first write the Hamiltonian of a two coupled cavities system. It is

$$\mathcal{H} = \sum_{i=1,2} \omega_0 |\varphi_i\rangle \langle \varphi_i| + \Gamma/2 (|\varphi_1\rangle \langle \varphi_2| + |\varphi_2\rangle \langle \varphi_1|). \quad (2.1)$$

In Eq. (2.1), φ_1 and φ_2 are the eigen wave function of the cavity 1 and cavity 2 respectively. It is assumed that φ_1 and φ_2 are orthogonal and complete [16], which means

$$\begin{cases} \langle \varphi_i | \varphi_j \rangle = \delta_{i,j} \\ \sum_{i=1,2} |\varphi_i\rangle \langle \varphi_i| = \mathbb{1} \end{cases} \quad (2.2)$$

Using $|\varphi\rangle_{\pm} = \frac{1}{\sqrt{2}}(|\varphi\rangle_1 \pm |\varphi\rangle_2)$ to diagonalize the Hamiltonian, we obtain the eigen values of the coupled system, they are $\omega_0 \pm \Gamma/2$. Here $|\varphi\rangle_{\pm} = \frac{1}{\sqrt{2}}(|\varphi\rangle_1 \pm |\varphi\rangle_2)$ are the hybridized modes of the system, where $|\varphi\rangle_+$ is the symmetric mode, $|\varphi\rangle_-$ is the anti-symmetric mode.

2.2.1.2 CROW

For a CROW structure, the Hamiltonian of the system is the following,

$$\mathcal{H} = \sum_m \omega_0 |\varphi_m\rangle \langle \varphi_m| + \sum_m \Gamma/2 (|\varphi_{m+1}\rangle \langle \phi_m| + |\varphi_m\rangle \langle \varphi_{m+1}|). \quad (2.3)$$

Similar to two coupled cavities, the set φ_i should fulfill the orthogonality and completeness conditions. Using $\varphi_k = \frac{1}{\sqrt{N}} \sum_m e^{-ikmR} \varphi_m$ to diagonalize the Hamiltonian, we obtain the band structure of the CROW,

$$\omega_k = \omega_0 + \Gamma \cos(kR). \quad (2.4)$$

Here, k is the Bloch wave vector, R is the distance between nearby cavities. This is equivalent to the result in [1] for an offset parameter of zero.

2.2.2 Coupled mode formalism

In the simplest form, the Hamiltonian formalism is restricted to closed systems. Its generalization to open system is very subtle. In comparison, the coupled mode [12] formalism which is another widely used formalism has a relative simple form, and can easily be extended to open systems, such as coupled cavities which are optically connected to waveguides.

2.2.2.1 Two coupled cavities

We first write the coupled equation of motion of a two coupled cavities system. It is [12]

$$\begin{cases} \frac{da_1(t)}{dt} = i\omega_0 a_1(t) + i\frac{1}{2}\Gamma a_2(t) \\ \frac{da_2(t)}{dt} = i\omega_0 a_2(t) + i\frac{1}{2}\Gamma a_1(t) \end{cases}. \quad (2.5)$$

Here $a_j(t)$ ($j = 1, 2$) describes the time evolution of the amplitude of the mode in cavity j . By Fourier transforming Eq. (2.5), we obtain

$$\begin{cases} i\omega A_1(\omega) = i\omega_0 A_1(\omega) + i\frac{1}{2}\Gamma A_2(\omega) \\ i\omega A_2(\omega) = i\omega_0 A_2(\omega) + i\frac{1}{2}\Gamma A_1(\omega) \end{cases}. \quad (2.6)$$

It is easy to find out that the condition that Eqs. (2.6) has solutions is that the value of ω should be

$$\omega_{\pm} = \omega_0 \pm |\Gamma|/2. \quad (2.7)$$

The solutions correspond to the frequency of the symmetric and anti-symmetric modes of the system. We choose the the eigen functions of the two cavities to be related by a pure translation $\mathbf{E}_1(\mathbf{r}) = \mathbf{E}_2(\mathbf{R} + \mathbf{r})$. Here $\mathbf{E}_1(\mathbf{r})$ and $\mathbf{E}_2(\mathbf{r})$ are the spatial profiles of the mode in cavity 1 and cavity 2. With this choice, when $\Gamma < 0$, ω_+ is the frequency of the anti-symmetric mode. In Ref. 1, the value of Γ is selected as a negative value.

2.2.2.2 CROW

For a CROW structure, we can write coupled equation as the following,

$$\frac{da_n(t)}{dt} = i\omega_0 a_n(t) + i\frac{1}{2}\Gamma a_{n-1}(t) + i\frac{1}{2}\Gamma a_{n+1}(t). \quad (2.8)$$

Here $a_n(t)$ describes the time evolution of the amplitude of the mode in cavity n .

For a infinite CROW, it has discrete translation symmetry. Therefore, according to Bloch theorem, we know the following phase relation,

$$a_{n+1}(t)e^{ikR} = a_n(t) = a_{n-1}(t)e^{-ikR}. \quad (2.9)$$

Using Eq. (2.9) combined with Eq. (2.8), the dispersion of CROW can be found as $\omega_k = \omega_0 + \Gamma \cos(kR)$, which is the same as Eq. (2.5).

2.2.3 Summary

We have used two different formalisms to obtain the eigen values of two coupled systems and the dispersion of CROWS, both of the formalisms lead to same results. Furthermore, both formalisms can be extended to higher-dimensional coupled cavities systems. In the following, we use the coupled mode formalism, as it is easier to extend to open systems.

2.3 Calculation of the coupling factor

In the physical model, we see there are two parameters, the intrinsic frequency of the cavity ω_0 and the coupling rate Γ . Now we introduce a dimensionless coupling factor which links these two parameters together. It is defined as

$$\kappa = \frac{\Gamma}{\omega_0}. \quad (2.10)$$

We now use the two coupled cavities system to explain the physical meaning of the coupling factor. Suppose we launch a mode to the two coupled systems, the mode is expressed as

$$\mathbf{E}_{\text{two}}(\mathbf{r}, t) = \mathbf{E}_s(\mathbf{r})e^{i\omega_- t} + \mathbf{E}_a(\mathbf{r})e^{i\omega_+ t}. \quad (2.11)$$

Here $\mathbf{E}_s(\mathbf{r}) = \mathbf{E}(\mathbf{r}) + \mathbf{E}(\mathbf{R} - \mathbf{r})$ and $\mathbf{E}_a(\mathbf{r}) = \mathbf{E}(\mathbf{r}) - \mathbf{E}(\mathbf{R} - \mathbf{r})$ are spatial distribution of the fields of symmetric and anti-symmetric modes. $\mathbf{E}(\mathbf{r})$ and $\mathbf{E}(\mathbf{R} - \mathbf{r})$ are the spatial components of the mode in cavity 1 and 2 respectively. At $t_0 = 0$, $\mathbf{E}_{\text{two}} = 2\mathbf{E}(\mathbf{r})$ which means the field is in the cavity 1. It is easy to notice at $t_1 = 2\pi/|\Gamma|$, $\mathbf{E}_{\text{two}} = 2e^{i\omega_- \frac{2\pi}{\Gamma}} \mathbf{E}(\mathbf{R} - \mathbf{r})$, which means the field is in the cavity 2 now. Obviously, the number of optical cycles N for energy to transfer from cavity 1 to 2 is

$$N = \frac{t_1 - t_0}{T_0} = \frac{\omega_0}{|\Gamma|}. \quad (2.12)$$

Here $T_0 = 2\pi/\omega_0$ is the period of one optical cycle of a single cavity. Thus, the physical meaning of κ is that the inverse of $|\kappa|$ is the number of optical cycles for energy to transfer from one cavity to another.

In the following, we show how we obtain the value of coupling factor κ for coupled mode-gap cavities [17] from microscopic numerical calculations. The numerical calculations are carried out using three different methods, and their results are compared.

2.3.1 Field integral method

The first method we use to calculate κ is the field integral method. From Maxwell's equations, there is an analytic expression of the coupling factor [1, 12],

$$\kappa = \frac{\int \delta\epsilon(\mathbf{r} - \mathbf{R}) \mathbf{E}(\mathbf{r} - \mathbf{R}) \cdot \mathbf{E}(\mathbf{r}) d\mathbf{r}}{\int \epsilon(\mathbf{r}) \mathbf{E}(\mathbf{r}) \cdot \mathbf{E}(\mathbf{r}) d\mathbf{r}}. \quad (2.13)$$

In Eq. (2.13), $\mathbf{E}(\mathbf{r})$ is the electric field of the resonant mode of the isolated single cavity, $\epsilon(\mathbf{r})$ is the dielectric function of a single cavity and $\delta\epsilon(\mathbf{r} - \mathbf{R})$ is the difference in dielectric function between one isolated cavity and two cavities with heart to heart distance \mathbf{R} . From Eq. (2.13), it is seen that analytically the coupling factor can be obtained if the electric field of the resonant mode of a single cavity is known. Using finite difference time domain (FDTD) method [18, 19], we calculate the electric field of a single mode-gap cavity (Fig. 2.2), and with the help of Eq. (2.13) we obtain the coupling factors for various distances, shown in Fig. 2.5.

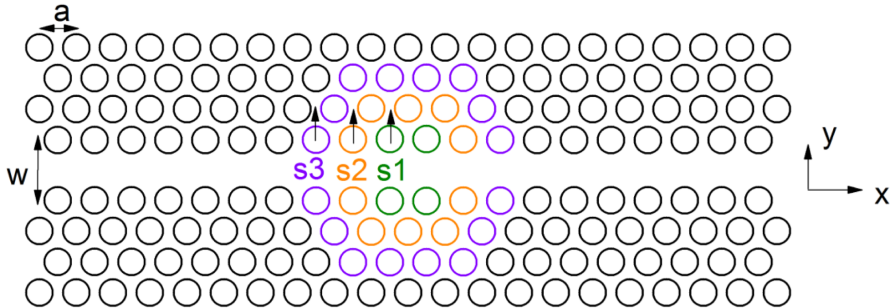


Figure 2.2: Schematic representation of the mode-gap cavity. The parameters are the following. The lattice constant is $a = 485$ nm, radius of the holes is $r = 0.25a$, the width of the waveguide w is $0.98\sqrt{3}$, the thickness of the membrane is $h = 180$ nm and refractive index of the material is $n = 3.17$. The shifting distance of green, orange and purple holes are $s_1=0.0124\sqrt{3}$, $s_2=2/3 s_1$, $s_3=1/3 s_1$ respectively.

2.3.2 Direct numerical method

The second method is the direct numerical method. For two coupled cavities, we can express the coupling rate as $|\Gamma| = |\omega_- - \omega_+|$. Thus the coupling factor can

be written as

$$|\kappa| = \frac{|\omega_- - \omega_+|}{\omega_0}. \quad (2.14)$$

From Eq. (2.14), we know we need intrinsic resonant frequency of the single cavity ω_0 and the intrinsic resonant frequency ω_{\pm} of the modes of a two coupled mode-gap cavities (Fig. 2.3) to calculate the coupling factor.

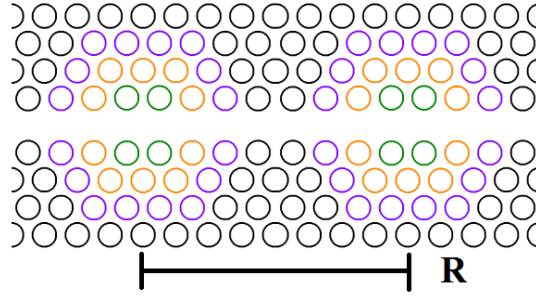


Figure 2.3: Schematic representation of a system consisted of two mode-gap cavities, the heart to heart distance is R .

We use the FDTD method [18] to calculate the needed intrinsic frequencies. ω_0 is calculated from the structure shown in Fig. 2.2, ω_{\pm} is calculated from the structure shown in Fig. 2.3. The results are shown in Fig. 2.5.

2.3.3 Bloch method

The third method we use is the Bloch method. In Sec. II, we have derived the dispersion of a CROW structure which is Eq. (2.5). From this, we can express the coupling factor as

$$|\kappa| = \frac{|\omega_k(kR = 0) - \omega_k(kR = \pi)|}{2\omega_0}. \quad (2.15)$$

Eq. (2.15) tells us the coupling factor κ can be calculated with the help of a super cell with the Bloch periodic boundary [6]. The sketch of the super cell is shown in Fig. 2.4. The super cell is very similar to the structure in Fig. 2.1, except it is truncated to length R , and Bloch boundary conditions are applied.

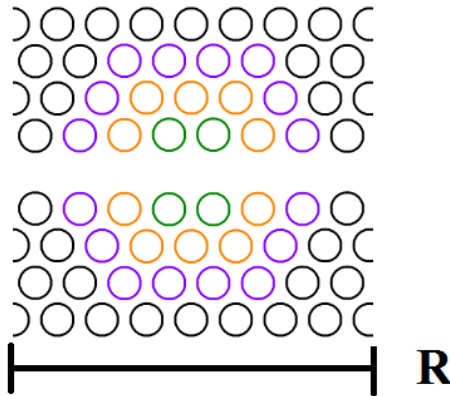


Figure 2.4: Schematic representation of a super cell with length R . In the super cell, the colored holes have the same meaning as shown in Fig. 2.2.

The procedure of calculating the coupling factor with a super cell is the following. First we create a super cell (Fig. 2.4) with the length equal to the heart to heart distance of two nearby cavities. Second we apply the Bloch condition $KR = 0$ ($KR = \pi$) to the boundary which means there is 0 (π) phase shift between the boundaries. Finally we only need to find out the resonant frequency $\omega_k(kR = 0)$ ($\omega_k(kR = \pi)$) of the modes in the super cell. The above procedure is implemented for the structure shown in Fig. 2.4 using the FDTD method.

2.3.4 Comparison of three methods

We show in Fig. 2.5 the coupling factors obtained from three the different methods versus spacing of the cavities. In Fig. 2.5, we see that the coupling factors obtained from the three different methods all decay exponentially as the distance between the cavities increases. This exponential feature can be attributed to the fact that the field envelope of the mode-gap cavities decays exponentially. We see the results from all three methods agree very well when $R = 8a$, $10a$. Here, a is the lattice constant of the photonic crystal. However there are noticeable deviations (less than 30 %) among the results from three different methods when $R = 6a$, $12a$. At $R = 6a$ the value from the Bloch method is bigger than from the other two methods. We attribute this to the frequency dependence of the coupling rate, detailed discussions are shown in Chapter 3. At $R = 12a$, the Bloch method and field integral method agree very well. However the value found by the direct numerical method is larger. The reason is not clear yet. In larger inter-cavity spacing the frequency difference between the symmetric mode and anti-symmetric mode is very small. The accuracy of finding very close resonant frequencies in simulation may be limiting the precision.

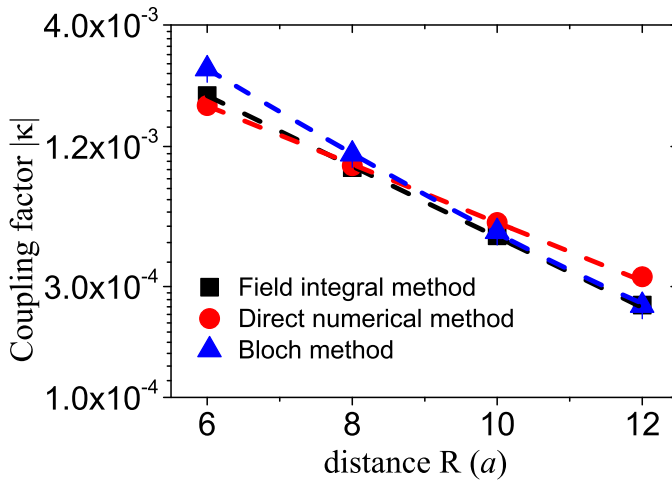


Figure 2.5: Coupling factor versus distance R . The red spots, black squares and blue triangles represent coupling factors calculated from direct numerical method, field integral method and Bloch method respectively. The red dashed, black dashed and blue dashed lines are the exponential fittings of the results obtained from direct numerical method, field integral method and Bloch method respectively.

From a technical point of view, for the calculation of the coupling factor, the direct numerical simulation is the most inefficient method, because the computation cell is quite big which means longer simulation time is needed. Also, multiple simulations are needed when values of various cavity spacing are needed. The Field integral is the most efficient method, because it only requires one simulation for obtaining the field of the mode. The efficiency of Bloch method is in between. However, its result may be the most directly applicable to retrieve the CROW band structure.

2.4 Optimization of the optical delay and transmission of the CROW band

In the first proposal of CROW [1], the CROW is an infinite structure. In reality, this is not achievable. For a realistic CROW structure, there are usually two situations which have to be considered. Firstly, the CROW is always finite size which means that the number of cavities is limited and finite-size effects [20] need to be taken into account. Secondly, for light transport we always need to couple light in and out of the CROW structure which means the CROW structure will have to be coupled to input and output waveguides (Fig. 2.6).

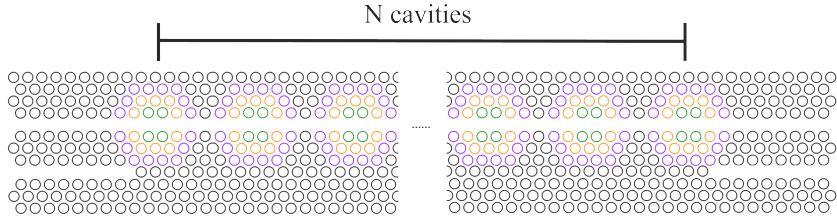


Figure 2.6: Schematic of a system consisted of N coupled cavities coupled to input and output waveguides.

A finite number of cavities means that the system supports a finite number of modes. When the spacing between the modes is larger than the linewidth of the modes, two effects will appear on the transmission of the system. Firstly, the transmission will show feature of sharp spikes or fringes. Secondly, the group delay of the system oscillates with the frequency. These characteristics are an obstacle to the applications of CROWs. For a slow light device the transmission band should be smooth and flat, and the group delay should be a smooth function. A solution which smooths the band without introducing extra intrinsic loss of the cavities is required.

Solutions to achieve a flat transmission and group delay spectrum require optimized tapering of the coupling rates between the cavities, and between the cavities and waveguides [20–24]. The optimization methods can be separated into three main types, transfer matrix based [20, 21], circuit based [23, 24], and Hamiltonian formalism based numerical optimization [22]. We choose a numerical optimization based on the coupled mode formalism. The first reason is that numerical optimization has more freedom on the number of optimized parameters compared to the other two types. The second reason is that coupled mode formalism has a simpler form compared to Hamiltonian formalism.

In this section, we first extend the coupled mode formalism so that it can be used to calculate the transmission of a system consisted of a finite CROW coupled to waveguides. Then we show the numerical optimization we use to optimize the transmission and group delay of the system.

2.4.1 Time dependent coupled mode model of direct coupled CROW and waveguide systems

For a single cavity coupled to a waveguide, the equation of motion of the system can be written as [13]

$$\frac{da_1(t)}{dt} = i\omega_0 a_1 - (\gamma_1 + \gamma_0) a_1 + \sqrt{2\gamma_1} S_+, \quad (2.16a)$$

$$S_- = -S_+ + \sqrt{2\gamma_1} a_1. \quad (2.16b)$$

In Eq. (2.16), $a_1(t)$ describes the time evolution of the amplitude in the cavity, and S_{\pm} is the amplitude of the forward (backward) propagating mode in the waveguide. It should be noticed that $|S_{\pm}|^2$ with SI unit W is the power input in

(reflected back to) the waveguide, whereas $|a(t)|^2$ with SI unit J is the energy in the cavity. Further, ω_0 is the intrinsic frequency of the cavity, γ_0 is the intrinsic loss rate of the cavity, and γ_1 is the coupling rate between the waveguide and cavity.

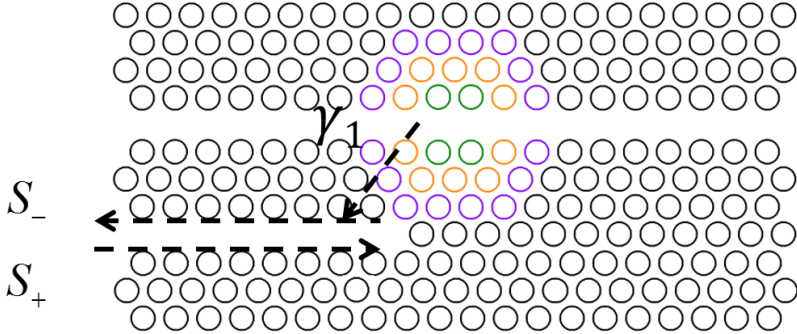


Figure 2.7: A single cavity coupled to a waveguide. We use S_{\pm} to denote the amplitude of the forward (backward) propagating mode in the waveguide, and γ_1 is the coupling rate between the waveguide and cavity.

We here briefly discuss the method we choose for calculating the coupling rate between cavity and waveguide. From Eq. (2.16), we note that the total loss rate γ_{total} of a cavity which is coupled to a waveguide is $\gamma_0 + \gamma_1$. For a high Q cavity, when it is coupled to a waveguide, we can assume $\gamma_{\text{total}} \approx \gamma_1$ since $\gamma_1 \gg \gamma_0$. Thus γ_1 can be obtained by calculating the loss rate of the structure consisting of a cavity and the corresponding waveguide to which it is coupled from FDTD simulation directly.

With the help of Eq. (2.16) and the coupled mode formalism discussed in Sec 2.2.2, we construct the complete model to describe the system,

$$\frac{da_1}{dt} = i\omega_0 a_1 - (\gamma_0 + \gamma_1)a_1 + \sqrt{2\gamma_1}S_{1+} + i\frac{\Gamma_{1,2}}{2}a_2, \quad (2.17a)$$

$$\frac{da_j}{dt} = i\omega_0 a_j - \gamma_0 a_j + i\frac{\Gamma_{j,j-1}}{2}a_{j-1} + i\frac{\Gamma_{j,j+1}}{2}a_{j+1} \quad (1 < j < N), \quad (2.17b)$$

$$\frac{da_N}{dt} = i\omega_0 a_N - (\gamma_0 + \gamma_2)a_N + \sqrt{2\gamma_2}S_{2-} + i\frac{\Gamma_{N-1,N}}{2}a_{N-1}, \quad (2.17c)$$

$$S_{1-} = -S_{1+} + \sqrt{2\gamma_1}a_1, \quad (2.17d)$$

$$S_{2-} = -S_{2+} + \sqrt{2\gamma_2}a_N. \quad (2.17e)$$

In Eq. (2.17), γ_2 is the coupling rate between the last cavity and the output waveguide. In $S_{j\pm}$, when $j = 1$ it represents the mode in the input waveguide, $j = 2$ refers to the output waveguide. Here, $\Gamma_{j,j-1}$ is the coupling rate between cavity j and cavity $j - 1$.

Eq. (2.17) in the Fourier domain can be written as a matrix,

$$\begin{pmatrix} M_b & i\frac{\Gamma_{1,2}}{2} & 0 & \cdots & 0 & 0 & 0 & 0 \\ i\frac{\Gamma_{1,2}}{2} & M_c & i\frac{\Gamma_{2,3}}{2} & \ddots & 0 & 0 & 0 & 0 \\ 0 & i\frac{\Gamma_{2,3}}{2} & \ddots & \ddots & 0 & 0 & 0 & 0 \\ \vdots & \ddots & \ddots & \ddots & \ddots & \vdots & \vdots & \vdots \\ 0 & 0 & \ddots & i\frac{\Gamma_{N-1,N-2}}{2} & M_c & i\frac{\Gamma_{N-1,N}}{2} & 0 & 0 \\ 0 & 0 & 0 & \cdots & i\frac{\Gamma_{N-1,N}}{2} & M_e & 0 & 0 \\ \sqrt{2\gamma_1} & 0 & 0 & \cdots & 0 & 0 & -1 & 0 \\ 0 & 0 & 0 & \cdots & 0 & \sqrt{2\gamma_2} & 0 & -1 \end{pmatrix} \times \begin{pmatrix} A_1 \\ A_2 \\ A_3 \\ \vdots \\ A_{N-1} \\ A_N \\ S_{1-} \\ S_{2+} \end{pmatrix} = \begin{pmatrix} -\sqrt{2\gamma_1}S_{1+} \\ 0 \\ 0 \\ \vdots \\ 0 \\ -\sqrt{2\gamma_2}S_{2-} \\ S_{1+} \\ S_{2-} \end{pmatrix} \quad (2.18)$$

In Eq. (2.18), $M_b = -i(\omega - \omega_0) - \gamma_1 - \gamma_0$, $M_e = -i(\omega - \omega_0) - \gamma_2 - \gamma_0$ and $M_c = -i(\omega - \omega_0) - \gamma_0$.

When light is injected only from the input waveguide we have $S_{1+} = 1$ and $S_{2-} = 0$. Thus, the response of the system ($\{A_1, \dots, A_N, S_{1-}, S_{2+}\}$) is the solution of the linear equations. $R = |S_{1-}|^2$ is the reflection of the system, $T = |S_{2+}|^2$ is the transmission of the system and $\tau = -\frac{d\text{Arg}(S_{2+})}{d\omega}$ is the group delay of the system.

2.4.2 Optimization of the optical delay and transmission

After introducing the time dependent coupled mode model, we now show an optimization procedure that yields a smooth and flat transmission spectrum of a finite CROW coupled to input and output waveguides. In the example we show here the number of the cavities N is 10.

We start with calculating the transmission spectrum and group delay for a structure without optimization. In the structure, the parameters are $\gamma_1 = \gamma_2 = 0.3 \Gamma_0$, $\Gamma_{j,j+1} = \Gamma_0 = 0.002 \omega_0$ ($1 \leq j < N$). The results are shown in Fig. 2.8 (black curves). In the transmission spectrum (black curve in Fig. 2.8(a)), we see 9 peaks corresponding to the 9 hybridized states of the cavities. In Fig. 2.8(b) (black curve), we see that the group delay oscillates with frequency as well. This is because the delays result from the discrete resonances. At the center frequency of each discrete state, the delay reaches a maximum.

The optimization to achieve a smooth transmission spectrum is done by a minimization procedure. Firstly, we define the total reflection function $R_{\text{total}} =$

$\int_{\omega_0 - \Gamma_0}^{\omega_0 + \Gamma_0} R(\omega) d\omega$. $R(\omega)$ is the reflection at input frequency ω . Γ_0 is half of the desired CROW bandwidth. Secondly, we let $\Gamma_{j,j+1} = \Gamma_0$ ($2 < j < N - 2$). In this case $\Gamma_0 = 0.002 \omega_0$. Thirdly, we make the coupling to the waveguide and the coupling between the first and last three cavities be free parameters. However, we constrain these couplings to remain symmetric, so that the total number of free parameters is three (γ_1 , $\Gamma_{1,2}$ and $\Gamma_{1,3}$). Finally, we run a minimization algorithm to find the set of free parameters which gives the minimum of R_{total} .

The optimized values are $\gamma_1 = \gamma_2 = 0.95 \Gamma_0$, $\Gamma_{1,2} = \Gamma_{N-1,N} = 1.5 \Gamma_0$, $\Gamma_{2,3} = \Gamma_{N-2,N-1} = 1.1 \Gamma_0$. The results with optimization are shown in Fig. 2.8 (red curves). After the optimization, we see the transmission spectrum is almost flat. At the same time, the delay spectrum is a smooth function without any oscillation. These results show that we have successfully optimized the optical delay and transmission of the CROW band.

The minimum transmission of the optimized band in our case is around 96%, which is good compared to the reported transfer matrix based method [20]. However, we use one extra optimization parameter. With three more optimized parameters a circuit based method reaches a transmission > 99% [23].

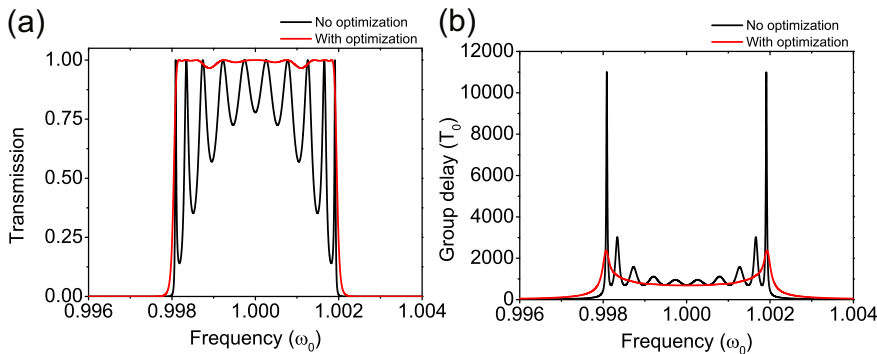


Figure 2.8: Transmission spectra (a) and group delay (b) of a system of 10 cavities coupled to input and waveguides without optimization (black curve) and with optimization (red curve).

2.5 Conclusion

In this chapter, we have performed a multi-scale modeling of CROW structures. The microscopic modeling is performed by FDTD while device scale modeling is done using coupled mode model. The coupling factor which is the connection between these two scales is calculated by three different methods. These three methods show a very good agreement. Finally, we have investigated the temporal coupled mode model for modeling the finite CROW structure with input and output waveguides. With the help of the temporal coupled mode model, we have shown an optimizing procedure that yields a CROW structure with flat transmission and smooth optical delay.

Bibliography

- [1] A. Yariv, Y. Xu, R. K. Lee, and A. Scherer, *Coupled-resonator optical waveguide: a proposal and analysis*, Opt. Lett. **24**, 711 (1999). — p.23, 25, 27, 30.
- [2] M. Notomi, E. Kuramochi, and T. Tanabe, *Large-scale arrays of ultrahigh-Q coupled nanocavities*, Nat. Photonics **2**, 741 (2008). — p.23.
- [3] F. Xia, L. Sekaric, and Y. Vlasov, *Ultracompact optical buffers on a silicon chip*, Nat. Photonics **1**, 65 (2007). — p.23.
- [4] F. Xia, L. Sekaric, M. O'Boyle, and Y. Vlasov, *Coupled resonator optical waveguides based on silicon-on-insulator photonic wires*, Appl. Phys. Lett. **89**, 041122 (2006). — p.23.
- [5] E. Kuramochi, K. Nozaki, A. Shinya, K. Takeda, T. Sato, S. Matsuo, H. Taniyama, H. Sumikura, and M. Notomi, *Large-scale integration of wavelength-addressable all-optical memories on a photonic crystal chip*, Nat. Photonics **8**, 474 (2014). — p.23.
- [6] N. Ashcroft and N. Mermin, *Solid State Physics* (Saunders College, Philadelphia, 1976). — p.23, 28.
- [7] M. J. Hartmann, F. G. S. L. Brandão, and M. B. Plenio, *Quantum many-body phenomena in coupled cavity arrays*, Laser Photon. Rev. **2**, 527 (2008). — p.23.
- [8] A. Altland and B. D. Simons, *Condensed Matter Field Theory* (Cambridge University Press, Cambridge, 2010). — p.23.
- [9] R. O. Umucalilar and I. Carusotto, *Artificial gauge field for photons in coupled cavity arrays*, Phys. Rev. A **84**, 043804 (2011). — p.23.
- [10] M. Hafezi, S. Mittal, J. Fan, A. Migdall, and J. M. Taylor, *Imaging topological edge states in silicon photonics*, Nat. Photonics **7**, 1001 (2013). — p.23.
- [11] K. Fang, Z. Yu, and S. Fan, *Realizing effective magnetic field for photons by controlling the phase of dynamic modulation*, Nat. Photonics **6**, (2012). — p.23.
- [12] H. A. Haus and W. Huang, *Coupled-mode theory*, Proc. IEEE **79**, 1505 (1991). — p.23, 24, 25, 27.
- [13] J. D. Joannopoulos, S. G. Johnson, J. N. Winn, and R. D. Meade , *Photonic Crystals: Molding the Flow of Light* (Princeton University Press, Princeton, 2008). — p.23, 31.
- [14] C. Manolatou, M. Khan, S. Fan, P. Villeneuve, H. Haus, and J. Joannopoulos, *Coupling of modes analysis of resonant channel add-drop filters*, IEEE J. Quant. Electron. **35**, 1322 (1999). — p.23.
- [15] E. N. Economou, *Green's functions in quantum physics* (Springer, Heidelberg, 2011). — p.23.

- berg, 2006). — p.24.
- [16] J. J. Sakurai, *Modern Quantum Mechanics* (Addison-Wesley, 1994). — p.24.
 - [17] E. Kuramochi, M. Notomi, S. Mitsugi, A. Shinya, T. Tanabe, and T. Watanabe, *Ultrahigh- Q photonic crystal nanocavities realized by the local width modulation of a line defect*, Appl. Phys. Lett. **88**, 041112 (2006). — p.27.
 - [18] A. F. Oskooi, D. Roundy, M. Ibanescu, P. Bermel, J. Joannopoulos, and S. G. Johnson, *Meep: A flexible free-software package for electromagnetic simulations by the FDTD method*, Comput. Phys. Commun. **181**, 687 (2010). — p.27, 28.
 - [19] A. Taflove and S. C. Hagness, *Computational Electrodynamics: The Finite-Difference Time-Domain Method, Third Edition* (Artech House, Boston, 2005). — p.27.
 - [20] P. Chak and J. E. Sipe, *Minimizing finite-size effects in artificial resonance tunneling structures*, Opt. Lett. **31**, 2568 (2006). — p.30, 31, 34.
 - [21] J. K. S. Poon, J. Scheuer, Y. Xu, and A. Yariv, *Designing coupled-resonator optical waveguide delay lines*, J. Opt.Soc. Am. B **21**, 1665 (2004). — p.31.
 - [22] M. Sumetsky and B. Eggleton, *Modeling and optimization of complex photonic resonant cavity circuits*, Opt. Express **11**, 381 (2003). — p.31.
 - [23] H.-C. Liu and A. Yariv, *Synthesis of high-order bandpass filters based on coupled-resonator optical waveguides (CROWs)*, Opt. Express **19**, 17653 (2011). — p.31, 34.
 - [24] V. Van, *Circuit-based method for synthesizing serially coupled microring filters*, J. Lightwave Technol. **24**, 2912 (2006). — p.31.

CHAPTER 3

Dispersion of coupled mode-gap cavities

The dispersion of a coupled resonator optical waveguide (CROW) made of photonic crystal mode-gap cavities is pronouncedly asymmetric. This asymmetry cannot be explained by the standard tight binding model. We show that the fundamental cause of the asymmetric dispersion is the inherent dispersive cavity mode profile, i.e., the mode wave function depends on the driving frequency, not the eigenfrequency. This occurs because the photonic crystal cavity resonances do not form a complete set. We formulate a dispersive mode coupling model that accurately describes the asymmetric dispersion without introducing any new free parameters.

3.1 Introduction

In coupled cavity systems in photonic crystals (PhC), light transport occurs via evanescent field coupling between high-quality factor (Q) cavities. The well known example is the coupled resonator optical waveguide (CROW) which is a linear chain of cavities [1]. Arrays of coupled cavities have attracted substantial scientific attention for practical applications such as slow light engineering and strong light-matter interaction enhancement [2–4], and many novel phenomena of fundamental interest such as gauge fields [5, 6] and time-reversal of light pulses [7, 8].

Realizations of low loss and compact CROWs require high- Q , wavelength-sized cavities. Mode-gap cavities [9] created by shifting some of the holes of around PhC waveguides as shown in Fig. 3.1(a) have been demonstrated to be extremely suitable for creating large scale cavity arrays [10, 11].

The tight binding (TB) model [1, 12] is the usual approach for modeling the dispersion in coupled cavities [3, 4, 13, 14]. The core concept of the TB model is that in coupled cavities the wave functions are tightly confined in each cavity. The eigenmodes of the individual cavities are then coupled to yield waveguide modes. Coupling between neighboring cavities is due to the overlap of the eigen wave function of the cavity modes. The dispersion of the CROW band as predicted by the TB model is a cosine curve [1]. For a given structure, its parameters can be

This chapter has been published as: J. Lian, S. Sokolov, E. Yüce, S. Combrié, A. De Rossi, A. P. Mosk, Opt. Lett. **40**, 4488 (2015).

evaluated by numerical methods, such as plane wave expansion (PWE) [15] and finite difference time domain (FDTD) [16].

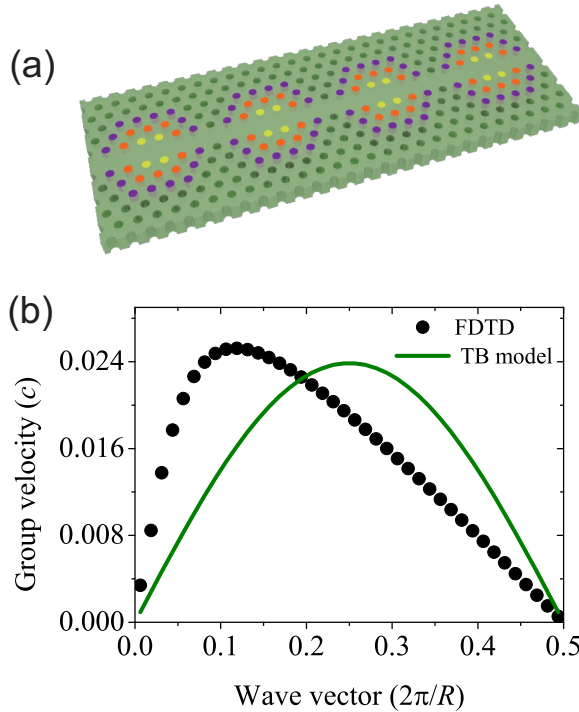


Figure 3.1: (a) Schematic of a CROW composed of coupled mode-gap cavities. The cavities are created by shifting of the yellow, red and purple holes around the waveguide in a tapered way. The width of the waveguide is $0.98\sqrt{3}a$ (a is the lattice constant). The radius of the holes is $0.25 a$. The shift of the yellow holes is $S1=\eta 0.0124\sqrt{3}a$, η is a factor we call it modulation strength. The shifts of the red and purple holes are $2/3 S1$ and $1/3 S1$ respectively.(b) Group velocity of the 2D CROW consisting of mode gap cavities with modulation strength 1.5 calculated by 2D FDTD (black dots) and TB model (green line). Parameters are calculated by FDTD.

However, the TB model does not describe the dispersion of a CROW composed of mode-gap cavities correctly. In Fig. 3.1(b) we show the group velocity curve as obtained from the TB model and as calculated by FDTD [17]. The TB result is perfectly symmetric with respect to $k = 0.5\pi/R$. In contrast, the FDTD result is pronouncedly asymmetric. The asymmetric spectrum has also been observed experimentally [11]. It is remarkable that the TB model fails here, as it only depends on the assumption of energy-independent eigenmodes, which is a direct consequence of the completeness of the set of eigenmodes [18].

In this Letter, we uncover the physical origin of the discrepancy and propose an improved mode coupling model.

3.2 The physical cause of the asymmetric dispersion

The resonant modes of a closed conservative cavity form a complete set. An important consequence of completeness is the fact that the response of a cavity is defined in terms of modes do not themselves depend on the driving frequency. In an open cavity we have quasimodes which form a complete set only if certain conditions are fulfilled [19], essentially, the edge of the resonant mode must be clearly defined in the structure and no outgoing waves should be scattered back to the cavity. These conditions are never fulfilled in a PhC cavity. In a PhC cavity light is confined by constructive interference of Bragg reflection and the Bragg reflection takes place throughout the PhC structure. As a result, the quasimodes do not form a complete set and their spatial profile depends on the driving frequency, i.e., mode profile is dispersive.

The breakdown of completeness for an open cavity shows a signature in driven oscillation. If the cavity is driven at frequency ω , the field inside the cavity will be $\mathbf{E}(\mathbf{r}, t) = \mathbf{E}(\mathbf{r}, \omega)e^{-i\omega t}$ where $\mathbf{E}(\mathbf{r}, \omega) \neq \mathbf{E}(\mathbf{r}, \omega_0)$. Alternatively speaking, when an open cavity is driven, the wave function of the mode is determined by the driving frequency not the free oscillation frequency.

In CROWs, therefore, the coupling between neighboring cavities is not characterized by the overlap of the eigen modes of the single cavity $\mathbf{E}(\mathbf{r}, \omega_0)$ (ω_0 is the eigen frequency of the cavity) but of the dispersive modes $\mathbf{E}(\mathbf{r}, \omega)$.

In Fig. 3.2 the dispersion of a quasimode is shown qualitatively. In a true eigen mode, the size of the mode profile should be always the same as the cavity is driven at different frequencies. However, the quasimode is dispersive and will be spatial narrower (Fig. 3.2(a)) or wider (Fig. 3.2(b)) than the resonant mode when the driving frequency is lower or higher than the intrinsic frequency respectively.

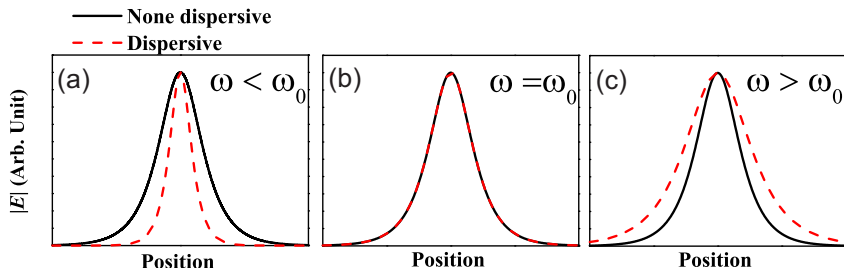


Figure 3.2: In driven oscillation, the quasimode (red) will be smaller (a) or larger (c) compared to the intrinsic resonant mode in the case when driving frequency is lower or higher than the intrinsic frequency. In contrast a true eigenmode (black) keeps the same spatial profile (b) when driven off-resonance.

We performed two dimensional (2D) FDTD simulations to quantitatively study the dispersion of the mode profile of PhC mode-gap cavities. In the simulation a continuous source is placed in the center of a single cavity and switched on smoothly. After the transient died out, we output the E_y field across the

waveguide direction. The same procedure was repeated several times at different frequencies and different cavities [20].

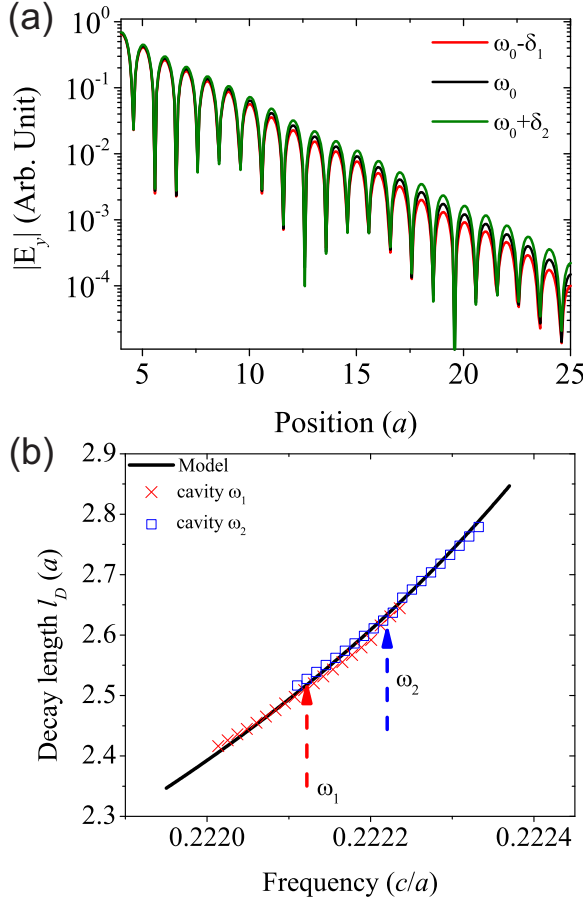


Figure 3.3: (a) 2D FDTD simulation of forced driving oscillation of a mode-gap cavity. The amplitude of the E_y field across the waveguide direction versus the position is plotted. The center position is located at 0. The red, black and green lines illustrate cases with different driving frequencies ($\omega_0=0.22212$ c/a , $\delta_1=0.00011$ c/a and $\delta_2=0.00010$ c/a). (b) Red crosses (blue squares) depict decay lengths of a cavity with intrinsic frequency $\omega_1=0.22212$ c/a ($\omega_2=0.22222$ c/a). The black curve is the model we use to describe the decay length. The decay lengths are obtained by fitting the envelope of the field from $x = 4a$ to $x = 14a$. The only difference between the geometries of the two cavities is the modulation strength.

In Fig. 3.3(a) we plot the amplitudes of the E_y field versus the position across the waveguide direction when we drive the cavity at three different frequencies. When the driving frequency is $\omega_0 + \delta_1$ which is higher than the resonant frequency ω_0 , the decay in space is slower. Alternatively speaking, the mode is larger in

space. When the driving frequency is $\omega_0 - \delta_2$, the mode is smaller. This clearly shows that for a single mode-gap cavity, the mode profile differs depending on the driving frequency. Outside the modulation part of the cavity, the envelope of the mode profile decays exponentially. Along the waveguide direction x , the envelope decays as e^{-x/l_D} , where l_D is the decay length and $x = 0$ is the center of the cavity. The decay length is related to the dispersion of the waveguide where the cavity lies in. The waveguide dispersion above the bandedge can be expanded as $\omega = \omega_{\text{edge}} + (k - \pi/a)^2/(2m)$ [21], where $m = (\partial^2\omega/\partial^2k)^{-1}$ is the photon mass in analogy to the effective mass of electrons [12] and ω_{edge} is the frequency of the edge of the waveguide band. By analytic continuation of the dispersion, the wave vector k becomes a complex number when $\omega < \omega_{\text{edge}}$. The decay length which is the inverse of the imaginary part of the wave vector, follows as $l_D = (2m(\omega_{\text{edge}} - \omega))^{-1/2}$. In Fig. 3.3(b), we plot the calculated decay lengths by the analytical model and the extracted decay lengths from FDTD simulations of two different cavities at various driving frequencies. Firstly we see when the cavity is driven at different frequencies the decay lengths differ. Secondly for two different cavities (one with intrinsic frequency ω_1 and the other with intrinsic frequency ω_2), when the driving frequencies are the same, the decay lengths are the same. The decay lengths are well described by the analytical model, and we conclude that mode-gap cavities have a mode profile that depends on the driving frequency not the resonant frequency.

3.3 Dispersive Mode (DM) model

As the consequence of the dispersive mode profile, the mode functions in the expression of the coupling rate [1, 22] should be the dispersive mode (DM) not the eigen mode. The expression of the coupling rate becomes

$$\Gamma(\omega) = \frac{\omega \int \delta\epsilon(\mathbf{r} - \mathbf{R}) \mathbf{E}_\omega(\mathbf{r} - \mathbf{R}) \cdot \mathbf{E}_\omega(\mathbf{r}) d\mathbf{r}}{\int \epsilon(\mathbf{r}) \mathbf{E}_\omega(\mathbf{r}) \cdot \mathbf{E}_\omega(\mathbf{r}) d\mathbf{r}}. \quad (3.1)$$

In Eq.(3.1), $\mathbf{E}_\omega(\mathbf{r})$ is the electric field of the wave function at frequency ω , $\epsilon(\mathbf{r})$ is the dielectric constant of a single cavity and $\delta\epsilon(\mathbf{r} - \mathbf{R})$ is the dielectric difference between one isolated cavity and two cavities with heart to heart distance \mathbf{R} . This expression is identical to that derived by Haus *et al.*[22] and by Yariv *et al.* [1], except for the replacement of the resonant mode profile $\mathbf{E}_{\omega_0}(\mathbf{r})$ by the dispersive mode profile $\mathbf{E}_\omega(\mathbf{r})$. The resulting dispersion of the CROW is,

$$\omega = \omega_0 + \Delta + \Gamma(\omega) \cos(kR), \quad (3.2)$$

where ω_0 is the eigen frequency of the single resonators, Δ is the frequency difference between ω_0 and the center of the CROW band.

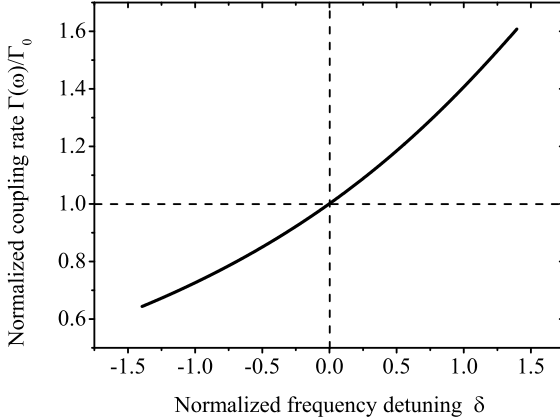


Figure 3.4: Normalized coupling rate $\Gamma(\omega)/\Gamma_0$ of the CROW structure in Fig. 3.1 versus the normalized frequency detuning δ .

To evaluate Eq.(3.1) and (3.2), some assumptions are made. Firstly, we assume that each polarization of $\mathbf{E}_\omega(\mathbf{r})$ can be decomposed into $E_\omega^X(x)E_\omega^{YZ}(y,z)$, here x, y represent the spatial coordinates and x is along the waveguide direction, where the $E_\omega^{YZ}(yz)$ can be approximated to be non dispersive, $E_\omega^{YZ}(y,z) \approx E_{\omega_0}^{YZ}(y,z)$. Secondly, we approximate the envelope of $E_\omega^X(x)$ by $1/\cosh(x/l_D)$, which is a resonable approximation for mode-gap cavities. The last assumption is for $\delta\epsilon(\mathbf{r} - \mathbf{R})$ and $\epsilon(\mathbf{r})$. We divide $\delta\epsilon(\mathbf{r} - \mathbf{R})$ into 5 blocks. For each block, the effects of $\delta\epsilon$ is essentially the increase of the effective dielectric function of the waveguide. We approximate that this increase happens at the center of each block, so we express $\delta\epsilon$ as a collection of delta functions $\delta\epsilon = \sum_{j=-2}^2 \delta(x - x_j)\bar{\delta}\epsilon_j$ with $x_j = ja$ and $\bar{\delta}\epsilon_j = \frac{3-|j|}{3}\bar{\delta}\epsilon_0$ (where $\bar{\delta}\epsilon_0$ is a constant). Based on these three assumptions the coupling rate is

$$\Gamma(\omega) = \beta \sum_{j=-2}^2 \frac{(3-|j|)\omega}{l_D \cosh(\frac{R-ja}{l_D}) \cosh(\frac{ja}{l_D})}. \quad (3.3)$$

Here β is a proportionality constant resulting from the integral over y , and we may abbreviate $\Gamma(\omega) = \beta g(\omega)$ where we emphasize $g(\omega)$ can be evaluated analytically. The dispersion relation becomes

$$\omega = \omega_0 + \Delta + \beta g(\omega) \cos(kR), \quad (3.4)$$

there are only three unknowns (ω, Δ, β) which is exactly the same number of the unknowns the TB model has, i.e., our model does not introduce any extra free parameters.

We show the normalized coupling rate of the CROW structure in Fig. 3.1 as a function of normalized frequency detuning $\delta = (\omega - \omega_0)/\Gamma_0$ with $\Gamma_0 = \Gamma(\omega_0)$ in Fig. 3.4. The normalized coupling rate is defined as $\Gamma(\omega)/\Gamma_0$, it is also equivalent

to $g(\omega)/g(\omega_0)$. The normalized coupling rate in Fig. 3.4 increases non-linearly as the detuning increases, in other words, $\Gamma(\omega)$ is highly dispersive. At the low k values which correspond to positive detuning δ , the coupling rate is larger, and therefore the group velocity is enhanced. As a result, the maximum of the group velocity shifts to low k values as compared to the result from the TB model.

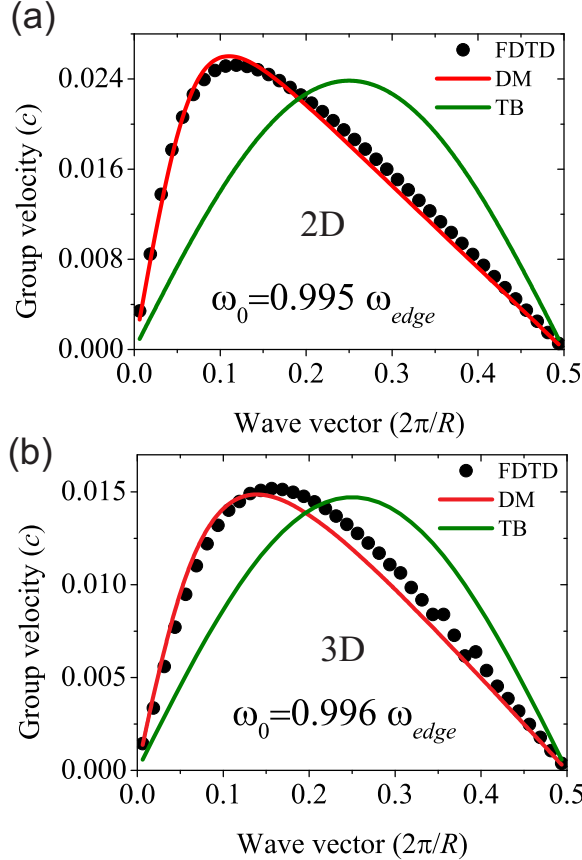


Figure 3.5: (a) Group velocity of the 2D CROW consisting of mode gap cavities with modulation strength 1.5 calculated by FDTD (black dots), TB model (green line) and DM model (red line). All the parameters are as same as in simulations of driven oscillation. (b) Group velocity of the 3D CROW consisting of mode gap cavities with modulation strength 2 calculated by FDTD (black dots), TB model (green line) and DM model (red line). In the 3D simulation, $h = 0.37a$ (h is the thickness of the slab) and $\epsilon = 10.04$.

We present the calculated group velocity of the CROW in 2D and in a 3D membrane structure in Fig. 3.5. In Fig. 3.5(a) the results of group velocity calculated by DM model is asymmetric with a maximum at $k \approx 0.10$ ($2\pi/R$), this matches the 2D FDTD results extremely well. In Fig. 3.5(b) the group velocity from the DM model is asymmetric with maximum at $k \approx 0.13$ ($2\pi/R$),

it agrees satisfactorily with the fully 3D FDTD results [23]. In contrast, the result from the TB model is symmetric about $k = 0.5$ (π/R). The excellent match between our DM model and the FDTD data confirms that dispersion of the cavity quasimodes is indeed the physical reason for the failure of the TB model to accurately describe photonic crystal CROWs.

3.4 Conclusion

In conclusion, the dispersion of a CROW composed of photonic crystal cavities can not be described by the standard TB model due to the breakdown of completeness of the resonant modes. We show a new model taking into account the dispersive property of the mode profile of the single cavity in a CROW structure. Our model describes the dispersion of the PhC CROW accurately without additional free parameters. Dispersion of the modes is inherent in all cavities. For racetrack resonators [2, 24] and PhC cavities with resonances far away from the bandedge such as L3 cavities [25], dispersion is negligible and shows no discernible effect on the dispersion of the related CROW structures. However, for shallow defect cavities, such as mode-gap cavities with small modulation strength and double-heterostructure cavities [26, 27] with small lattice mismatch, the defect modes are close to the edge of the waveguide band which make the dispersive nature of the modes become pronounced. The dispersion of CROWS of such cavities has strong asymmetry. Thus, our theory will be useful for describing all devices based on coupling of shallow defect cavities such as delay lines [10], optical memory [28], and \mathcal{PT} symmetric diodes [29].

Bibliography

- [1] A. Yariv, Y. Xu, R. K. Lee, and A. Scherer, *Coupled-resonator optical waveguide: a proposal and analysis*, Opt. Lett. **24**, 711 (1999). — p.37, 41.
- [2] F. Xia, L. Sekaric, and Y. Vlasov, *Ultracompact optical buffers on a silicon chip*, Nat. Photonics **1**, 65 (2007). — p.37, 44.
- [3] M. J. Hartmann, F. G. S. L. Brandão, and M. B. Plenio, *Quantum many-body phenomena in coupled cavity arrays*, Laser Photon. Rev. **2**, 527 (2008). — p.37.
- [4] M. F. Yanik and S. Fan, *Stopping light all optically*, Phys. Rev. Lett. **92**, 083901 (2004). — p.37.
- [5] M. Hafezi, S. Mittal, J. Fan, A. Migdall, and J. M. Taylor, *Imaging topological edge states in silicon photonics*, Nat. Photonics **7**, 1001 (2013). — p.37.
- [6] R. O. Umucalllar and I. Carusotto, *Artificial gauge field for photons in coupled cavity arrays*, Phys. Rev. A **84**, 043804 (2011). — p.37.
- [7] S. Longhi, *Stopping and time reversal of light in dynamic photonic structures via Bloch oscillations*, Phys. Rev. E **75**, 026606 (2007). — p.37.
- [8] M. F. Yanik and S. Fan, *Time reversal of light with linear optics and modulators*, Phys. Rev. Lett. **93**, 173903 (2004). — p.37.
- [9] E. Kuramochi, M. Notomi, S. Mitsugi, A. Shinya, T. Tanabe, and T. Watanabe, *Ultrahigh- Q photonic crystal nanocavities realized by the local width modulation of a line defect*, Appl. Phys. Lett. **88**, 041112 (2006). — p.37.
- [10] M. Notomi, E. Kuramochi, and T. Tanabe, *Large-scale arrays of ultrahigh- Q coupled nanocavities*, Nat. Photonics **2**, 741 (2008). — p.37, 44.
- [11] N. Matsuda, E. Kuramochi, H. Takesue, and M. Notomi, *Dispersion and light transport characteristics of large-scale photonic-crystal coupled nanocavity arrays*, Opt. Lett. **39**, 2290 (2014). — p.37, 38.
- [12] N. Ashcroft and N. Mermin, *Solid State Physics* (Saunders College, Philadelphia, 1976). — p.37, 41.
- [13] P. Chak and J. E. Sipe, *Minimizing finite-size effects in artificial resonance tunneling structures*, Opt. Lett. **31**, 2568 (2006). — p.37.
- [14] M. Sumetsky and B. Eggleton, *Modeling and optimization of complex photonic resonant cavity circuits*, Opt. Express **11**, 381 (2003). — p.37.
- [15] K. M. Leung and Y. F. Liu, *Photon band structures: The plane-wave method*, Phys. Rev. B **41**, 10188 (1990). — p.38.
- [16] A. Tafove and S. C. Hagness, *Computational Electrodynamics: The Finite-Difference Time-Domain Method, Third Edition* (Artech House, Boston, 2005). — p.38.
- [17] A. F. Oskooi, D. Roundy, M. Ibanescu, P. Bermel, J. Joannopoulos, and S.

- G. Johnson, *Meep: A flexible free-software package for electromagnetic simulations by the FDTD method*, Comput. Phys. Commun. **181**, 687 (2010). — p.38.
- [18] J. J. Sakurai, *Modern Quantum Mechanics* (Addison-Wesley, 1994). — p.38.
- [19] E. Ching, P. Leung, A. Maassen van den Brink, W. Suen, S. Tong, and K. Young, *Quasinormal-mode expansion for waves in open systems*, Rev. Mod. Phys. **70**, 1545 (1998). — p.39.
- [20] To decrease the time of the transient, the dielectric is made slightly lossy given by $\epsilon(\omega) = \epsilon(\infty) + \frac{\sigma\omega_a^2}{\omega_a^2 - \omega^2 - i\omega\gamma_a}$, where $\omega_a = 5(2\pi c/a)$, $\gamma_a = 30(2\pi c/a)$ and $\sigma = 0.5$. The strength of this artificial loss has not influenced our results. — p.40.
- [21] R. Faggiani, R. Baron, X. Zang, L. Lalouat, S. A. Schulz, K. Vynck, B. Regan, B. Cluzel, F. De Fornel, T. F. Krauss, and P. Lalanne, *Lower bound for the spatial extent of localized modes in photonic-crystal waveguides with small random imperfections*, Sci Rep. **6**, 27037 (2016). — p.41.
- [22] H. A. Haus and W. Huang, *Coupled-mode theory*, Proc. IEEE **79**, 1505 (1991). — p.41.
- [23] The shape of the group velocity is independent of the resolution the FDTD simulations. The absolute accuracy of the group velocity is estimated as 4%. — p.44.
- [24] F. Xia, L. Sekaric, M. O’Boyle, and Y. Vlasov, *Coupled resonator optical waveguides based on silicon-on-insulator photonic wires*, Appl. Phys. Lett. **89**, 041122 (2006). — p.44.
- [25] Y. Akahane, T. Asano, and B.-S. Song, *High- Q photonic nanocavity in a two-dimensional photonic crystal*, Nature **425**, 944 (2003). — p.44.
- [26] B.-S. Song, S. Noda, T. Asano, and Y. Akahane, *Ultra-high-Q photonic double-heterostructure nanocavity*, Nat. Mater. **4**, 207 (2005). — p.44.
- [27] J. Jágerská, N. Le Thomas, V. Zabelin, R. Houdré, W. Bogaerts, P. Dumon, and R. Baets, *Experimental observation of slow mode dispersion in photonic crystal coupled-cavity waveguides*, Opt. Lett. **34**, 359 (2009). — p.44.
- [28] E. Kuramochi, K. Nozaki, A. Shinya, K. Takeda, T. Sato, S. Matsuo, H. Taniyama, H. Sumikura, and M. Notomi, *Large-scale integration of wavelength-addressable all-optical memories on a photonic crystal chip*, Nat. Photonics **8**, 474 (2014). — p.44.
- [29] H. Ramezani, H.-K. Li, Y. Wang, and X. Zhang, *Unidirectional Spectral Singularities*, Phys. Rev. Lett. **113**, 263905 (2014). — p.44.

CHAPTER 4

Measurement of the profiles of disorder-induced localized resonances by local tuning

Near the band edge of photonic crystal waveguides, localized modes appear due to disorder. We demonstrate a new method to elucidate the spatial profile of the localized modes in such systems using precise local tuning. Using deconvolution with the known thermal profile, the spatial profile of a localized mode with quality factor (Q) $> 10^5$ was successfully reconstructed with a resolution of $2.5 \mu\text{m}$.

4.1 Introduction

Disorder-induced multiple scattering of waves is a universal phenomenon in physics. Coherent scattering in a disordered system leads to localization of waves [1, 2]. For a periodical system with disorder, localization of waves appears near the edge of the energy band [3, 4]. In photonics, photonic crystal waveguides (PhCWG) [5] are well-known periodic systems where localization of light [6–8] is unavoidable near the band edge because of the ubiquitous disorder caused by fabrication [9]. Localization of light in PhCWGs appears as a set of spatially random localized modes.

An example of a disorder-induced random localized mode is shown in Fig. 4.1. The numerically calculated intensity profile shows an envelope that is approximately $30 \mu\text{m}$ wide, and oscillates with a carrier frequency that corresponds to the waveguide mode at the edge of the Brillouin zone. Remarkably, the disorder on the 1-nm scale shows no noticeable effect on the local structure of the mode wavefunction, its main effect is the modification of the envelope which is around $10 \mu\text{m}$ in scale. This shows the the most important information of the random localized mode is the spatial profile, the envelope of the mode.

The random localized modes raise much interest because of their inherently high quality factor (Q), which maybe utilized for random quantum networks [10]. The spatial and the spectral characteristics of disorder induced modes in PhCWGs are not predictable due to the disordered nature. In previous work, characterizations have been done using invasive methods that perturb the structure, such as near field scanning microscope (NSOM) [7, 8] and enhanced emission measurements from the quantum dots in the PhCWGs [10]. Time dependent optical tuning by carrier injection induces local index shift and absorption [11],

hence it is not applicable for high Q systems.

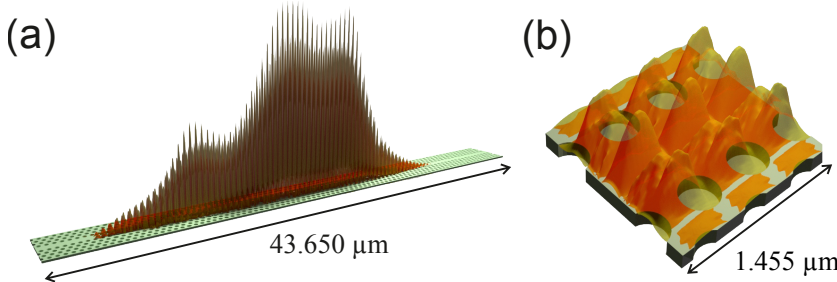


Figure 4.1: (a) Visualization of the intensity of a typical disorder induced localized mode in a photonic crystal waveguide. (b) A zoom in of the center of (a), the intensity is scaled down in order to show that the periodic oscillation of the intensity matches the period of the waveguide.

Here, we show a new non-invasive method to elucidate the spatial profile of the localized modes in a photonic crystal waveguide with unavoidable disorder. In this method, we first use precise local thermal tuning [12] to obtain the resonance wavelength shift as a function of position. Secondly, using deconvolution with the known thermal profile, we reconstruct the mode profiles of the disorder-induced modes. Using our method, we successfully reconstruct the spatial profile a localized mode with $Q > 10^5$ with a resolution of 2.5 μm.

4.2 Sample and Apparatus

The sample and experimental setup is shown in Fig. 4.2. The sample is a triangle lattice photonic crystal membrane structure made of GaInP [13]. The thickness h of the membrane is 180 nm and the lattice constant a is 485 nm. A barrier waveguide with width $W_0 = 0.98\sqrt{3}a$ and length $L = 106a$ is created in the sample and it is side coupled to two carrier waveguides with width $W_1 = 1.1\sqrt{3}a$. A tunable continuous wave (CW) infrared (IR) laser is coupled to the input carrier waveguide of our sample by a polarization maintaining lensed fiber (PMF) with numerical aperture (NA) of 0.55. The transmitted signal from the sample is collected by another lensed fiber, then detected by a photodiode (PD). A pump spot from a CW diode laser ($\lambda_{\text{pump}} = 405$ nm) is focused on our sample surface by an objective with 0.4 NA. The full width half maximum (FWHM) of the pump spot is 0.83 μm, and the power is 20 μW. The surface of the sample is imaged with a visible range camera using a tube lens with a system magnification of $\times 27$. We control the position of the pump spot on the barrier waveguide by writing blazed phase gratings with different periods on a spatial light modulator. To suppress oxidation effects [14, 15], the sample is kept in a N₂ environment with oxygen concentration less than 0.03% for all measurements.

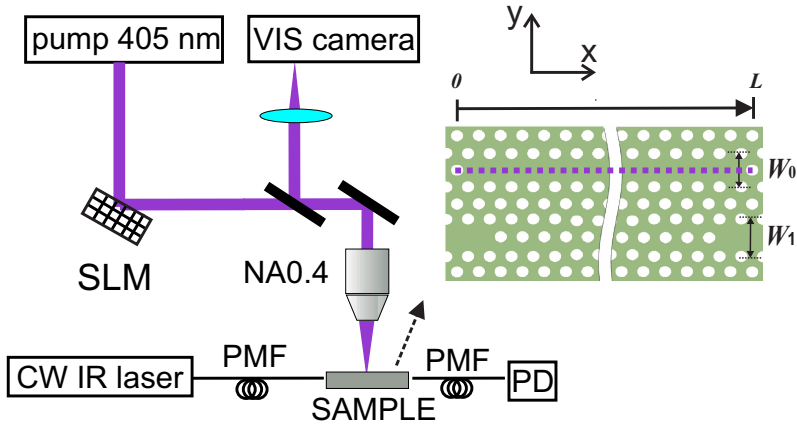


Figure 4.2: Experimental setup and schematic representation of the sample. PD is the photodiode which is used to detect the transmission signal. PMFs are the polarization maintaining lenses which are used to couple light from the CW IR laser to the sample and couple light out of sample to the PD.

4.3 Transmission spectra

In Fig. 4.3(a), we show a reference transmission spectrum of our sample. We see multiple narrow peaks and dips on top of Fabry-Pérot fringes with Fano line shapes [16]. The narrow resonances correspond to the disorder induced localized modes in the PhCWG. The transmission spectrum does not provide spatial information of these modes. In Fig. 4.3(b), we show the transmission spectrum with and without a pump spot at position $x = 17.7 \mu\text{m}$ in the waveguide. We observe a pump induced redshift of 163 pm for this resonance. The reference wavelength of this resonance is 1531.515 nm and the observed Q factor for the reference is 3.8×10^5 . Due to the pump laser noise, we see modulation on the intensity of the transmitted signal, however no significant influence on the linewidth is observed.

The redshift of the resonance is due to the increase of the dielectric constant of the sample with temperature. This redshift can also be calculated quantitatively by perturbation theory,

$$\Delta\lambda(\mathbf{r}_0) = \lambda_0 \frac{\int \delta\epsilon(\mathbf{r}_0 - \mathbf{r}) |\mathbf{E}(\mathbf{r})|^2 d\mathbf{r}}{\int \epsilon(\mathbf{r}) |\mathbf{E}(\mathbf{r})|^2 d\mathbf{r}}. \quad (4.1)$$

Here λ_0 is the wavelength of the resonance shown in Fig. 4.3(a). $\mathbf{E}(\mathbf{r})$ represents the electric field of the mode. $\epsilon(\mathbf{r})$ is the dielectric distribution of the waveguide. $\delta\epsilon(\mathbf{r}_0 - \mathbf{r})$ is the perturbation of the dielectric caused by the thermal tuning, it is proportional to the temperature distribution $\delta T(\mathbf{r}_0 - \mathbf{r})$ and \mathbf{r}_0 is the pump position. Perturbation theory is only valid when shifts are small compared to the spacing to any nearby mode.

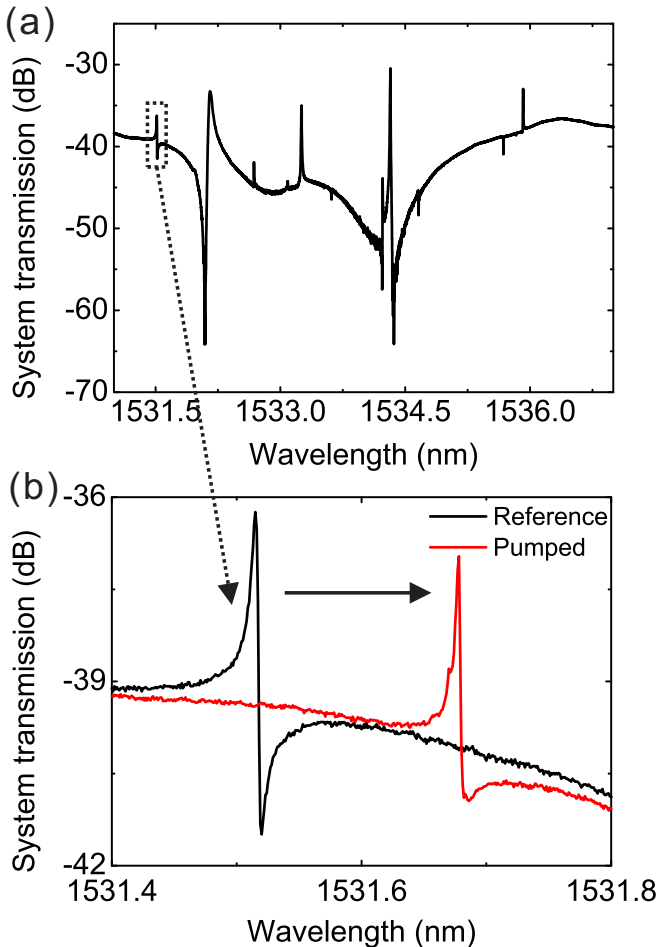


Figure 4.3: (a) Transmission spectrum of the sample. (b)Zoomed in reference (black) and pumped (red) transmission spectra of the sample. The system transmission here is defined as the ratio between the power we send into the input fiber and the power we detect on the PD.

4.4 Thermal profile and extracted intensity profile

When we move the pump along the waveguide direction, the wavelength shift we detect is the convolution of the intensity profile of the resonance and the temperature profile that is induced by the pump beam. Taking into account the fact the system is 1D, the obtained wavelength shift can be approximated as

$$\Delta\lambda(x_0) \approx \alpha \int (T(x_0 - x) - T_0) |\mathbf{E}^X(x)|^2 dx. \quad (4.2)$$

Here, $T(x)$ is the temperature profile along the waveguide direction and temperature gradients transversal to the waveguide are neglected. $|\mathbf{E}^X(x)|^2$ is the envelope of the mode profile along the waveguide which is expected to be the same as the integrated intensity along y direction, α is a normalization factor. As a result, the spatial profile of the localized mode can be reconstructed by deconvolving the wavelength shift with temperature distribution.

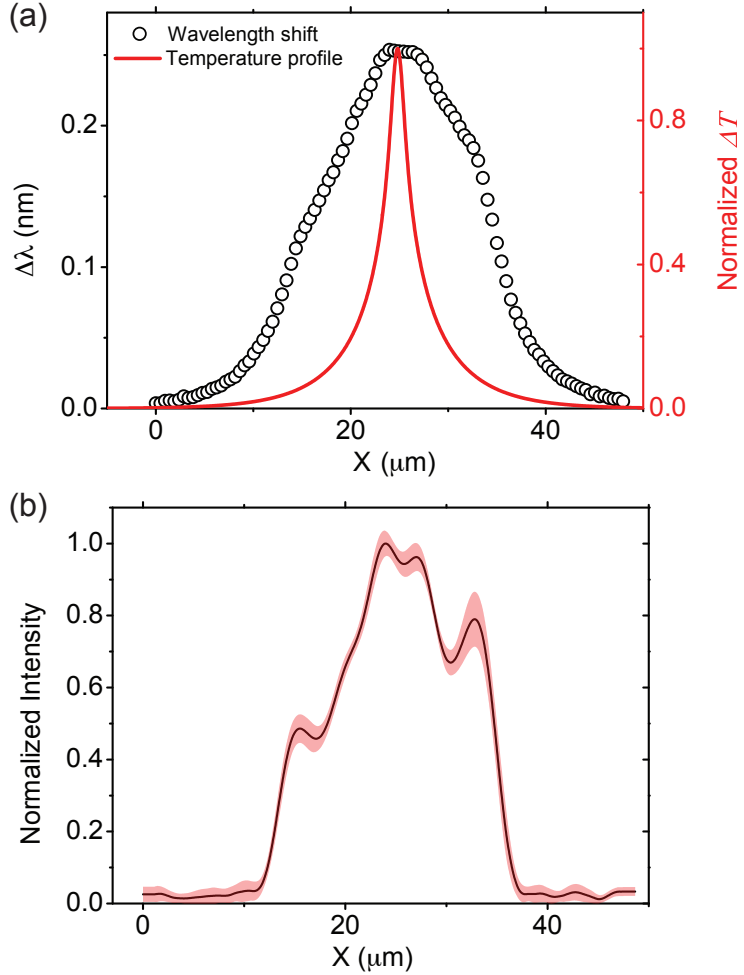


Figure 4.4: (a) Black circles: wavelength shift versus pump spot position of 5 independent measurements. The standard deviation is approximately equal to the symbol size. Red curve: temperature distribution along the waveguide direction. (b) Black curve: reconstructed mode profile along the waveguide direction. Pink bar: $3\sigma_E$ confidence interval.

We scan our pump beam along the waveguide from $x = 0 \mu\text{m}$ to $x = 48.7 \mu\text{m}$. The shift in wavelength of the mode versus pump position is shown in Fig. 4.4(a).

We see that the wavelength shift varies with the pump position. The maximum shift is observed when the pump is around the middle of the waveguide. This shows the mode is localized in the center part of the waveguide. The temperature distribution caused by the pump beam is calculated using the finite element method (COMSOL) as in Ref. 12. Following the same procedures, we have simulated the temperature distribution in the waveguide, shown in Fig. 4.4(a). We see that although the temperature distribution has a relatively narrow peak, it has a considerably wide base. This indicates that the envelope function of the random localized mode is blurred by the temperature profile. Thus, in order to reconstruct the mode profile of the disorder-induced localized mode, deconvolution is needed.

We perform the deconvolution procedures in the Fourier domain. Using the notation \mathcal{F} to represent Fourier transform, we define $I(f_x) = \mathcal{F}\{|\mathbf{E}^X(x)|^2\}$, $S(f_x) = \mathcal{F}\{\Delta\lambda(x)\}$ and $H(f_x) = \mathcal{F}\{\delta T^X(x)\}$. Before the Fourier transform, we interpolate the measured wavelength shift to match the resolution of the simulated temperature profile. $I(f_x)$ is obtained by

$$I(f_x) = \frac{S(f_x)}{H(f_x)} G(f_x), \quad (4.3)$$

here $G(f_x)$ is a Butterworth filter. The cutoff of the filter is determined by $\text{SNR}(f_x)$, which in our case is defined as $\text{SNR}(f_x) = \frac{|\bar{S}(f_x)|^2}{\text{Var}[S(f_x)]}$. The cutoff of $G(f_x)$ is selected at the frequency where $\text{SNR}(f_x) = 1$. For our experimental data, $f_{\text{cutoff}} = 0.4 \mu\text{m}^{-1}$. From the cut off frequency we estimated our resolution to be $2.5 \mu\text{m}$ which is f_{cutoff}^{-1} . $|\mathbf{E}^X(x)|^2$ can be obtained by $\mathcal{F}^{-1}\{I(f_x)\}$.

Using the procedures mentioned above, we deconvolve the wavelength shifts obtained from 5 measurements on the same structure. After the deconvolution, we first calculate the mean value and standard error of the 5 results. Secondly, we estimated the upper and lower confidence limits of the reconstructed signal as $|\mathbf{E}^X(x)|_{\pm}^2 = |\bar{\mathbf{E}}^X(x)|^2 \pm 3\sigma_E(|\mathbf{E}^X(x)|^2)$. $|\bar{\mathbf{E}}^X(x)|^2$ is the mean of the deconvolved intensities, $\sigma_E(|\mathbf{E}^X(x)|^2)$ is the standard error. Thirdly, we used simple moving average to smooth $|\mathbf{E}^X(x)|_{\pm}^2$. The averaging period is $2.5 \mu\text{m}$. The smoothed results are the final upper and lower limits of the reconstructed mode profile. Finally, we calculate the final reconstructed profile as the mean of the upper and lower limits. The final reconstructed intensity profile is presented in Fig. 4.4(b). In Fig. 4.4(b), we see the intensity profile is narrower than the wavelength shift and it has multiple peaks in the center part. Wiggles outside the center part of the mode are due to Gibbs oscillation [17].

The disorder-induced mode profile in Fig. 4.4(b) is localized mainly from around $x = 12 \mu\text{m}$ to around $x = 38 \mu\text{m}$. The envelop function has a complicated profile with several local maxima, which are well resolved by our method.

4.5 Numerical Validation

In order to validate our method against a “ground truth” which is a mode profile that we know, we performed a direct simulation of our experiments.

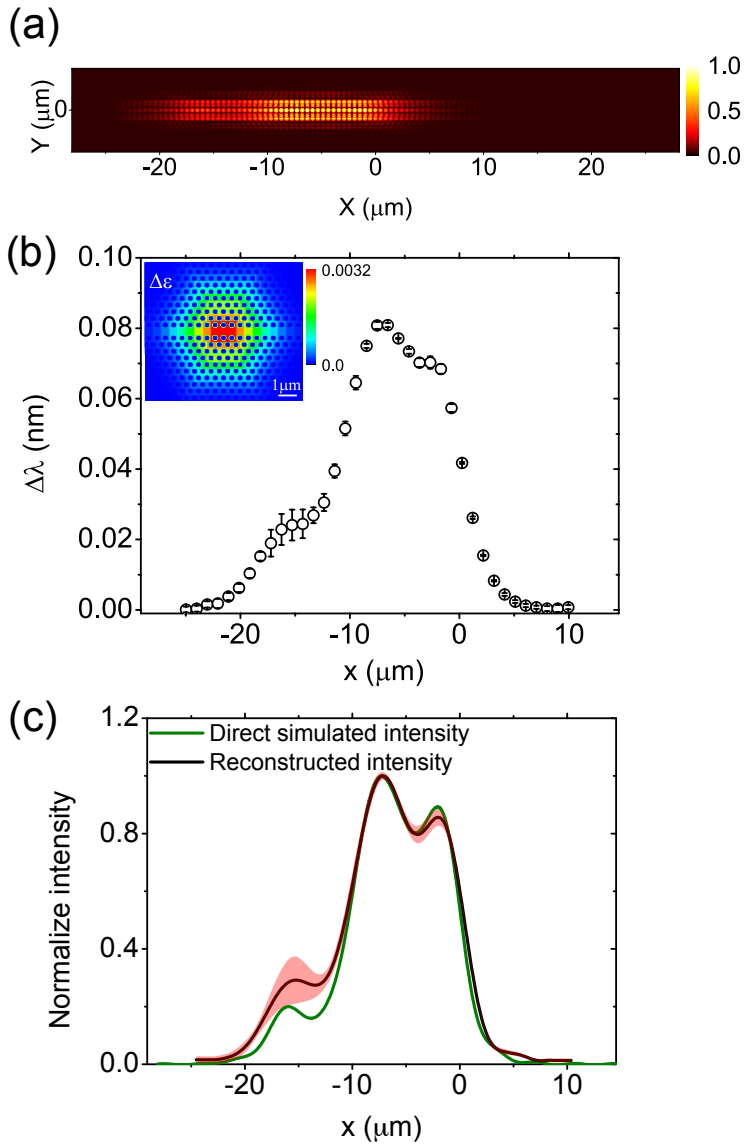


Figure 4.5: Numerical validation of the mode reconstruction method. (a) Amplitude of the y component of the electric field $|E_y|$ of a simulated mode. (b) Black circles: wavelength shift versus pump spot position. The effect of pump is simulated by the relative change of dielectric constant distribution as shown in the top left. (c) Green curve: directly simulated intensity projected along the x axis. Black curve: reconstructed profile from simulated measurement.

The direct simulations are done in two dimensional finite difference time domain simulations [18]. In our simulations, the lattice constant a of the struc-

ture and the radius of the holes are uniformly randomly distributed within the range of 485.00 ± 4.85 nm and 121.2500 ± 1.2125 nm respectively. The length of the waveguide is $106\text{ }\mu\text{m}$. For one single realization, in order to obtain the field patterns of disorder-induced modes we follow the following procedures. Firstly, multiple sources with broad linewidth are randomly placed in the waveguide to excite the disorder induced localized modes. Meanwhile, multiple detectors are placed randomly in the waveguide to analyze the field evolution. In such way, we can obtain the resonance frequencies of the disorder-induced modes. Secondly, we place multiple sources with narrow linewidth in waveguides in a random way. The sources are spectrally matched to only one of the resonances extracted before. In such way, we can obtain the field pattern of the disorder-induced modes. A disorder-induced localized mode in one random realization with wavelength 2172.845 nm is shown in Fig. 4.5(a). From the field pattern, we see the simulated disorder-induced localized mode has a periodical oscillation very similar to the waveguide mode, except it is localized rather than extended through the waveguide.

We create a profile of $\Delta\epsilon(x, y)$ to simulate the change due to the pump, which is shown in the top left of Fig. 4.5(b). It is a discretized Gaussian function with sharp stop. The width of the Gaussian function is $3.5\text{ }\mu\text{m}$. The total width of the truncated function is $10.2\text{ }\mu\text{m}$. Care has been taken to avoid overlapping boundaries as they lead to unwanted changes in FDTD simulations that are equivalent to extra disorder in the subpixel averaging [19]. The pump scan in the experiment is simulated by changing the center of $\Delta\epsilon$. The shift in wavelength versus the pump position of the simulated experiment is shown in Fig. 4.5(b). The fine features in Fig. 4.5(a) are lost because of the width of the simulated pump beam. From Fig. 4.5(b), we can only obtain the information of where the mode is localized. By performing the same procedure as for the experimental data, we deconvolve the data in Fig. 4.5(b) with the cross section of $\Delta\epsilon$. The result is shown in Fig. 4.5 (c). The reconstructed intensity has 3 resolvable peaks. We also plot the integrated intensity along y axis of the mode which is the “ground truth” in Fig. 4.5 (b). We see the reconstructed intensity is very similar to the “ground truth”. It is noticed that there is an overestimation of the amplitude around position $x = -16\text{ }\mu\text{m}$. This is because of interaction of a nearby mode with wavelength of 2171.437 nm. When the pump is moved around $x = -16\text{ }\mu\text{m}$, the mode with short wavelength has a larger response than the mode we want to retrieve. This causes a weak hybridization of the modes. As a consequence, the mode we want to retrieve experiences a bigger shift than expected from the first order perturbation theory (Eq. 4.1). Nevertheless, the features and positions of the local peaks are very well resolved.

4.6 Conclusion

In conclusion, we have successfully retrieved the spatial profile of a random localized mode in a PhCWG by performing spatially dependent thermal tuning and deconvolution procedures. A direct simulation of our experiment shows that the

deconvolution procedure in our method gives a reconstructed mode profile close to the “ground truth”. Beside measuring the intensity profile of disorder induced modes in PhCWGs which is a 1D system, our method can be straightforwardly applied to higher dimensional disordered system [20, 21]. Accurately retrieving the mode profiles is an essential step towards engineering the functionality of the disordered photonic systems [15, 22].

Bibliography

- [1] P. W. Anderson, *Absence of diffusion in certain random lattices*, Phys. Rev. **109**, 1492 (1958). — p.47.
- [2] A. Lagendijk, B. van Tiggelen, and D. S. Wiersma, *Fifty years of Anderson localization*, Physics Today **62**, 24 (2009). — p.47.
- [3] P. W. Anderson, *The size of localized States near the mobility edge*, Proc. Natl. Acad. Sci. **69**, 1097 (1972). — p.47.
- [4] S. John, *Electromagnetic Absorption in a Disordered Medium near a Photon Mobility Edge*, Phys. Rev. Lett. **53**, 2169 (1984). — p.47.
- [5] J. D. Joannopoulos, S. G. Johnson, J. N. Winn, and R. D. Meade , *Photonic Crystals: Molding the Flow of Light* (Princeton University Press, Princeton, 2008). — p.47.
- [6] M. Patterson, S. Hughes, S. Combrié, N.-V.-Q. Tran, A. De Rossi, R. Gabet, and Y. Jaouén, *Disorder-Induced Coherent Scattering in Slow-Light Photonic Crystal Waveguides*, Phys. Rev. Lett. **102**, 253903 (2009). — p.47.
- [7] M. Spasenović, D. M. Beggs, P. Lalanne, T. F. Krauss, and L. Kuipers, *Measuring the spatial extent of individual localized photonic states*, Phys. Rev. B **86**, 155153 (2012). — p.47.
- [8] S. R. Huisman, G. Ctistis, S. Stobbe, A. P. Mosk, J. L. Herek, A. Lagendijk, P. Lodahl, W. L. Vos, and P. W. H. Pinkse, *Measurement of a band-edge tail in the density of states of a photonic-crystal waveguide*, Phys. Rev. B **86**, 155154 (2012). — p.47.
- [9] A. F. Koenderink, A. Lagendijk, and W. L. Vos, *Optical extinction due to intrinsic structural variations of photonic crystals*, Phys. Rev. B **72**, 153102 (2005). — p.47.
- [10] L. Sapienza, H. Thyrrstrup, S. R. Stobbe, P. D. Garcia, S. Smolka, and P. Lodahl, *Cavity quantum electrodynamics with Anderson-Localized Modes*, Science **1027**, 1352 (2010). — p.47.
- [11] R. Bruck, B. Mills, B. Troia, D. J. Thomson, F. Y. Gardes, Y. Hu, G. Z. Mashanovich, V. M. N. Passaro, G. T. Reed, and O. L. Muskens, *Device-level characterization of the flow of light in integrated photonic circuits using ultrafast photomodulation spectroscopy*, Nat. Photonics **9**, 54 (2014). — p.47.
- [12] S. Sokolov, J. Lian, E. Yüce, S. Combrié, G. Lehoucq, A. De Rossi, and A. P. Mosk, *Local thermal resonance control of GaInP photonic crystal membrane cavities using ambient gas cooling*, Appl. Phys. Lett. **106**, 171113 (2015). — p.48.
- [13] S. Combrié, Q. V. Tran, A. De Rossi, C. Husko, and P. Colman, *High qual-*

- ity *GaInP nonlinear photonic crystals with minimized nonlinear absorption*, Appl. Phys. Lett. **95**, 221108 (2009). — p.48.
- [14] N. Caselli, F. Intonti, C. Bianchi, F. Riboli, S. Vignolini, L. Balet, L. H. Li, M. Francardi, A. Gerardino, A. Fiore, and M. Gurioli, *Post-fabrication control of evanescent tunnelling in photonic crystal molecules*, Appl. Phys. Lett. **101**, 211108 (2012). — p.48.
 - [15] F. Riboli, N. Caselli, S. Vignolini, F. Intonti, K. Vynck, P. Barthelemy, A. Gerardino, L. Balet, L. H. Li, A. Fiore, M. Gurioli, and D. S. Wiersma, *Engineering of light confinement in strongly scattering disordered media*, Nat. Mater. **13**, 720 (2014). — p.48, 55.
 - [16] A. E. Miroshnichenko, S. Flach, and Y. S. Kivshar, *Fano resonances in nanoscale structures*, Rev. Mod. Phys. **82**, 2257 (2010). — p.49.
 - [17] George B. Arfken, Hans J. Weber , *Mathematical Methods for Physicists*, 3rd ed (Academic Press, Orlando, 1985). — p.52.
 - [18] A. F. Oskooi, D. Roundy, M. Ibanescu, P. Bermel, J. Joannopoulos, and S. G. Johnson, *Meep: A flexible free-software package for electromagnetic simulations by the FDTD method* , Comput. Phys. Commun. **181**, 687 (2010). — p.53.
 - [19] A. Farjadpour, D. Roundy, A. Rodriguez, M. Ibanescu, P. Bermel, J. D. Joannopoulos, S. G. Johnson, and G. Burr, *Improving accuracy by subpixel smoothing in FDTD*, Opt. Lett. **31**, 2972 (2006). — p.54.
 - [20] R. Sarma, A. Yamilov, P. Neupane, B. Shapiro, and H. Cao, *Probing long-range intensity correlations inside disordered photonic nanostructures*, Phys. Rev. B **90**, 014203 (2014). — p.55.
 - [21] K. Vynck, M. Burresi, F. Riboli, and D. S. Wiersma, *Photon management in two-dimensional disordered media*, Nat. Mater. **11**, 1017 (2012). — p.55.
 - [22] D. S. Wiersma, *Disordered photonics*, Nat. Photonics **7**, 188 (2013). — p.55.

CHAPTER 5

Hybridization of disorder-induced localized modes in photonic crystal waveguides by adaptive tuning

Here we experimentally demonstrate the hybridization of disorder-induced localized modes to extended resonant modes in a photonic crystal waveguide. The resonances show avoided crossings which are the evidence of hybridization. Furthermore, we reconstruct the mode profiles of the hybridized resonances and find they extend through the waveguide.

5.1 Introduction

Multiple-nanocavity systems give rise to many intriguing observations and applications. For example, one-dimensional coupled-cavity arrays, also named coupled resonator optical waveguides (CROW) [1–5], can be used as optical memory devices [6]. A multiple-cavity system with quantum dots is a quantum network when the light and matter interaction is strong enough [7]. Even the simplest multiple-nanocavity system, two coupled cavities system, brings out fascinating applications and phenomena such as sources of entangled photon pairs [8], polariton condensation [9] and spontaneous mirror-symmetry breaking [10]. However, unavoidable disorder limits the functionality by causing unwanted random shifts of the resonance wavelengths.

Recently, it was realized that disorder-induced random resonances in photonic crystal waveguides (PhCWGs) [11–13] are natural high quality factor (Q) cavities [14, 15]. They provide an alternative way to construct a multiple-resonator system. To achieve functionality such as transmission, the first step is to align the spatially and spectrally randomly distributed resonances to the same frequency (Fig. 5.1).

Here we experimentally demonstrate the alignment of the frequencies of two disorder-induced resonances in a photonic crystal waveguide, causing them to form hybridized states. Furthermore, we reconstruct the mode profiles of the hybridized modes.

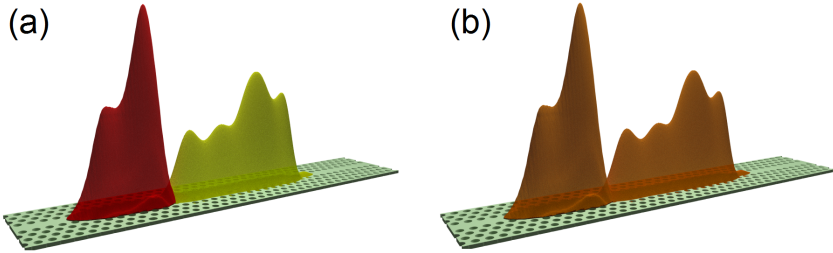


Figure 5.1: Carton depicting two disorder-induced modes in a photonic crystal waveguide before hybridization (a) and after hybridization (b). Different colors indicate different frequencies of the modes.

5.2 Sample and experimental setup

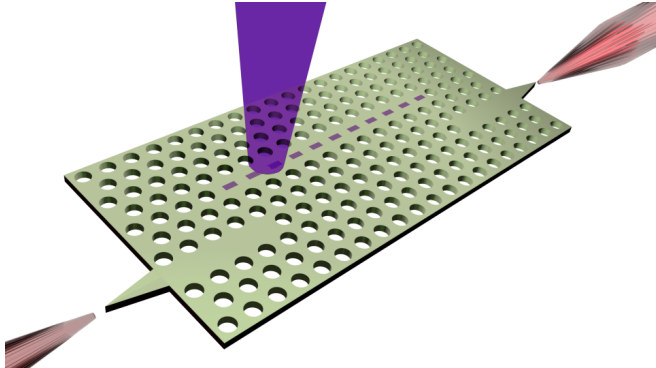


Figure 5.2: Schematic representation of the sample and experimental setup. The green membrane represents the sample. The two cones with red color inside represent the polarization maintaining lensed fibers (PMF). The purple cone represents the focused pump beam. The dashed line indicates the trace along which the pump is moved.

The schematic representation of the experimental setup and sample are shown in Fig. 5.2. The sample is a GaInP membrane structure [16] with thickness of 180 nm. Holes are etched on a triangle lattice with lattice constant $a = 485$ nm to form a photonic crystal structure. Three line defects form waveguides. The two waveguides which are in line are the carrier waveguides with a width of $W_1 = 1.1\sqrt{3}a$. The other waveguide is the barrier waveguide. The width of it is $W_0 = 0.98\sqrt{3}a$ and its length is $L = 106a$. Light from a tunable continuous wave (CW) infrared (IR) laser is coupled to the input carrier waveguide by a polarization maintaining lensed fiber (PMF) with numerical aperture (NA) of 0.55. A same type PMF is used to couple light from the waveguide to a photodiode. We focus a pump spot ($\lambda_{\text{pump}} = 405$ nm) from a CW diode laser on the surface of sample by an objective with 0.4 NA. The full width half maximum (FWHM) of the focus

is $0.83 \mu\text{m}$, and the power is $20 \mu\text{W}$. We use a spatial light modulator to move the pump light along the center line of the barrier waveguide. The sample is placed in a N_2 environment with oxygen concentration less than 0.03% for all measurements to reduce oxidation effects [17, 18].

5.3 Extraction of the profiles of overlapping random modes

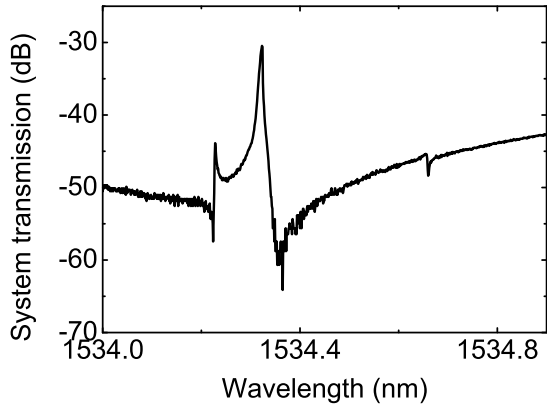


Figure 5.3: Reference transmission spectrum of the sample.

The reference transmission spectrum of our sample is plotted in Fig. 5.3. In the plot we see two transmission peaks at 1534.226 nm and 1534.321 nm , as well as one dip at 1534.659 nm . They correspond to the disorder-induced resonances. The reason why these resonances show different lineshapes is that the disorder-induced resonances interfere with the background signal in the spectrum with different phases [19].

When the sample is pumped, the disorder induced resonances shift to the red due to the temperature change of the sample [20], and the wavelength shifts are position dependent. In Fig. 5.4(a), we plot the wavelength of the resonances versus pump position. We see these three resonances have different dependence on the pump position. Here we focus on the resonance 1 and resonance 2. We see the maximum response of the pump for resonance 1 is around $x = 10 \mu\text{m}$ ($x = 0 \mu\text{m}$ is the beginning of the barrier waveguide), the maximum shift of resonance 2 occurs around $x = 25 \mu\text{m}$.

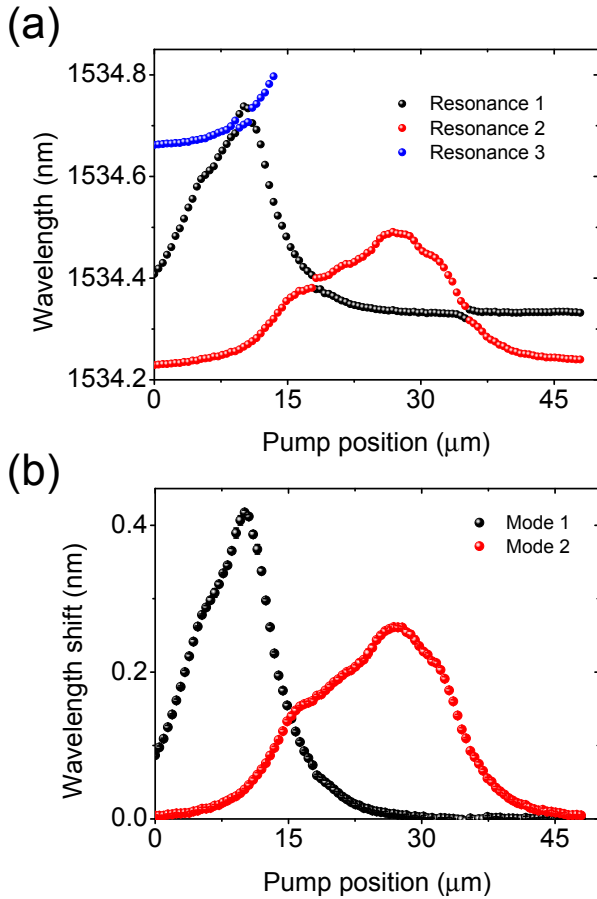


Figure 5.4: (a) Wavelengths of three resonances versus pump position.(b) Wavelength shift versus pump position for mode 1 and mode 2.

In Fig. 5.4(a), we observe avoided crossings of resonance 1 and 2 around $x = 18 \mu\text{m}$. First, these two modes start to approach each other in wavelength. However, when they come closer, we see that instead of intersecting with each other, a repulsion occurs. After that the wavelengths of resonance 1 and resonance 2 start to deviate quickly. When these avoided crossing happens, two resonances hybridize with each other. At the pump position where the spacing of the resonances has a minimum, the bare frequencies of the two modes are aligned to the same wavelength and the modes are hybridized completely. In Fig. 5.4(a), avoid crossings also happen at other pump positions. One happens around $x = 9 \mu\text{m}$ between resonances 1 and 3. The other happens around $x = 35 \mu\text{m}$ between resonances 1 and 2. Thus, at these pump positions the resonances of the disorder-induced modes hybridize completely.

5.4 Reconstruction of the mode profiles of hybridized resonances.

After the hybridization of the modes, the next step is to obtain the mode profiles of the hybridized modes. To reconstruct the mode profiles of the hybridized modes we need to know the mode profiles of the localized modes. From chapter 4, we know the mode profile can be reconstructed by deconvolving the wavelength shift of the mode with the distribution of the temperature change induced by the pump in the regime where the perturbation theory is valid. However, perturbation theory is not valid when hybridized modes are present.

To apply perturbation theory, we have to remove the effect of coupling of the modes. This can be done with the help of coupled mode theory [21].

The frequencies of the hybridized modes according to coupled mode theory can be expressed as,

$$\omega_{\pm} = \frac{\omega_1 + \omega_2}{2} \pm \sqrt{\left(\frac{\omega_1 - \omega_2}{2}\right)^2 + \left(\frac{\Gamma}{2}\right)^2}. \quad (5.1)$$

Here ω_{\pm} represent the frequencies of the hybridized modes corresponding to $\omega_{\pm} = 2\pi c/\lambda_{\mp}$. Γ is the coupling rate between the cavities. ω_1 and ω_2 are the bare frequencies of the isolated modes. From Eq. (5.1), we can also easily find out that

$$|\Gamma| = |\omega_+ - \omega_-|_{\min}. \quad (5.2)$$

From the data plotted in Fig.5.4(a) where the avoid crossing happens, we obtain Γ by Eq. (5.2). We can then retrieve ω_1 and ω_2 at any pump position with the help of Eq. (5.1).

After retrieving the wavelengths of the isolated modes, we plot the wavelength shifts of mode 1 and 2 in Fig. 5.4(b). Compared to Fig. 5.4(a), the influences of coupling have been eliminated. Now plotted on the same offset, we see the the wavelength shift of mode 1 is bigger than mode 2 and has a narrower profile than mode 2, which indicates that mode 1 has a smaller mode volume.

Using the deconvolution procedure discussed in chapter 4, we retrieve the mode profiles of isolated mode 1 and 2, which are presented in Fig. 5.5(a). We see that for both modes the mode profiles are much narrower than the pump wavelength response plot in Fig. 5.4(b). In the mode profile of mode 1, instead of one broad response, two peaks are clearly resolved. For mode 2, we resolve 4 distinguishable peaks.

After knowing the profiles of mode 1 and mode 2, we can reconstruct the mode profiles of the hybridized modes with the help of coupled mode theory. The intensity of the hybridized mode can be expressed as

$$I_{\lambda_{\pm}} = I_1(x) + I_2(x) \pm \sqrt{I_1(x)I_2(x)}. \quad (5.3)$$

Here λ_+ is the mode with longer wavelength, λ_- is the one with shorter wavelength. The argument of the sign selection of the modes is the following. In the Fourier space (k space), the mode with a node in the envelop function has a

broader spread. Since the waveguide mode has a negative dispersion (Fig. 1.1), a broader spread results in a higher energy.

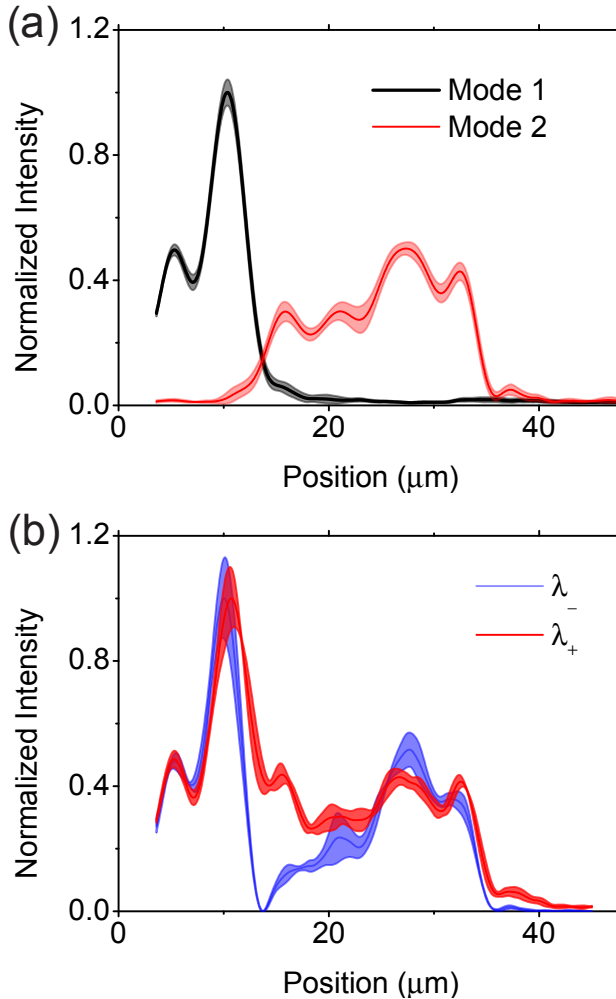


Figure 5.5: (a) Reconstructed mode profiles of isolated modes 1 and 2. (b) Reconstructed mode profiles of the hybridized modes. The grey, pink, blue and red bands represent the estimated errors.

In Fig. 5.5(b), we plot the mode profiles of the two hybridized modes. We see that now we have two extended modes in the waveguide with a much larger width than the localized modes 1 and 2. The main difference between these two modes is that the hybridized mode with shorter wavelength has a zero intensity around $x = 13 \mu\text{m}$.

5.5 Conclusion

In conclusion, we have shown that we have successfully aligned the wavelengths of two disorder-induced resonances in a photonic crystal waveguides. Taking into account the hybridization of the modes, using coupled mode theory, we have retrieved the wavelength shifts of the two isolated modes and reconstructed the mode profiles of them separately. This extends the possibilities of the application of the method we have shown in chapter 4. Further more, using coupled mode theory we have retrieved the mode profiles of the hybridized modes. Our work allows one to investigate the physics of coupled resonators [8–10] in a random system. In the future we expect more complicated multiple-cavity system can be built up from disorder-induced resonances from PhCWGs.

Bibliography

- [1] A. Yariv, Y. Xu, R. K. Lee, and A. Scherer, *Coupled-resonator optical waveguide: a proposal and analysis*, Opt. Lett. **24**, 711 (1999). — p.59.
- [2] M. Notomi, E. Kuramochi, and T. Tanabe, *Large-scale arrays of ultrahigh-Q coupled nanocavities*, Nat. Photonics **2**, 741 (2008). — p.59.
- [3] F. Xia, L. Sekaric, and Y. Vlasov, *Ultracompact optical buffers on a silicon chip*, Nat. Photonics **1**, 65 (2007). — p.59.
- [4] C. Taddei, L. Zhuang, M. Hoekman, A. Leinse, R. Oldenbeuving, P. van Dijk, and C. Roeloffzen, in *Microwave photonics (mwp) and the 2014 9th asia-pacific microwave photonics conference (apmp) 2014 international topical meeting on* (IEEE, Sendai, 2014), pp. 44–47. — p.59.
- [5] C. Taddei, L. Zhuang, M. Hoekman, C. Roeloffzen, and K.-J. Boller, in *2015 european conference on lasers and electro-optics - european quantum electronics conference* (Optical Society of America, Munich, 2015). — p.59.
- [6] E. Kuramochi, K. Nozaki, A. Shinya, K. Takeda, T. Sato, S. Matsuo, H. Taniyama, H. Sumikura, and M. Notomi, *Large-scale integration of wavelength-addressable all-optical memories on a photonic crystal chip*, Nat. Photonics **8**, 474 (2014). — p.59.
- [7] H. J. Kimble, *The quantum internet*, Nature **453**, 1023 (2008). — p.59.
- [8] A. Dousse, J. Suffczyński, A. Beveratos, O. Krebs, A. Lemaître, I. Sagnes, J. Bloch, P. Voisin, and P. Senellart, *Ultrabright source of entangled photon pairs*, Nature **466**, 217 (2010). — p.59, 65.
- [9] M. Galbiati, L. Ferrier, D. D. Solnyshkov, D. Tanese, E. Wertz, A. Amo, M. Abbarchi, P. Senellart, I. Sagnes, A. Lemaître, E. Galopin, G. Malpuech, and J. Bloch, *Polariton condensation in photonic molecules*, Phys. Rev. Lett. **108**, 126403 (2012). — p.59, 65.
- [10] P. Hamel, S. Haddadi, F. Raineri, P. Monnier, G. Beaudoin, I. Sagnes, A. Levenson, and A. M. Yacomotti, *Spontaneous mirror-symmetry breaking in coupled photonic-crystal nanolasers*, Nat. Photonics **9**, 311 (2015). — p.59, 65.
- [11] M. Patterson, S. Hughes, S. Combrié, N.-V.-Q. Tran, A. De Rossi, R. Gabet, and Y. Jaouén, *Disorder-Induced Coherent Scattering in Slow-Light Photonic Crystal Waveguides*, Phys. Rev. Lett. **102**, 253903 (2009). — p.59.
- [12] M. Spasenović, D. M. Beggs, P. Lalanne, T. F. Krauss, and L. Kuipers, *Measuring the spatial extent of individual localized photonic states*, Phys. Rev. B **86**, 155153 (2012). — p.59.
- [13] S. R. Huisman, G. Ctistis, S. Stobbe, A. P. Mosk, J. L. Herek, A. Lagendijk, P. Lodahl, W. L. Vos, and P. W. H. Pinkse, *Measurement of a band-edge*

- tail in the density of states of a photonic-crystal waveguide*, Phys. Rev. B **86**, 155154 (2012). — p.59.
- [14] D. S. Wiersma, *Physics. Random quantum networks*, Science (New York, N.Y.) **327**, 1333 (2010). — p.59.
 - [15] L. Sapienza, H. Thyrrstrup, S. R. Stobbe, P. D. Garcia, S. Smolka, and P. Lodahl, *Cavity quantum electrodynamics with Anderson-Localized Modes*, Science **1027**, 1352 (2010). — p.59.
 - [16] S. Combrié, Q. V. Tran, A. De Rossi, C. Husko, and P. Colman, *High quality GaInP nonlinear photonic crystals with minimized nonlinear absorption*, Appl. Phys. Lett. **95**, 221108 (2009). — p.60.
 - [17] N. Caselli, F. Intonti, C. Bianchi, F. Riboli, S. Vignolini, L. Balet, L. H. Li, M. Francardi, A. Gerardino, A. Fiore, and M. Gurioli, *Post-fabrication control of evanescent tunnelling in photonic crystal molecules*, Appl. Phys. Lett. **101**, 211108 (2012). — p.61.
 - [18] F. Riboli, N. Caselli, S. Vignolini, F. Intonti, K. Vynck, P. Barthelemy, A. Gerardino, L. Balet, L. H. Li, A. Fiore, M. Gurioli, and D. S. Wiersma, *Engineering of light confinement in strongly scattering disordered media*, Nat. Mater. **13**, 720 (2014). — p.61.
 - [19] A. E. Miroshnichenko, S. Flach, and Y. S. Kivshar, *Fano resonances in nanoscale structures*, Rev. Mod. Phys. **82**, 2257 (2010). — p.61.
 - [20] S. Sokolov, J. Lian, E. Yüce, S. Combrié, G. Lehoucq, A. De Rossi, and A. P. Mosk, *Local thermal resonance control of GaInP photonic crystal membrane cavities using ambient gas cooling*, Appl. Phys. Lett. **106**, 171113 (2015). — p.61.
 - [21] H. A. Haus and W. Huang, *Coupled-mode theory*, Proc. IEEE **79**, 1505 (1991). — p.63.

CHAPTER 6

Fano lines of waveguide-cavities systems: measurements, modeling and manipulation of the Fano lineshapes

Reflection spectra of a waveguide-cavities system show several Fano resonances. This Fano lineshape makes interpretation of measured spectra complicated. Here we show our measurements of Fano lines from a directly coupled waveguide-cavities system and an analytical model that accurately characterizes the reflection spectra. A simple scheme of manipulating the Fano lineshape proposed from our model is demonstrated experimentally.

6.1 Introduction

Photonic crystal (PhC) [1] cavities are of tremendous interest for device applications due to their fascinating properties such as small mode volume and high quality factor (Q) [2–4]. Multiple-cavity systems are great platforms to study fundamental physics and build all optical devices [5–10]. Thus, characterization of multiple-cavity systems composed of photonic crystal cavities is of great importance.

Reflection measurement is a typical way of characterizing resonant systems. The geometry of a reflection measurement in a direct coupled system we use is shown in Fig. 6.1. From a reflection spectrum, the resonant width and frequency can be obtained. For a resonant system, the line shape is generally described by a Lorentzian function that is perfectly symmetric. Thus, a set of Lorentzian dips are expected to be observed in the reflection spectrum for a direct coupled waveguide-cavities system. However, in reality a set of asymmetric line shapes are usually observed. An example is shown in Fig. 6.2. The asymmetric line shape originates from Fano interference [11, 12]. When a narrower resonance interferes with a continuum, sharp asymmetric Fano resonances are observed [11, 12]. In many cases, the Fano line shape is preferred to the Lorentzian shape. For example, for optical switching Fano resonances give much larger switching contrast [13]. For a given cavity, by deliberate design of the coupling to the continuum, different Fano lineshapes can be obtained [14]. However, when the structure is fabricated it is very difficult to change the Fano lineshape without changing the frequency of the resonance because this requires to change the

properties of the continuum.

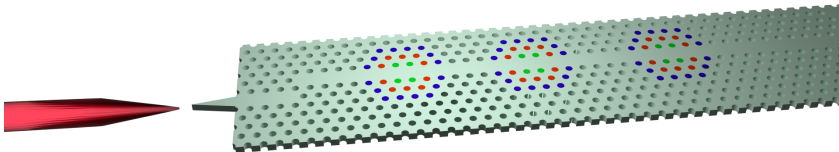


Figure 6.1: A schematic representation of the sample and experimental setup. The sample is represented by the green membrane structure. In the barrier waveguide (middle line defect), three cavities have been created by shifting the holes around the waveguided in a tapered way. The shift of the green holes are $S_1 = 0.0124a$, the shifts of the red and blue holes are $2/3 S_1$ and $1/3 S_1$, and a is the lattice constant. The red cone next to the sample represents a polarization maintaining lensed fiber (PMF) used to couple light into the membrane.

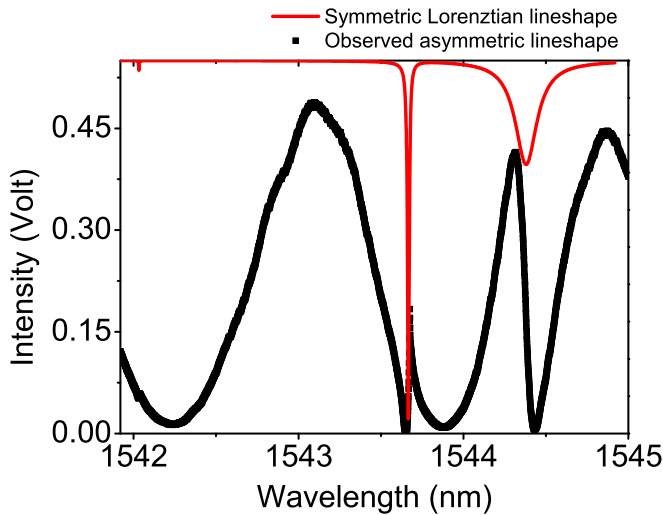


Figure 6.2: Reflection spectrum of a direct coupled waveguide and multiple-cavity system. Black square: measured spectrum. Red line: expected spectrum in absence of Fano interference.

In this work, we experimentally and theoretically investigate Fano resonances in a direct coupled waveguide and multiple-cavity system in a PhC membrane structure. We measure the Fano lineshapes and manipulate the Fano lineshape by tuning the resonances. We create an analytical model which uncovers the origin of the Fano resonances, and it accurately reproduces our experimental results. With the help of our model, we propose and experimentally demonstrate a way of directly manipulating the Fano lineshape without tuning the resonances.

6.2 Theoretical model

We first introduce the theoretical model we create to characterize the system. The schematic of the system we consider is shown in Fig. 6.3. Different from the typical scheme for direct coupled waveguide-systems, here we include the lensed fiber used to couple light into waveguide. Light propagation can be separated into three processes. The first process is the light coupling between the lensed fiber and the input waveguide. The second process is the light transport in the input waveguide. The last process is the light coupling between the waveguides and cavities. We use a transfer matrix method to model all these processes. The transfer matrix connects the fields of forward and backward propagating waves from left side to right side,

$$\begin{pmatrix} S_{R+} \\ S_{R-} \end{pmatrix} = \mathbf{M} \begin{pmatrix} S_{L+} \\ S_{L-} \end{pmatrix}. \quad (6.1)$$

Here $S_{R\pm}$ is the forward (backward) propagating wave on the right side, $S_{L\pm}$ is the forward (backward) propagating wave on the left side. \mathbf{M} is the transfer matrix that links them.

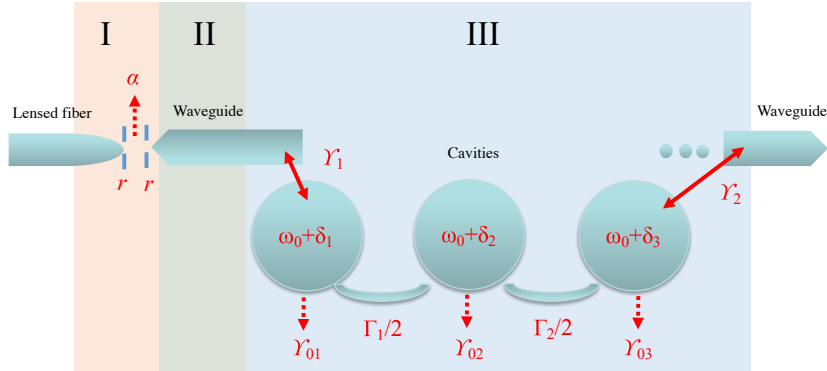


Figure 6.3: Schematic of the optical system including coupled cavities direct coupled to waveguides. A lensed fiber as a measurement device is also taken into account in the system.

6.2.1 Process I: coupling between the measurement device and waveguide

In the process of coupling between the measurement device (lensed fiber) and waveguide, there are a few physical events we have to consider. The first is the reflection at the boundaries between the lensed fiber and air, and between air and the facet of the input waveguide. The second is the coupling loss. The third is the light propagation in the air.

Reflection at the boundaries can be model as reflection from partial reflection mirrors. The transfer matrix of a partial reflection mirror has the following form

[15],

$$\mathbf{M}_{\text{pr}} = \frac{1}{i\sqrt{1-r^2}} \begin{pmatrix} -1 & -r \\ r & 1 \end{pmatrix}. \quad (6.2)$$

The r here is the amplitude reflection coefficient. In the model here for simplicity, we assume it is the same for both boundaries.

The propagation of light in the air gap is modeled as,

$$\mathbf{M}_{\text{Air}} = \begin{pmatrix} e^{i\frac{\omega}{c}\Delta} & 0 \\ 0 & e^{-i\frac{\omega}{c}\Delta} \end{pmatrix}, \quad (6.3)$$

where Δ is the length of the air gap.

The corresponding physical process of the coupling loss can be modeled as the matrix below,

$$\mathbf{M}_{\text{loss}} = \begin{pmatrix} \sqrt{1-\alpha} & 0 \\ 0 & \frac{1}{\sqrt{1-\alpha}} \end{pmatrix}, \quad (6.4)$$

where α is the power loss in the coupling process.

The matrix that describes the process I is the multiplication of the matrices discussed above, it is

$$\mathbf{M}_{\text{I}} = \mathbf{M}_{\text{pr}} \cdot \mathbf{M}_{\text{loss}} \cdot \mathbf{M}_{\text{Air}} \cdot \mathbf{M}_{\text{pr}} \quad (6.5)$$

6.2.2 Process II: propagation in the photonic crystal waveguide

The propagation in the photonic crystal waveguide has the same form as Eq. (6.3). However, the dispersion of the waveguide has to be considered. The matrix is

$$\mathbf{M}_{\text{II}} = \begin{pmatrix} e^{ik_b(\omega)L_l} & 0 \\ 0 & e^{-ik_b(\omega)L_l} \end{pmatrix} \quad (l = 1, 2). \quad (6.6)$$

$k_b(\omega)$ is the Bloch wave vector of the wave in the waveguide, it is a dispersive quantity. L_l is the length of waveguide l . It is known that close to the band edge, the dispersion of the photonic crystal can be expressed as $\omega = \omega_{\text{edge}} + (k_b - \pi/a)^2/(2m)$ [16, 17], where ω is the frequency of the waveguide mode, ω_{edge} is the frequency of the band edge of the waveguide mode, $m = (\partial^2\omega/\partial^2k)^{-1}$ is the effective photon mass close to the band edge. As a result, we can express the Bloch wave vector k_b as $k_b = \pi/a - \sqrt{2m(\omega - \omega_{\text{edge}})}$.

6.2.3 Process III: light coupling between the waveguides and cavities.

To derive the matrix which describes the light coupling between the waveguides and cavities, we use the temporal coupled equations to describe the coupling between the cavities and waveguides. In the equations, we only consider the coupling between the first (last) cavity and input (output) waveguide, with coupling rates are γ_1 and γ_2 respectively. We use $a_j(t)$ ($j = 1, 2, 3$) to denote the time evolution of the field in cavity j , and $S_{l\pm}$ ($l = 1, 2$) to denote the amplitude of the mode in waveguide l . $l = 1$ represents the input waveguide and $l = 2$ represents

the output waveguide. The "±" represents forward (backward) propagation. As discussed in the chapter 2, the following equations describe the dynamics of the system [1, 18],

$$\frac{da_1}{dt} = i(\omega_0 + \delta\omega_1)a_1 - (\gamma_{01} + \gamma_1)a_1 + \sqrt{2\gamma_1}S_{1+} + i\frac{\Gamma_1}{2}a_2, \quad (6.7a)$$

$$\frac{da_2}{dt} = i(\omega_0 + \delta\omega_2)a_2 - \gamma_{01}a_1 + i\frac{\Gamma_1}{2}a_1 + i\frac{\Gamma_2}{2}a_3, \quad (6.7b)$$

$$\frac{da_3}{dt} = i(\omega_0 + \delta\omega_3)a_3 - (\gamma_{03} + \gamma_2)a_1 + \sqrt{2\gamma_2}S_{2-} + i\frac{\Gamma_2}{2}a_2, \quad (6.7c)$$

$$S_{1-} = -S_{1+} + \sqrt{2\gamma_1}a_1, \quad (6.7d)$$

$$S_{2-} = -S_{2+} + \sqrt{2\gamma_2}a_3. \quad (6.7e)$$

In Eq. (6.7), ω_0 is the intended intrinsic frequency of the cavities. $\delta\omega_j$ ($j = 1, 2, 3$) represents the frequency deviation of cavity j to the actual bare resonance frequency due to fabrication disorder. We define $\omega_j = \omega_0 + \delta\omega_j$. γ_{0j} is the intrinsic loss rate of cavity j . Γ_1 is the coupling rate between cavity 1 and 2, Γ_2 is the coupling rate between cavity 2 and 3. As discussed in chapter 2, Eq. (6.7) can be written in a matrix format,

$$\mathbf{M} \times \begin{pmatrix} A_1 \\ A_2 \\ A_3 \\ S_{1-} \\ S_{2+} \end{pmatrix} = \begin{pmatrix} -\sqrt{2\gamma_1}S_{1+} \\ 0 \\ -\sqrt{2\gamma_2}S_{2-} \\ S_{1+} \\ S_{2-} \end{pmatrix}, \quad (6.8)$$

with

$$\mathbf{M} = \begin{pmatrix} -i\omega_1 - \gamma_1 - \gamma_{01} & i\frac{\Gamma_1}{2} & 0 & 0 & 0 \\ i\frac{\Gamma_1}{2} & -i\omega_2 - \gamma_{02} & i\frac{\Gamma_2}{2} & 0 & 0 \\ 0 & i\frac{\Gamma_2}{2} & -i\omega_3 - \gamma_{03} - \gamma_2 & 0 & 0 \\ \sqrt{2\gamma_1} & 0 & 0 & -1 & 0 \\ 0 & 0 & \sqrt{2\gamma_2} & 0 & -1 \end{pmatrix}, \quad (6.9)$$

and A_j is the Fourier transform of a_j . By solving this matrix equation, we express S_{2-} and S_{2+} in terms of S_{1-} and S_{1+} . The transfer matrix that defines this relation is \mathbf{M}_{III} . The lengthy but straightforward formula is not shown here.

The matrix describes all the process is $\mathbf{M}_{\text{sys}} = \mathbf{M}_{\text{III}} \cdot \mathbf{M}_{\text{II}} \cdot \mathbf{M}_{\text{I}}$. The reason why we do not consider any process after light enter into the output waveguide here is that in our experiment the value of γ_2 is small enough to assume all the elements after output waveguide decouple from the system and do not influence the reflection spectrum.

6.3 Experimental setup and reflection spectra

The experimental setup and our sample are shown in Fig. 6.1. Our sample is a photonic crystal membrane structure made of InGaP [19] with thickness of

180 nm. The lattice constant is $a = 485$ nm, the radius of the holes is $0.28a$. There are two waveguides shown in the sample in Fig. 6.1. One is the input waveguide with width of $1.1\sqrt{3}a$. The length of it is $219a$. The other one is the barrier waveguide, the width of it is $0.98\sqrt{3}a$. In the barrier waveguide, there are three mode-gap cavities [2]. They are created by shifting the holes around the barrier waveguide (Fig. 6.1). An output waveguide which is in line with the input waveguide is also in the structure. However, it is placed further away from the third cavity. A polarization maintaining lensed fiber (red cone in Fig. 6.1) with numerical aperture (NA) 0.55 is used to couple light from a tunable continuous wave (CW) infrared (IR) laser to the sample. A fiber circulator is used to connect the lensed fiber and laser. The third port of the fiber circulator is connected to a photodiode to measure the reflection spectra of the sample.

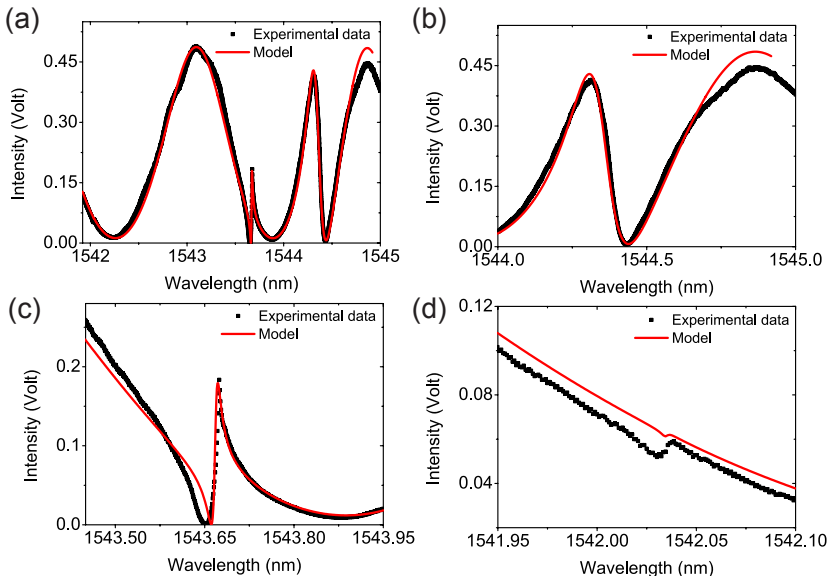


Figure 6.4: Reference reflection spectrum. The black squares represent the experimental data and the red line is the fit from our theoretical model. (b), (c) and (d) are zoomed in from (a).

The reflection spectrum is shown in Fig. 6.4. In Fig. 6.4(a), we see that the cavity resonances form different lineshapes on top of Fabry-Pérot fringes. The first Fano resonance (Fig. 6.4(b)) is between 1544 nm and 1545 nm, it is a wide and deep valley with a bit asymmetry. The second Fano resonance is between 1543.5 nm and 1544 nm, it has a sharp asymmetric line shape. The peak intensity of this resonance is twice smaller than the maximum intensity of the background fringes. The third resonance (Fig. 6.4(c)) between 1541.95 nm and 1542.10 nm is less visible.

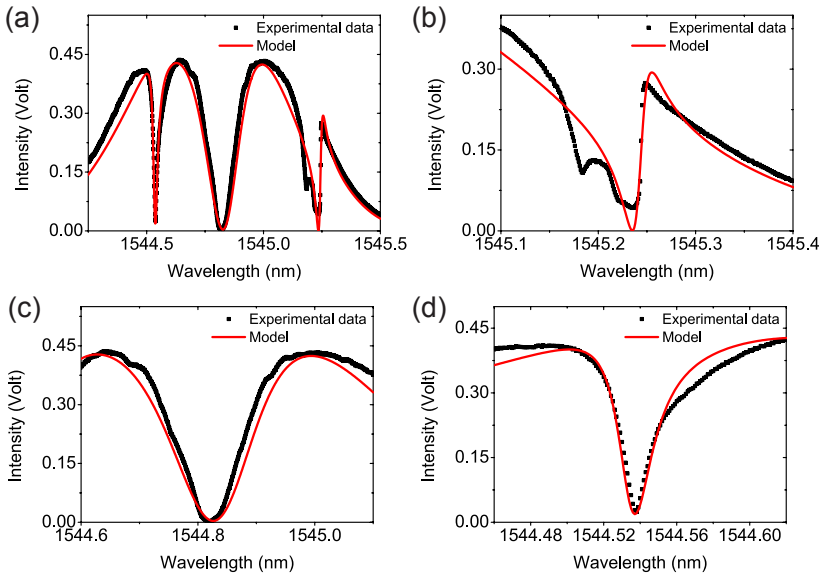


Figure 6.5: Pumped reflection spectrum. The black squares represent the experimental data and the red line is the fit from our theoretical model. (b), (c) and (d) are zoomed in from (a).

We use a CW diode laser ($\lambda_{\text{pump}} = 405 \text{ nm}$) to tune the frequencies of the cavities in the sample. The mechanism of the tuning is heating. To control the first and third cavity simultaneously, two foci are projected to the surface of the sample by an objective with NA 0.4. These foci are generated with the help of a reflective spatial light modulator (SLM) in the pump path. A digital holographic phase pattern is written on the SLM for the generation of the foci [20].

When the laser spots are focused on the cavities, the cavities resonances are tuned to the red. Although there is no direct laser light on the second cavity, the resonance of cavity 2 also shifts due to heat diffusion [21]. The reflection spectrum of the tuned device is shown in Fig. 6.5. The power of the spots on cavity 1 and cavity 3 is $9 \mu\text{W}$ and $108 \mu\text{W}$ respectively. We see in Fig. 6.5(a) the three resonances occur within 1 nm in the spectrum. One is with sharp asymmetric line shape. The other two have less asymmetric line shape and form two deep valleys in the spectrum.

6.4 Analysis of reflection spectra

The analysis of the reflection spectra is done by fitting experimental results with our model. We first fit the original spectrum, then the spectrum of the tuned device. The values of the parameters in our model are listed in Table 6.1.

The fit from our model for the original spectrum is shown in Fig. 6.4. The fit from our model agrees very well with our data for resonances 1, 2 and the

Table 6.1: Values of parameters in theoretical model

Parameter	Reference	Pumped
Γ_1/ω_0	0.00018	0.00018
Γ_2/ω_0	0.00039	0.00039
λ_1 (nm)	1543.351 ± 0.005	1544.838 ± 0.001
λ_2 (nm)	1543.638 ± 0.005	1544.993 ± 0.001
λ_3 (nm)	1542.092 ± 0.005	1544.769 ± 0.001
γ_{01}/ω_0	$(4.00 \pm 1.00) \times 10^{-6}$	4.00×10^{-6}
γ_{02}/ω_0	$(1.50 \pm 0.8) \times 10^{-6}$	1.50×10^{-6}
γ_{03}/ω_0	$> 4 \times 10^{-7}$	$(6.80 \pm 3.80) \times 10^{-6}$
γ_1/ω_0	$(5.50 \pm 0.20) \times 10^{-5}$	5.50×10^{-5}
$\omega_{\text{edge}}(2\pi c/a)$	0.301697 ± 0.000010	0.301697
$m/(1/ac)$	0.3194 ± 0.001	0.3194
r	0.15	0.15
α	0.795	0.795
Δ (nm)	0	0

^a $\omega_0 = a/\lambda_0$ and λ_0 is 1544.790 nm. $\omega_j = a/\lambda_j$ ($j = 1, 2, 3$). The values of Γ_1 and Γ_2 have been obtained from our previous work.

background fringes. It nicely characterize the period and visibility of the fringes. Meanwhile, it describes the line shapes, widths, height of the peak and depth of the trough for resonances 1 and 2. However, we can not correctly characterize the depth and width of resonance 3 at the same time. The probable cause for this is a direct coupling term between the waveguide and cavities 2 and 3, or a second neighboring coupling between the cavities. Such terms have been ignored in our model as they would lead to an excessive number of free parameters.

The fit from our model of the pumped reflection spectrum is shown in Fig. 6.5. We see that for all three resonances the fit agrees very well with experimental data. There are slight deviations on wings of the resonances between the fit and experimental data. These wings are mostly determined by the Febry-Pérot fringes. To characterize them accurately, the accurate knowledge of the curvature of the PhC waveguide band is needed. In our model, we only use two parameters m and ω_{edge} to describe the band. This is an approximation only valid for a short range. The values are obtained by fitting from the reference spectrum shown in Fig 6.4(a). Thus, the small deviation shown in the tuned spectrum which is in a different wavelength range is reasonable. It is likely that a better characterization of the waveguide band and setting the reflection of the input waveguide as a separate parameter will reduce the deviation.

The fact that the fit from our model has an excellent agreement with the experiment shows that our model describes the physical process of the system accurately. It not only explains the physical origin of the observed Fano reso-

nances, but also provides the key parameters of the sample such as the intrinsic loss rates of the cavities.

6.5 Direct manipulation of the Fano lineshape

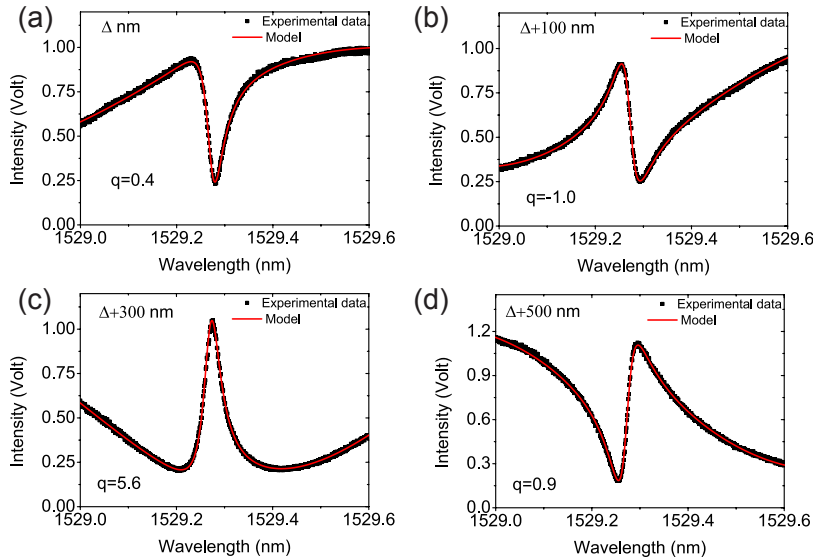


Figure 6.6: Reflection spectra of a Fano resonance at different air gaps sizes. The black squares represent experimental data and the red lines represent fits from model. (a) Δ , (b) $\Delta + 100$ nm, (c) $\Delta + 300$ nm and (d) $\Delta + 500$ nm

From our model, we know that the lensed fiber, air gap, input waveguide and the cavities together form a very special Febry-Pérot cavity. If we ignore the reflection from the facet of the input wavguide, the first “mirror” of this Febry-Pérot cavity is the tip of the lensed fiber, the second “mirror” of this cavity is the system of photonic crystal cavities. The length of the cavity is the total length of the air gap together with the input waveguide. The phase shift of a single round trip of this Febry-Pérot cavity contains two parts, the first part is the phase shift from propagation and the second part is the phase shift due the reflection from the second “mirror”. The specialty of the second “mirror” is that it is very dispersive around the cavity frequencies. The Fano lineshape is determined by the phase shift of the round trip. Therefore, we conclude that the Fano lineshape of the resonance can be tuned by changing the length of the air gap.

We performed an experiment to test this prediction on a new sample with the same parameters as our previous sample. Due to the inevitable disorder the resonance positions of the cavities appear at different wavelengths. We measured reflection spectra with different sizes of the air gap. This was done by moving the sample step by step away from the lensed fiber by our precise stage.

The measured reflection spectra are shown in Fig. 6.6. In Fig. 6.6(a), the reference spectrum is presented (the reference distance between the lensed fiber and sample is denoted by Δ , and is the distance where coupling is optimized), we see a Fano resonance is in the form of a dip with a bit asymmetry. After the reference measurement, we increase the length of air gap with step size 100 nm. The spectra with air gap size $\Delta + 100$ nm, $\Delta + 300$ nm, $\Delta + 500$ nm are shown in Fig. 6.6(b), Fig. 6.6(c) and Fig. 6.6(d) respectively. In Fig. 6.6(b), we see a sharp asymmetric Fano resonance with peak at short wavelength and dip at longer wavelength. Completely different from reference spectrum, instead of a dip we see a peak with a bit asymmetry in Fig. 6.6(c). In Fig. 6.6(d), we again see a sharp asymmetric Fano resonance, however it is almost a flipped version of Fig. 6.6(b). It has a dip at short wavelength and peak at longer wavelength. We also retrieve the q parameter that describes the asymmetry of Fano lines using Fano line formula [12]. The results shown in Fig. 6.6 confirms our prediction that the shape of Fano resonance can be tuned by changing the size of the air gap between the sample and lensed fiber.

6.6 Conclusion

In summary, Fano resonances in the reflection spectra of a direct-coupled waveguide-cavities system in a photonic crystal membrane structure have been investigated experimentally and theoretically. Our theoretical model has an excellent agreement with our experimental results and provides important information on the bare loss rate of the cavities. The origin of the Fano lineshape is the interference between the wave reflected from the lensed fiber and the wave reflected from the photonic crystal cavities. The path length difference between these waves is a round trip of the air gap size and the input waveguide. We propose and show experimentally that the Fano asymmetric parameter can be simply tuned by changing the air gap size between the sample and the fiber. Our model can be used to investigate other physical processes in the system, such as how to dynamically tune the Fano asymmetry by ultra-fast switching [22, 23].

Bibliography

- [1] J. D. Joannopoulos, S. G. Johnson, J. N. Winn, and R. D. Meade , *Photonic Crystals: Molding the Flow of Light* (Princeton University Press, Princeton, 2008). — p.69, 73.
- [2] E. Kuramochi, M. Notomi, S. Mitsugi, A. Shinya, T. Tanabe, and T. Watanabe, *Ultrahigh- Q photonic crystal nanocavities realized by the local width modulation of a line defect*, Appl. Phys. Lett. **88**, 041112 (2006). — p.69, 74.
- [3] T. Tanabe, M. Notomi, E. Kuramochi, A. Shinya, and H. Taniyama, *Trapping and delaying photons for one nanosecond in an ultrasmall high-Q photonic-crystal nanocavity*, Nature Photonics **1**, 49 (2007). — p.69.
- [4] B.-S. Song, S. Noda, T. Asano, and Y. Akahane, *Ultra-high-Q photonic double-heterostructure nanocavity*, Nat. Mater. **4**, 207 (2005). — p.69.
- [5] A. Yariv, Y. Xu, R. K. Lee, and A. Scherer, *Coupled-resonator optical waveguide: a proposal and analysis*, Opt. Lett. **24**, 711 (1999). — p.69.
- [6] M. Hafezi, S. Mittal, J. Fan, A. Migdall, and J. M. Taylor, *Imaging topological edge states in silicon photonics*, Nat. Photonics **7**, 1001 (2013). — p.69.
- [7] M. Notomi, E. Kuramochi, and T. Tanabe, *Large-scale arrays of ultrahigh-Q coupled nanocavities*, Nat. Photonics **2**, 741 (2008). — p.69.
- [8] F. Xia, L. Sekaric, and Y. Vlasov, *Ultracompact optical buffers on a silicon chip*, Nat. Photonics **1**, 65 (2007). — p.69.
- [9] M. J. Hartmann, F. G. S. L. Brandão, and M. B. Plenio, *Quantum many-body phenomena in coupled cavity arrays*, Laser Photon. Rev. **2**, 527 (2008). — p.69.
- [10] M. F. Yanik and S. Fan, *Stopping light all optically*, Phys. Rev. Lett. **92**, 083901 (2004). — p.69.
- [11] U. Fano, *Effects of configuration interaction on intensities and phase shifts*, Physical Review **124**, 1866 (1961). — p.69.
- [12] A. E. Miroshnichenko, S. Flach, and Y. S. Kivshar, *Fano resonances in nanoscale structures*, Rev. Mod. Phys. **82**, 2257 (2010). — p.69, 78.
- [13] K. Nozaki, A. Shinya, S. Matsuo, T. Sato, E. Kuramochi, and M. Notomi, *Ultralow-energy and high-contrast all-optical switch involving Fano resonance based on coupled photonic crystal nanocavities*, Opt. Express **21**, 11877 (2013). — p.69.
- [14] Y. Yu, M. Heuck, H. Hu, W. Xue, C. Peucheret, Y. Chen, L. K. Oxenløwe, K. Yvind, and J. Mørk, *Fano resonance control in a photonic crystal structure and its application to ultrafast switching*, Appl. Phys. Lett. **105**, 15 (2014). — p.69.

- [15] H. A. Haus, *Waves and Fields in Optoelectronics* (Prentice-Hall, New York, 1984). — p.72.
- [16] R. Faggiani, R. Baron, X. Zang, L. Lalouat, S. A. Schulz, K. Vynck, B. Regan, B. Cluzel, F. De Fornel, T. F. Krauss, and P. Lalanne, *Lower bound for the spatial extent of localized modes in photonic-crystal waveguides with small random imperfections*, Sci Rep. **6**, 27037 (2016). — p.72.
- [17] J. Lian, S. Sokolov, E. Yüce, S. Combrié, A. D. Rossi, and A. P. Mosk, *Dispersion of coupled mode-gap cavities*, Opt. Lett. **40**, 4488 (2015). — p.72.
- [18] H. A. Haus and W. Huang, *Coupled-mode theory*, Proc. IEEE **79**, 1505 (1991). — p.73.
- [19] S. Combrié, Q. V. Tran, A. De Rossi, C. Husko, and P. Colman, *High quality GaInP nonlinear photonic crystals with minimized nonlinear absorption*, Appl. Phys. Lett. **95**, 221108 (2009). — p.73.
- [20] M. Pasinski and B. DeMarco, *A high-accuracy algorithm for designing arbitrary holographic atom traps*, Opt. Express **16**, 2176 (2008). — p.75.
- [21] S. Sokolov, J. Lian, E. Yüce, S. Combrié, G. Lehoucq, A. De Rossi, and A. P. Mosk, *Local thermal resonance control of GaInP photonic crystal membrane cavities using ambient gas cooling*, Appl. Phys. Lett. **106**, 171113 (2015). — p.75.
- [22] E. Yüce, G. Ctistis, J. Claudon, E. Dupuy, R. D. Buijs, B. de Ronde, A. P. Mosk, J.-M. Gérard, and W. L. Vos, *All-optical switching of a microcavity repeated at terahertz rates*, Opt. Lett. **38**, 374 (2013). — p.78.
- [23] K. Nozaki, T. Tanabe, A. Shinya, S. Matsuo, T. Sato, H. Taniyama, and M. Notomi, *Sub-femtojoule all-optical switching using a photonic-crystal nanocavity*, Nat. Photonics **4**, 477 (2010). — p.78.

CHAPTER 7

Polarization conversion in photonic crystal cavities

In a system consisting of photonic crystal cavities direct coupled to waveguides, light transmission is achieved by tunneling between the waveguides and the cavity. When the coupling between the cavity and the waveguides is asymmetric, one expects extremely low transmission even on resonances. However, we experimentally observe a high transmission signal with an oscillating background. We attribute this transmission to TE (transverse electric)/TM (transverse magnetic) conversion in the cavities. We present an effective model which successfully explains the physical processes and matches our experimental data.

7.1 Introduction

Photonic crystal membrane structures are thin layers with a periodic pattern of holes [1]. This type of structures is the most widely used photonic crystal structure since it allows one to define integrated photonic circuits [2]. One of the most attractive building blocks of such device is an ultra-high Q nanocavity [3–5]. As a two-dimensional structure, the photonic membrane structure is usually designed for realizing an optimized stop gap for TE (transverse electric)-like light, the ultra-high Q cavities in such structures are resonators for TE-like modes of the light field [3–5].

Transmission measurement is a convenient way of characterizing the optical property of a nanocavity. In a direct coupled cavity and waveguides system, light transmission is achieved by tunneling between the waveguides and cavity. When the coupling between the cavity and access waveguides is asymmetric, one expects a low transmission signal even on resonances. In our experiments, we observe high transmission signal of the resonances (Fig. 7.1) although the coupling is extremely asymmetric since the nanocavities of interest are located much closer to the input waveguide than the output waveguide. Most surprisingly, this signal is TM (transverse magnetic)-like light instead of TE-like light. We attribute this high transmission to TE/TM conversion in the cavity due to unavoidable fabrication disorder [6].

In this chapter, we study the transmission spectrum of a direct coupled photonic crystal cavity and waveguides system. An analytical model based on the transfer matrix method is built to explain the origin of the TM-like resonance

signal. This model successfully explains the physical processes that lead to the observed transmission spectrum and agrees well with experimental data.

7.2 Experimental setup and transmission spectra

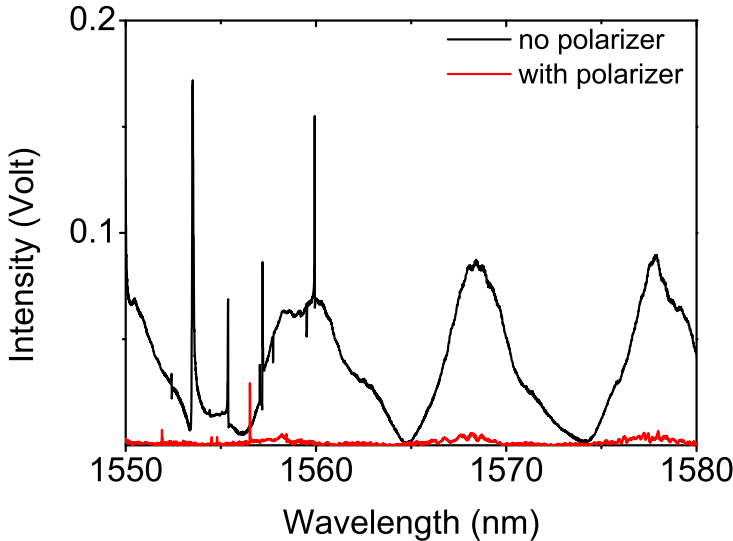


Figure 7.1: Transmission spectra of the sample. The black curve represents the spectrum measured without the polarizer, the red curve represents the spectrum measured with a polarizer selecting TE-like light at the output.

The experimental setup is very similar to the setup described in chapter 4, 5 and 6. The difference is that for one transmission spectrum a polarizer was added between the sample and photodiode at the transmission side to block the TM-like light. The sample is similar to the samples described in chapter 4, 5 and 6 with identical specifications. In this sample, there are 10 mode-gap cavities placed in the barrier waveguide.

The transmission spectra are shown in Fig. 7.1. In the spectrum measured without the polarizer, we see a few sharp peaks and dips on top of a oscillating background. The sharp peaks and dips represent the resonances in the barrier waveguide, they are expected to be from the resonances of the cavities close to the input waveguide. In the spectrum, these resonances together with a broad band background form Fano lineshapes [7, 8]. The oscillating background has a very high visibility. In the wavelength range from 1560 nm to 1580 nm, the visibility is approximately 97%. We see that the background intensity is reduced by more than 20 times when a polarizer is inserted to select only TE-like light. The dips and peaks from the cavity resonances are removed by the polarizer. From

the comparison, it is quite clear that the major contribution to the transmitted intensity is TM-like light. However, the cavity resonances only support TE-like light. This indicates there must be some processes which convert the TE-like to the TM-like light after the cavity is excited by the TE-like light.

7.3 Physical processes of the system

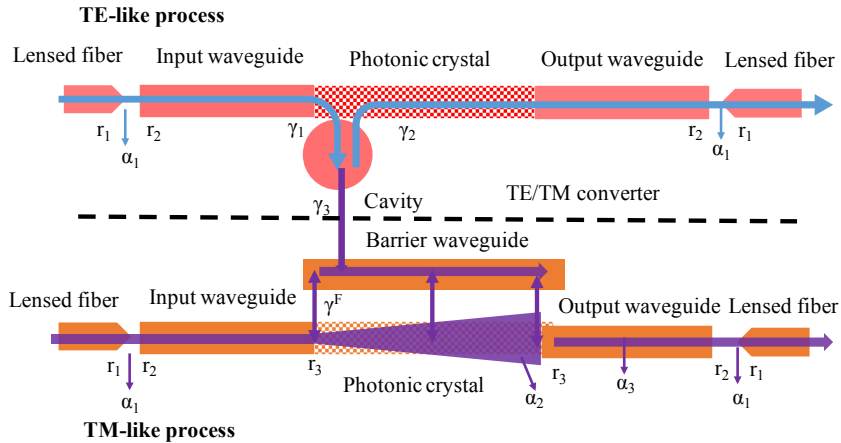


Figure 7.2: Diagram of the modeled physical process in the system. The upper part shows the process of the TE-like light and the lower part shows the TM-like process. The blue line represents the light path of the TE-like light, and the purple line represents the light path of the TM-like light.

The diagram of the physical processes we model is shown in Fig. 7.2. We first discuss the common processes for TE-like and TM-like light. These processes are the in-coupling (from lensed fiber to waveguide) and out-coupling (from waveguide to lensed fiber) processes. We assume there is no difference in these processes for TE-like and TM-like light. Similar to chapter 6, we consider here the reflections at boundaries between the lensed fiber and air gap, and between the air gap and the facet of the waveguide. Also we take into account the coupling loss. The amplitude reflection coefficients at the boundary between the lensed fiber and air gap, air gap and waveguide are r_1 and r_2 respectively. The coupling loss is modeled as a loss factor α_1 . We assume the values of these quantities are the same for TE-like and TM-like modes.

Secondly we consider free propagation in the input and output waveguides. For the input and output waveguides, both TE-like and TM-like modes can be guided. However, they are guided by different mechanisms. The TE-like light is guided by the stop gap of the periodical structure and the TM-like light as an index guided mode is guided by total internal reflection.

Finally, we discuss the transmission processes between the input and output

waveguides. There are two parts, the first is the photonic crystal part and the second is the barrier waveguide part. The photonic crystal part has a stop gap for the TE-like light but not for the TM-like light. This means that although the transport of the TE-like light is forbidden, TM-like light transport is allowed. However, the intensity of the TM-like light is expected to drop due to geometric broadening of the propagation. We use an effective loss factor α_2 to denote this power loss. Also, there will be reflections at boundaries between the photonic crystal and input (output) waveguide. Its amplitude reflection coefficient is r_3 . For the barrier waveguide, the TE-like light can only be transported through the cavity resonance. The coupling rate between the cavity and input waveguide is γ_1 , between the cavity and the output waveguide is γ_2 . For the TM-like light, light transport is still possible in the barrier waveguide. We model the barrier waveguide for TM-like light as a Fabry-Pérot cavity which is side coupled to the bulk propagation, the coupling rate is γ^F . To link the TE-like and TM-like process, we assume the resonance is coupled to the TM process after it is excited by the TE-like signal with an a priori unknown coupling rate is γ_3 .

7.4 Transfer matrices of the system

We use a transfer matrix method to model the system, the transfer matrix \mathbf{M} relates the amplitudes of forward and backward propagating TE-like and TM-like fields from left side to right side of each process. It is defined as

$$(TE_R^+, TE_R^-, TM_R^+, TM_R^-)^T = \mathbf{M} (TE_L^+, TE_L^-, TM_L^+, TM_L^-)^T. \quad (7.1)$$

Here TE and TM represent amplitudes of TE-like and TM-like light, and \pm represent forward and backward propagation. R and L represent right and left side of the sample.

We start with the in-coupling and out-coupling processes of TE-like and TM-like light. We assume there is no difference in these processes between TE-like and TM-like light. The in-coupling process is described as

$$\mathbf{M}_{cp_1} = \begin{pmatrix} \mathbf{M}_{pr_2} \cdot \mathbf{M}_{loss_1} \cdot \mathbf{M}_{Air} \cdot \mathbf{M}_{pr_1} & 0 \\ 0 & \mathbf{M}_{pr_2} \cdot \mathbf{M}_{loss_1} \cdot \mathbf{M}_{Air} \cdot \mathbf{M}_{pr_1} \end{pmatrix}. \quad (7.2)$$

The out-coupling process is described as

$$\mathbf{M}_{cp_2} = \begin{pmatrix} \mathbf{M}_{pr_1} \cdot \mathbf{M}_{loss_1} \cdot \mathbf{M}_{Air} \cdot \mathbf{M}_{pr_2} & 0 \\ 0 & \mathbf{M}_{pr_1} \cdot \mathbf{M}_{loss_1} \cdot \mathbf{M}_{Air} \cdot \mathbf{M}_{pr_2} \end{pmatrix}. \quad (7.3)$$

\mathbf{M}_{pr_1} and \mathbf{M}_{pr_2} describe the reflections at boundaries between the lensed fiber and the air, air and input waveguide (output waveguide), they have the same form as Eq. (6.2). \mathbf{M}_{Air} describes the free propagation in the air, it has the same form as Eq. (6.3). \mathbf{M}_{loss_1} describes the coupling loss, it has the same form as Eq. (6.4).

The matrices for TE and TM propagation in the input waveguide and output waveguide are,

$$\mathbf{M}_{CWG_1} = \begin{pmatrix} \mathbf{M}_{CWG_1}^{TE} & 0 \\ 0 & \mathbf{M}_{CWG_1}^{TM} \end{pmatrix}, \quad (7.4)$$

and

$$\mathbf{M}_{\text{CWG}_2} = \begin{pmatrix} \mathbf{M}_{\text{loss}_3} \cdot \mathbf{M}_{\text{CWG}_2}^{\text{TE}} & \mathbf{0} \\ \mathbf{0} & \mathbf{M}_{\text{loss}_3} \cdot \mathbf{M}_{\text{CWG}_2}^{\text{TM}} \end{pmatrix}. \quad (7.5)$$

$\mathbf{M}_{\text{CWG}_j}^{\text{TE/TM}}$ ($j = 1, 2$) has the same form as Eq.(6.6). Here, $j = 1$ denotes input waveguide and $j = 2$ denotes the output waveguide. The wave vector of TE light k^{TE} is expressed as $k^{\text{TE}} = \pi/a - \sqrt{2m(\omega - \omega_{\text{edge}})}$. We neglect the dispersion of TM light and express its wave vector as $k_{\omega}^{\text{TM}} = n_{\text{eff}_1}\omega/c$. Here n_{eff_1} is the effective index we assign to the TM-like light in the waveguide. The value of it is in Table 7.3 in the appendix. We include a loss matrix $\mathbf{M}_{\text{loss}_3}$ to take into account the propagation loss in the output wavguide, since the length of the output waveguide is 0.95 mm. Loss in the short input waveguide is neglected.

Now we construct the matrices related to the barrier waveguide. We first discuss the TM-like process. For TM light we model the barrier waveguide as a side-coupled Fabry-Pérot cavity and treat it as a scattering problem. The transfer matrix of it is [9, 10]

$$\mathbf{M}_{\text{scc}} = \begin{pmatrix} 1 - \frac{2\gamma_l}{i(\omega - \omega_l) + \gamma_{0l}} & -\frac{2\gamma_l}{i(\omega - \omega_l) + \gamma_{0l}} \\ \frac{2\gamma_l}{i(\omega - \omega_l) + \gamma_{0l}} & 1 + \frac{2\gamma_l}{i(\omega - \omega_l) + \gamma_{0l}} \end{pmatrix}. \quad (7.6)$$

Here ω_l is the frequency of the resonance l of the side coupled cavity, γ_{0l} is the intrinsic loss rate of the resonance l , γ_l is the coupling rate between the resonance l and the side coupled waveguide. Since for TM-like light the waveguide is open, the cavity we refer here is a Fabry-Pérot cavity originated from a waveguide. Thus, it supports many longitudinal modes. In a good approximation, Eq. (7.6) is modified to

$$\mathbf{M}_{\text{scc}} = \begin{pmatrix} 1 - \sum_l \frac{2\gamma_l^F}{i(\omega - \omega_l^F) + \gamma_{0l}^F} & -\sum_l \frac{2\gamma_l^F}{i(\omega - \omega_l^F) + \gamma_{0l}^F} \\ \sum_l \frac{2\gamma_l^F}{i(\omega - \omega_l^F) + \gamma_{0l}^F} & 1 + \sum_l \frac{2\gamma_l^F}{i(\omega - \omega_l^F) + \gamma_{0l}^F} \end{pmatrix}. \quad (7.7)$$

For the TE-like light process, we model our sample as a direct coupled waveguides and cavity system. Using the coupled equations discussed in chapter 2, we derive the transfer matrix of the direct coupled waveguides and cavity system as

$$\mathbf{M}_{\text{dcwc}} = \begin{pmatrix} \frac{i(\omega_0 - \omega) - \gamma_0 + \gamma_1 + \gamma_2}{2\sqrt{\gamma_1\gamma_2}} & \frac{i(\omega_0 - \omega) - \gamma_0 - \gamma_1 + \gamma_2}{2\sqrt{\gamma_1\gamma_2}} \\ \frac{-i(\omega_0 - \omega) + \gamma_0 - \gamma_1 + \gamma_2}{2\sqrt{\gamma_1\gamma_2}} & \frac{-i(\omega_0 - \omega) + \gamma_0 + \gamma_1 + \gamma_2}{2\sqrt{\gamma_1\gamma_2}} \end{pmatrix}. \quad (7.8)$$

Here γ_1 and γ_2 are the coupling rates between the cavity and the input waveguide and output waveguide, ω_0 is frequency of the cavity resonance and γ_0 is the intrinsic loss rate of the cavity.

To link the TE-like and TM-like process we assume the cavity resonance is coupled to three channels. The first and second channels are TE-like channels, they are the input and output waveguides. The third channel is a TM-like channel, it is the barrier waveguide. The coupling rate between the resonance and

TM channel is γ_3 . To derive the conversion matrix which describes this, we start with a set of coupled equation as following,

$$i\omega A = i\omega_0 A - (\gamma_0 + \gamma_1 + \gamma_2 + 2\gamma_3)A + S_{\text{total}} \quad (7.9a)$$

$$TE_L^- = -TE_L^+ + \sqrt{2\gamma_1}A \quad (7.9b)$$

$$TE_R^- = -TE_R^+ + \sqrt{2\gamma_2}A \quad (7.9c)$$

$$TM_L^+ = TM_R^+ + \sqrt{2\gamma_3}A \quad (7.9d)$$

$$TM_L^- = TM_R^- - \sqrt{2\gamma_3}A \quad (7.9e)$$

Here $S_{\text{total}} = \sqrt{2\gamma_1}TE_L^+ + \sqrt{2\gamma_2}TE_R^- + \sqrt{2\gamma_3}TM_L^+ + \sqrt{2\gamma_3}TM_R^-$.

From Eqs.(7.9), we can derive the matrix links $(TE_R^+, TE_R^-, TM_R^+, TM_R^-)^T$ and $(TE_L^+, TE_L^-, TM_L^+, TM_L^-)^T$, it is

$$\mathbf{M}_{\text{cv}} = \begin{pmatrix} \frac{i(\omega_0-\omega)-\gamma_0+\gamma_1+\gamma_2}{2\sqrt{\gamma_1\gamma_2}} & \frac{i(\omega_0-\omega)-\gamma_0-\gamma_1+\gamma_2}{2\sqrt{\gamma_1\gamma_2}} & \sqrt{\frac{\gamma_3}{\gamma_2}} & \sqrt{\frac{\gamma_3}{\gamma_2}} \\ \frac{-i(\omega_0-\omega)+\gamma_0-\gamma_1+\gamma_2}{2\sqrt{\gamma_1\gamma_2}} & \frac{-i(\omega_0-\omega)+\gamma_0+\gamma_1+\gamma_2}{2\sqrt{\gamma_1\gamma_2}} & -\sqrt{\frac{\gamma_3}{\gamma_2}} & -\sqrt{\frac{\gamma_3}{\gamma_2}} \\ -\sqrt{\frac{\gamma_3}{\gamma_1}} & -\sqrt{\frac{\gamma_3}{\gamma_1}} & 1 & 0 \\ \sqrt{\frac{\gamma_3}{\gamma_2}} & \sqrt{\frac{\gamma_3}{\gamma_2}} & 0 & 1 \end{pmatrix}. \quad (7.10)$$

In Eq.(7.10), we see that \mathbf{M}_{cv} has a very elegant format, since when γ_3 is zero, it degrades to a diagonal block matrix in which TE-like and TM-like process are well separated. Combining \mathbf{M}_{cv} with the previously derived matrices, we build the matrix which describes the barrier waveguide, input waveguide and output waveguide,

$$\mathbf{M}_{\text{BWG}} = \begin{pmatrix} 1 & 0 \\ 0 & \mathbf{M}_{\text{pr}_3} \cdot \mathbf{M}_{\text{loss}_2} \cdot \mathbf{M}_{\text{BWG}}^{\text{TM}} \end{pmatrix} \cdot \begin{pmatrix} 1 & 0 \\ 0 & \mathbf{M}_{\text{scc}} \end{pmatrix} \cdot \mathbf{M}_{\text{cv}} \cdot \begin{pmatrix} 1 & 0 \\ 0 & \mathbf{M}_{\text{BWG}}^{\text{TM}} \cdot \mathbf{M}_{\text{pr}_3} \end{pmatrix}. \quad (7.11)$$

In Eq. (7.11), we have three new matrices $\mathbf{M}_{\text{loss}_2}$, \mathbf{M}_{pr_3} and $\mathbf{M}_{\text{BWG}}^{\text{TM}}$. \mathbf{M}_{pr_3} describes the reflection at boundaries between the waveguide and bulk crystal. $\mathbf{M}_{\text{loss}_2}$ describes the geometric broadening loss in the bulk crystal for TM-like light. We estimate the effective power loss is $1 - \frac{W}{2\pi D}$, W here is the width of the output waveguide and D is the distance between input and output waveguide, i.e. we assume the light spreads uniformly in all angles. The estimated value of the power loss factor α_2 that models this process is in the appendix. The matrix $\mathbf{M}_{\text{BWG}}^{\text{TM}}$ describes the free propagation of the TM-like light in the bulk crystal,

$$\mathbf{M}_{\text{BWG}}^{\text{TM}} = \begin{pmatrix} e^{(ik_{\omega}^{\text{TM}_2}D/2)} & 0 \\ 0 & e^{(-ik_{\omega}^{\text{TM}_2}D/2)} \end{pmatrix}. \quad (7.12)$$

Here $k_{\omega}^{\text{TM}_2}$ is the wave vector of the TM light in the crystal which we approximate as $k_{\omega}^{\text{TM}_2} = n_{\text{eff}_2}\omega/c$. Here n_{eff_2} is the effective index of the TM-like light in the

bulk crystal, the procedure to estimate this parameter is given in the appendix. For simplicity, we assume the conversion happens in the center of the barrier waveguide, the results are not strongly dependent on this assumption.

Having found the matrices of all processes, we write the transfer matrix of the whole system as

$$\mathbf{M}_{\text{sys}} = \mathbf{M}_{\text{cp}_2} \cdot \mathbf{M}_{\text{CWG}_2} \cdot \mathbf{M}_{\text{BWG}} \cdot \mathbf{M}_{\text{CWG}_1} \cdot \mathbf{M}_{\text{cp}_1}. \quad (7.13)$$

7.5 Analysis of experimental data

For the analysis of the experimental data, we focus on the observed resonance between 1553 nm and 1554 nm. Before we analyze the transmission data, we first use the reflection model we have developed in chapter 6 to analyze the reflection spectrum. The benefit of this is that we reduce the number of free parameters in the transmission model. The experimental result and the fit of the reflection spectrum are shown in Fig. 7.3. In Fig. 7.3, we see an asymmetric reflection dip in the spectrum and the fit agrees well with the experimental data.

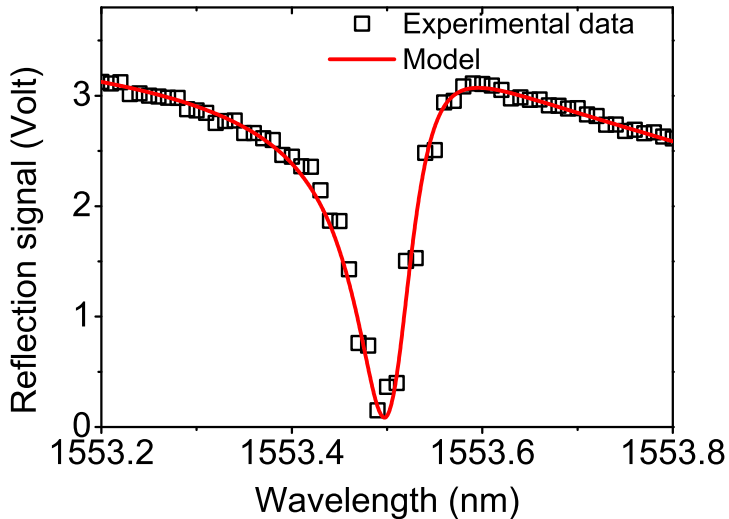


Figure 7.3: Reflection spectrum. Black squares: experimental data. Red line: fit from model.

We list the main parameters related to the resonance in Table 7.1, the other retrieved parameters are in Table 7.2 in the appendix. We have to point out the loss rate we retrieve from the reflection spectrum is the sum of the pure intrinsic loss and the TE/TM conversion.

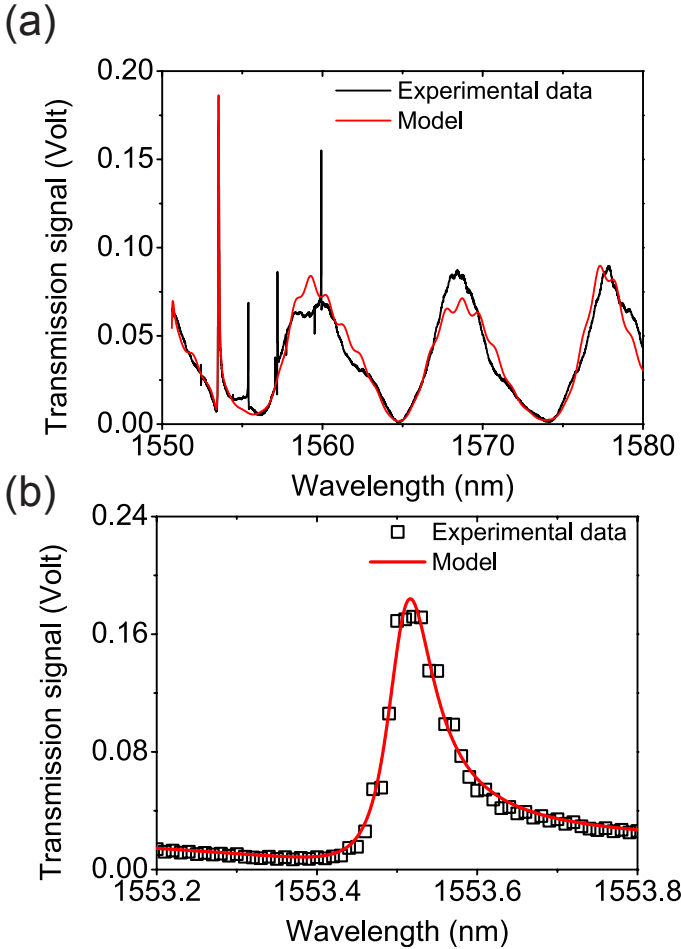


Figure 7.4: Transmission spectrum. (b) is zoomed in from (a).

We use the transmission model to analyze our data, taking into account that 2% of the input signal is TM-like light, as determined in a calibration measurement. We list the parameters direct related to resonance in Table 7.1. The other parameters are in the Appendix. The fit of the transmission spectrum is shown in Fig. 7.4. From Fig. 7.4, we see the fit curve agrees very well with our experiential data, it not only accurately reproduces the resonance but also catches the feature of the oscillating fringes. This shows our model well explains the physical processes of the light transport in our system.

It is noticeable that from Table 7.1 that 10 % of the loss term is due to TE/TM conversion. This shows that TE/TM scattering is an important loss channel of the resonance, while the main loss is attributed to out-of-plane scattering.

We point out that the ratio between the reflected intensity and transmitted

Table 7.1: Values of parameters of the resonance

Parameter	R model (no conversion)	T model (with conversion)
λ_1 (nm)	1553.506 ± 0.001	1553.506
γ_1/ω_0	$(22.17 \pm 1.12) \times 10^{-6}$	22.17×10^{-6}
$(\gamma_0 + \gamma_3)/\omega_0$	$(4.63 \pm 0.73) \times 10^{-6}$	$(4.74 \pm 0.31) \times 10^{-6}$
γ_3/ω_0	—	$(0.42 \pm 0.04) \times 10^{-6}$

^a $\omega_0 = a/\lambda$ and λ is 1543.506 nm, The error-bars in the table are 95% confidence interval from fitting.

intensity in the model is 2-3 orders smaller than in our experiment. It is plausible that the value of the geometric broadening loss we estimate for the TM-like light is too high. However, this loss in our model happens after the conversion (Eq. (7.11)). Changing the estimated value in the model does not lead to noticeable effects on the ratio between the resonance peak and the oscillating fringes.

In the model, we simplified the TM-like light propagation in the barrier waveguide as a side-coupled waveguide and cavity system. The high visibility but low finesse is successfully explained by this model. However, the spacing of the resonances does not match the expected group index of the TM-like light in the barrier waveguide. The expected group index that corresponds to the observed fringe spacing is around 2.60, whereas the group index we obtain using plane-wave-expansion (PWE) method [11, 12] is 1.23. More detailed modeling of the TM-like light propagation could shed light on this. Experiments such as NSOM [13], OLCR [14] or ab-initio numerical simulation [15, 16] are suggested to be carried out in the future to confirm the interference process giving rise to the large-scale fringes.

7.6 Conclusion

We have shown here that the transmission signals measured from our direct coupled waveguide-cavities system are due to the TM-like light not the TE-like light. The background fringes are attributed to TM-like light we send in. The TM resonance signal from the cavity is from TE/TM conversion in the cavities. We have developed an analytical model to explain the physical processes, it agrees well with our experimental data. Combined with our experimental data and model, we conclude that TE/TM conversion is a substantial loss channel for cavity resonances.

7.7 Appendix

Here, we provide details of our fitting procedure and list the value of parameters. We first use the reflection model discussed in chapter 6 to obtain the parameters

of TE-like light. They are listed in Table 7.2.

Table 7.2: Parameters of TE-like light from reflection model

Parameter	Value
$\omega_{\text{edge}} (2\pi c/a)$	0.29828 ± 0.00006
$m (1/ac)$	0.3246 ± 0.0014
r_1	0.217 ± 0.012
r_2	0.107 ± 0.006
α_1	0.64 ± 0.01
$\Delta(a)$	6

The errorbars in the table are 95% confidence interval from fitting. The value of Δ is from our estimation.

For the TM-like light, the value of the effective index n_{eff_1} in the access waveguides is obtained in two steps. First, we obtain the estimated value $n_{\text{est}} = 1.24$ for n_{eff_1} from the dispersion calculated from the plane-wave-expansion (PWE) method. Second, in order to match the Fano lineshape of the resonance, we do a constrained fit for n_{eff_1} with the initial value obtained from PWE method. The effective index n_{eff_2} in the bulk is estimated simply by calculating the averaged index. The reflectance at boundaries between the waveguide and bulk crystal is estimated from Fresnel law using n_{eff_1} and n_{eff_2} . The geometric broadening loss is estimated using $1 - \frac{W}{2\pi D}$, where W is the width of the output waveguide, D is the distance between the input and output waveguides. The propagation loss in the long output waveguide is assumed to be 50%.

Table 7.3: Parameters of TM-like light of propagation and reflection

Parameter	Value
n_{eff_1}	$1.2342 \pm 0.0002^*$
n_{eff_2}	2.63
r_3	0.36
α_2	0.997
α_3	0.5

The errorbars in the table are 95% confidence interval from fitting. The value of n_{eff_1} is a constrained free parameter in fitting to match the Fano line shape of the resonance, its initial value is obtained from PWE method.

After obtaining all the parameters in table 7.3, we do fitting to the barrier waveguide which we treat as a side coupled Fabry-Pérot cavity. We assume there

are 5 relevant longitudinal modes. The parameters are below. Compared to the parameters related to mode 2, 3 and 4, the parameters related to mode 1 and 5 are quite off. This is because the initial values of mode 1 and 5 are set outside the range from 1550.60 nm to 1580.30 nm.

Table 7.4: Parameters of the side coupled Fabry-Pérot cavity

Parameter	Value
λ_1^F (nm)	1550.05 ± 0.05
λ_2^F (nm)	1556.04 ± 0.04
λ_3^F (nm)	1564.75 ± 0.01
λ_4^F (nm)	1574.01 ± 0.02
λ_5^F (nm)	1583.43 ± 0.02
γ_1^F/ω_0	$(8.3 \pm 2.3) \times 10^{-5}$
γ_2^F/ω_0	0.00122 ± 0.00004
γ_3^F/ω_0	0.00215 ± 0.00005
γ_4^F/ω_0	0.00175 ± 0.00004
γ_5^F/ω_0	0.00574 ± 0.00010
γ_{01}^F/ω_0	$(1.2 \pm 0.8) \times 10^{-5}$
γ_{02}^F/ω_0	0.000605 ± 0.000023
γ_{03}^F/ω_0	0.000231 ± 0.000006
γ_{04}^F/ω_0	0.000421 ± 0.000012
γ_{05}^F/ω_0	$1 \times 10^{-9} \pm 4 \times 10^{-5}$

^a $\omega_0 = a/\lambda$ and λ is 1543.506 nm. The error-bars in the table are 95% confidence interval from fitting.

Bibliography

- [1] J. D. Joannopoulos, S. G. Johnson, J. N. Winn, and R. D. Meade , *Photonic Crystals: Molding the Flow of Light* (Princeton University Press, Princeton, 2008). — p.81.
- [2] S. McNab, N. Moll, and Y. Vlasov, *Ultra-low loss photonic integrated circuit with membrane-type photonic crystal waveguides*, Opt. Express **11**, 2927 (2003). — p.81.
- [3] B.-S. Song, S. Noda, T. Asano, and Y. Akahane, *Ultra-high-Q photonic double-heterostructure nanocavity*, Nat. Mater. **4**, 207 (2005). — p.81.
- [4] Y. Akahane, T. Asano, and B.-S. Song, *High- Q photonic nanocavity in a two-dimensional photonic crystal*, Nature **425**, 944 (2003). — p.81.
- [5] E. Kuramochi, M. Notomi, S. Mitsugi, A. Shinya, T. Tanabe, and T. Watanabe, *Ultrahigh- Q photonic crystal nanocavities realized by the local width modulation of a line defect*, Appl. Phys. Lett. **88**, 041112 (2006). — p.81.
- [6] A. F. Koenderink, A. Lagendijk, and W. L. Vos, *Optical extinction due to intrinsic structural variations of photonic crystals*, Phys. Rev. B **72**, 153102 (2005). — p.81.
- [7] U. Fano, *Effects of configuration interaction on intensities and phase shifts*, Physical Review **124**, 1866 (1961). — p.82.
- [8] A. E. Miroshnichenko, S. Flach, and Y. S. Kivshar, *Fano resonances in nanoscale structures*, Rev. Mod. Phys. **82**, 2257 (2010). — p.82.
- [9] S. Fan, *Sharp asymmetric line shapes in side-coupled waveguide-cavity systems*, Appl. Phys. Lett **80**, 908 (2002). — p.85.
- [10] H. A. Haus, *Waves and Fields in Optoelectronics* (Prentice-Hall, New York, 1984). — p.85.
- [11] P. T. Leung, S. Y. Liu, S. S. Tong, and K. Young, *Time-independent perturbation theory for quasinormal modes in leaky optical cavities*, Phys. Rev. A **49**, 3068 (1994). — p.89.
- [12] S. G. Johnson and J. D. Joannopoulos, *Block-iterative frequency-domain methods for Maxwell's equations in a planewave basis*, Opt. Express **8**, 173 (2001). — p.89.
- [13] S. R. Huisman, G. Ctistis, S. Stobbe, A. P. Mosk, J. L. Herek, A. Lagendijk, P. Lodahl, W. L. Vos, and P. W. H. Pinkse, *Measurement of a band-edge tail in the density of states of a photonic-crystal waveguide*, Phys. Rev. B **86**, 155154 (2012). — p.89.
- [14] A. Parini, P. Hamel, A. De Rossi, S. Combrié, N. V. Q. Tran, Y. Gottesman, R. Gabet, A. Talneau, Y. Jaouën, and G. Vadalà, *Time-wavelength reflectance maps of photonic crystal waveguides: A new view on disorder*

- induced scattering*, J. Lightwave Technol. **26**, 3794 (2008). — p.89.
- [15] A. F. Oskooi, D. Roundy, M. Ibanescu, P. Bermel, J. Joannopoulos, and S. G. Johnson, *Meep: A flexible free-software package for electromagnetic simulations by the FDTD method* , Comput. Phys. Commun. **181**, 687 (2010). — p.89.
- [16] A. Taflove and S. C. Hagness, *Computational Electrodynamics: The Finite-Difference Time-Domain Method, Third Edition* (Artech House, Boston, 2005). — p.89.

CHAPTER 8

Experimental demonstration of strong control of the Q factor of a disorder-induced resonance

8.1 Introduction

Ultrahigh Q nanocavities [1–4] provide opportunity to trap photons in a nanoscale space for nanoseconds [5, 6]. This superior function of ultrahigh Q nanocavities gives rise to possibilities for quantum information and optical processing [7–9]. Photonic crystal membrane cavities attract much attention because of their high Q and small volumes, and because they can be integrated with other functional components such as photonic crystal waveguides [10–12] on chips.

The origin of the resonances of photonic crystal cavities are defect modes in the stop gaps or band gap [10]. The mode-gap cavity (Fig 1.2) [4] is created by locally modulating the hole positions of a photonic crystal waveguide. Its resonance exists in the mode-gap between the waveguide band and photonic crystal band. Fascinating devices such as optical delay lines and memories have been demonstrated in structures composed of mode-gap cavities [13, 14].

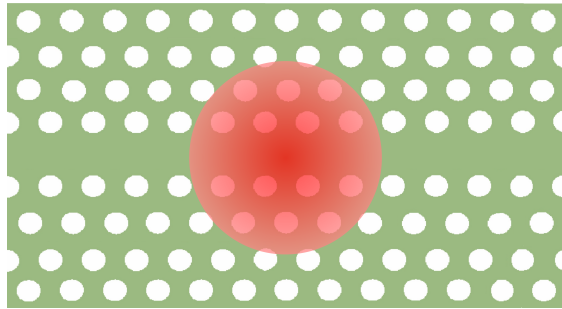


Figure 8.1: Schematic representation of a photonic crystal waveguide with local index modulation. The red disk indicates the part that the index is locally modulated.

Instead of introducing local modulation of the holes positions around a waveguide, it has been proposed that a mode-gap cavity can be created by introducing a tapered positive local refractive index change on a waveguide (Fig. 8.1) [15]. This local index change could be introduced using nonlinear effects such as the Kerr effect [16] or thermal effects [17]. The principle is in fact the same as

the previous design of a mode-gap cavity, since both of the designs create defect modes in the mode-gap by changing the local effective width of a waveguide. Compared to the previous design, the latter one offers a reconfigurable way to create cavities on a waveguide.

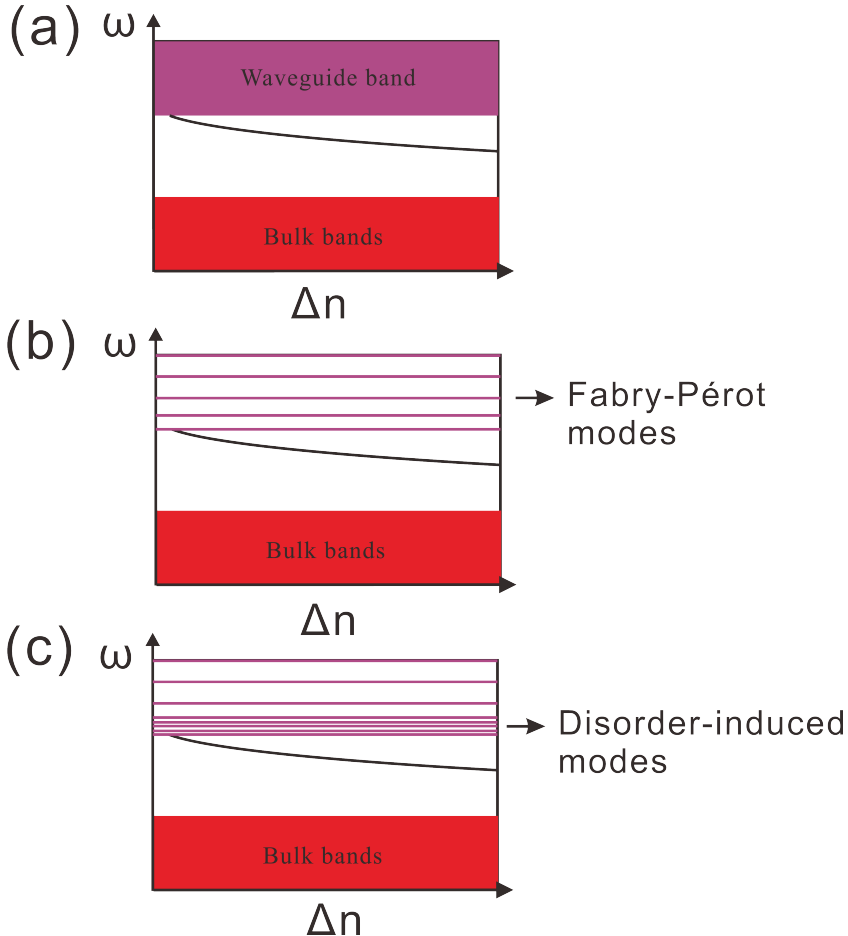


Figure 8.2: Three origins of the resonance of a mode-gap cavity. (a) In an infinite structure, the resonance emerges from a continuous band. (b) In a finite waveguide without disorder, a resonance emerges from one of the Fabry-Pérot modes. (c) In a finite waveguide with disorder, the resonance emerges from a disorder-induced resonance.

To create a resonance using nonlinear effects is also very attractive from the view point of physics. The defect modes originate from continuum [10]. One can imagine when a defect such as a local change of hole sizes is gradually switched on, a defect mode emerges from the continuum into the stop gap gradually. The same will happen if an appropriate local index change is introduced (Fig. 8.2(a)). As the amplitude of the local index change increases, the defect gets pushed deeper

into the stop gap. As a consequence, the mode gets more confined around the part where the local index change is maximal, the mode volume decreases and the Q increases (for a finite size structure). An experiment to verify this process permits a direct observation of the evolution of a mode from the continuum to a localized state, and vice versa.

The situation in a real finite size system is even more interesting. For a finite size waveguide, the waveguide band splits into a set of Fabry-Pérot modes [11]. Thus, one expects that the defect mode originates from the Fabry-Pérot modes (Fig. 8.2(b)). But this is not true due to unavoidable disorder [18]. Close to the band edge there are disordered-induced localized modes [19–23] instead of the Fabry-Pérot modes. Thus, one expects that the localized mode which is created should originate from one of the disorder-induced modes. As the amplitude of the local index change increases, a loosely confined disorder-induced mode should gradually be confined to the position where the local index change happens (Fig. 8.2(c)), and the Q of this mode should increase with the strength of the index change.

We perform an experiment with the goal of converting a disorder-induced mode into a localized cavity resonance. Using thermal tuning, we observe one order of magnitude increase of the Q of a disorder-induced resonance. Unlike typical disorder-induced modes which are completely localized in the waveguide, the mode we show here is only partially localized in the waveguide. Surprisingly, as we increase the amplitude of the local index change we observe that the confinement of this mode in the direction transverse to the waveguide is increased.

8.2 Sample and Experimental setup

The schematic representation of the experimental setup and sample are shown in Fig. 8.3. The sample is a GaInP membrane structure [24] with a triangle lattice air hole pattern on it. The thickness h of the membrane is 180 nm. The lattice constant a is 485 nm. The radius of the holes is $0.28a$. There are three line defects which represent three waveguides. The two waveguides which are in line are the carrier waveguides, and their width is $W_1 = 1.1\sqrt{3}a$. The other one is the barrier waveguide, its width is $W_0 = 0.98\sqrt{3}a$ and its length L is $106a$. A tunable continuous wave (CW) infrared (IR) laser is used to provide signal for characterizing our sample. A fiber circulator is used to connect the lensed fiber and CW IR laser. The third port of the fiber circulator is connected to a photodiode to measure the reflection spectra of the sample. Two laser spots are focused on the surface of our sample by an objective with numerical aperture (NA) of 0.4 to introduce local index changes. One is from a CW diode laser with wavelength of 405 nm with the full width of maximum (FWHM) $0.83 \mu\text{m}$, the other one is from a CW diode laser of 640 nm with the FWHM of $0.94 \mu\text{m}$. We name the laser spot from the 640 nm laser "pump", and the laser spot from 405 nm laser "tickle". This is because during the experiment the pump power is more than $100 \mu\text{W}$, and it is focused at a fixed position at $x = 7.0 \mu\text{m}$. Its main role is to introduce a big local modulation of the refractive index so that

a localized resonance may be created. The power of the tickle beam is set to be $15 \mu\text{W}$ and it is used to identify the profile of the mode using the line scan technique we have discussed in chapter 4. The scanning traces of the tickle beam are shown in Fig. 8.3(b). With the help of the tickle beam, we not only obtain the spatial information of the mode, but also detect how the spatial profile changes due to the pump. Thanks to the large difference in wavelength, no interference effects between pump and tickle beams occur. During the experiment the sample is kept in a He environment with oxygen concentration less than 0.03% in order to suppress oxidation effects [25, 26]. More importantly, compared to N_2 which we used before, He reduces the spatial width of the index change [17].

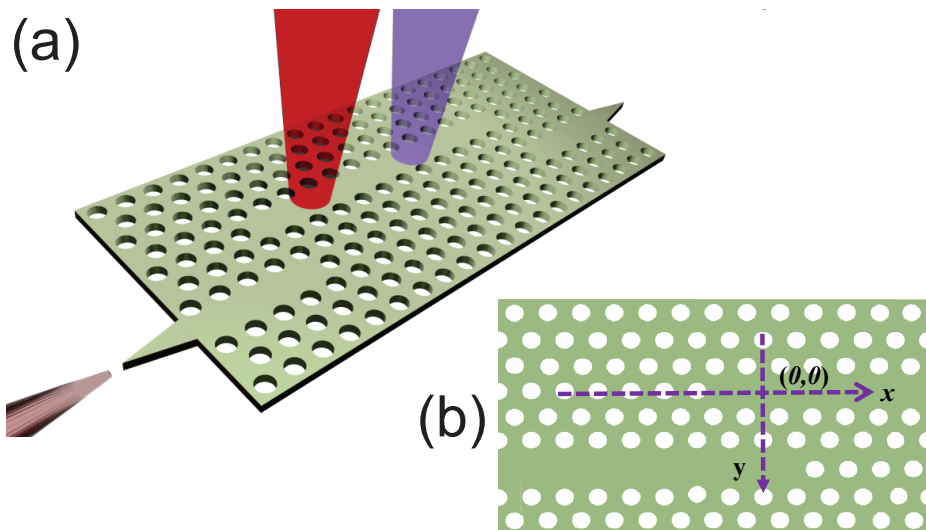


Figure 8.3: (a) Schematic representation of the sample and experimental setup. The green membrane represents the sample. The cone left of the membrane represents a polarization maintaining lensed fiber (PMF). The purple cone represents a focused beam with wavelength of 405 nm. The red cone represents another focused beam of wavelength 640 nm. (b) Scanning traces of the 405 nm laser spot on our sample. One trace is the x scan, the other trace is the y scan.

8.3 Experimental results

We perform reflection measurements with different pump powers, the spectra are shown in Fig. 8.4. All the spectra shown in Fig. 8.4 are obtained with the tickle beam switched off. We see a common oscillating background in the spectra. As shown in chapter 6, this background is from the Fabry-Pérot cavity formed by the lensed fiber together with the input waveguide. We see as we increase the pump power step by step from 0.343 mW to 1.513 mW, one resonance shifts from the wavelength around 1534 nm to 1540 nm. As the resonance shifts to longer wavelength, it shows different Fano lineshapes. Although the Fano lineshape

complicates the interpretation of linewidth of the resonance, it is quite clear that there is a significant narrowing of the linewidth. When tracing back this resonance to the spectrum measured at 0 mW pump power, this resonance is expected to occur between 1532 nm and 1533 nm. In the spectrum of 0 mW pump power, we do see a Fano peak between 1532 nm and 1533 nm. Noticeably, there is a small dent on top of this peak. This indicates that this resonance coincides with another resonance that probably occurs deeper in the waveguide.

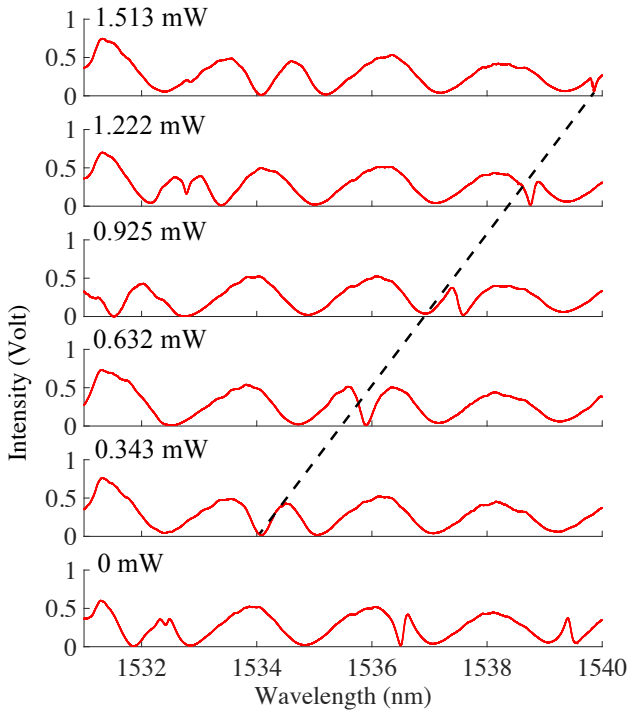


Figure 8.4: Reflection spectra at different pump levels. The dashed line here is a guide to the eye.

Using the reflection model from chapter 6, we extract the wavelength and the Q of the resonance at different pump powers. The Q is calculated by $Q = \frac{\omega_0}{2(\gamma_0 + \gamma_1)}$, where ω_0 is the resonance frequency, γ_0 is the intrinsic loss rate of the cavity and γ_1 is the coupling rate between the cavity and waveguide. The results are shown in Fig. 8.5. We see that the wavelength of the resonance increases almost linearly with pump power. We see a huge increase of the Q factor in Fig. 8.5. The Q experiences an increase from 2400 to 24000, and at higher powers appears to increase exponentially with pump power.

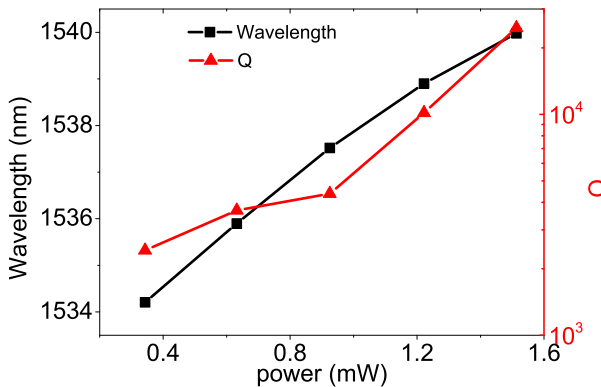


Figure 8.5: Q and wavelength of the resonance versus pump power. Black square: wavelength of the resonance. Red triangle: Q factor of the resonance note the logarithmic scale. The lines in the graph connect data points.

In Fig. 8.5, it is noticeable that the wavelength shift of the resonance increases a bit slower than linear at the highest pump power. This is opposite to our expectation. Since we expect that the mode should get more confined around the pump beam, this should lead to even an acceleration of the wavelength shift. The increase of the Q indicates that the coupling rate to the input waveguide decreases with pump power, and this supports our expectation that the mode profile should become more confined. The reason that the wavelength shift slows down with the pump power is not completely clear for us yet. In the experiment, we observe a blue shift of > 250 pm of the resonance after the pump measurement. The blue shift is very likely due to removal of the water layer from the sample surface and possibly oxidation effects [25–27]. The blue shift may be one of the contributions to the slow down of the wavelength shift. In our data analysis, although we take into account the effect of the blue shift, we can not compensate it perfectly since the resonance we analyze coincides with another resonance (Fig. 8.4).

In order to obtain the spatial information of the mode, we perform the x scan of the tickle beam along the waveguide direction at pump power 1.513 mW and 0.925 mW. The results are shown in Fig. 8.6. We also plot the temperature distribution caused by the pump beam in Fig. 8.6. It is calculated using the finite element method (COMSOL) as in Ref. 17. The wavelength shift in Fig. 8.6 is defined as $\Delta\lambda = \lambda(x) - \lambda_{\max}$, here λ_{\max} is the maximum of the wavelength of the resonance measured during the tickle beam scan. In Fig. 8.6, we see that the wavelength shift of the resonance has two maxima during the tickle scan indicating that the mode has two intensity maxima. Remarkably, one maximum is around the end facet of the input waveguide. This indicates that this mode is extended beyond the barrier waveguide and into the photonic crystal part. We also see the amplitudes of wavelength shift we obtain from two pump power levels

are the same.

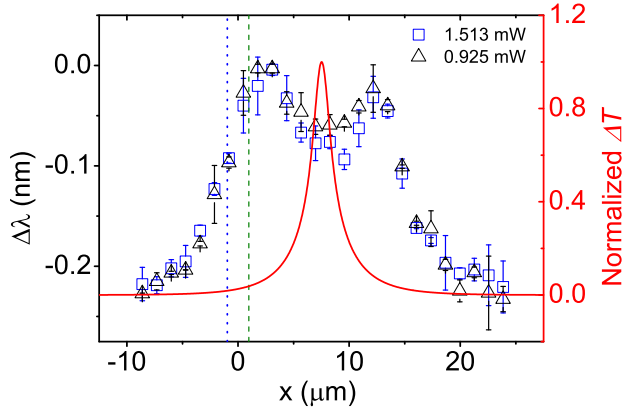


Figure 8.6: Resonance wavelength shift versus tickle beam x position at different pump power levels. Blue square: pump power is 1.513 mW. Black triangle: pumper power 0.925 mW. The error bars represent the standard deviation of two measurements. The red line is the temperature profile induced by the pump along the x direction. The blue dotted line represents the position of the facet of the barrier waveguide. The green dashed line represents the position of the end facet of the input waveguide.

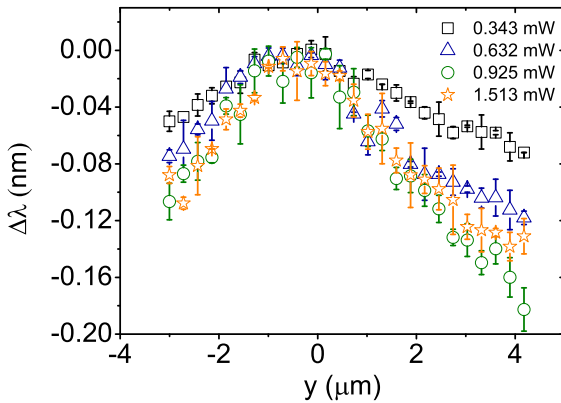


Figure 8.7: Wavelength shift of the resonance versus tickle beam position in the y line scan for four different pump powers.

We show the wavelength shift of the resonance versus vertical tickle beam position in the y line scan in Fig. 8.7. The wavelength shift in Fig. 8.7 is defined as $\Delta\lambda = \lambda(y) - \lambda_{\max}$, here λ_{\max} is the maximum of the wavelength of the

resonance measured during the tickle beam scan. The profile is centered around $y = -0.7 \mu\text{m}$ at all power levels. Its width decreases with power, although the highest two pump powers show a very similar width. This is another signature that the mode volume decreases with pump power.

8.4 Conclusion

In conclusion, we observe that the Q of a disorder-induced resonance increases 10 times when we use a pump beam to introduce a local refractive index change in a photonic crystal waveguide. From the x line scan data, we see that this mode is not completely longitudinally confined in the photonic crystal waveguide but extends in the bulk photonic crystal. We observe that the confinement of this mode in the transversal direction of the waveguide is increased as we increase the pump power.

The increase of the Q and the confinement in transversal direction of the mode show that mode profile of the resonance is decreased. However, we can not conclude that we have reached the goal of converting a disorder-induced resonance to the resonance of a mode-gap cavity, since the mode does not become localized at the pump beam position. We also analyzed other disorder-induced resonances from the same waveguide. However, we did not see noticeable changes of the mode profiles and linewidths of in any of the other modes.

8.5 Outlook

From the experimental point of view, there are following things we can improve. First, increasing the scan range and making a two-dimensional scan can provide more information of the mode we have analyzed, such as how exactly the mode profile decreases. Second, due to the fact that we investigate a direct coupled waveguide and cavity system, we can only analyze the resonance spatially close to the access waveguide. A side coupled system will allow us to investigate a wider range of disorder-induced modes. Furthermore, reducing the effects of the surface water layer will allow us to measure the wavelength more accurately, and the relation between the wavelength shift and pump power can be quantified more accurately.

From the theoretical point of view, as far as we know, there is no numerical work which shows how a disorder-induced mode evolves into a resonance comparable to a mode-gap cavity. Thus, performing numerical simulations to elucidate this process is important.

Bibliography

- [1] K. J. Vahala, *Optical microcavities*, Nature **424**, 839 (2003). — p.95.
- [2] Y. Akahane, T. Asano, and B.-S. Song, *High- Q photonic nanocavity in a two-dimensional photonic crystal*, Nature **425**, 944 (2003). — p.95.
- [3] B.-S. Song, S. Noda, T. Asano, and Y. Akahane, *Ultra-high-Q photonic double-heterostructure nanocavity*, Nat. Mater. **4**, 207 (2005). — p.95.
- [4] E. Kuramochi, M. Notomi, S. Mitsugi, A. Shinya, T. Tanabe, and T. Watanabe, *Ultrahigh- Q photonic crystal nanocavities realized by the local width modulation of a line defect*, Appl. Phys. Lett. **88**, 041112 (2006). — p.95.
- [5] T. Tanabe, M. Notomi, E. Kuramochi, A. Shinya, and H. Taniyama, *Trapping and delaying photons for one nanosecond in an ultrasmall high-Q photonic-crystal nanocavity*, Nature Photonics **1**, 49 (2007). — p.95.
- [6] Y. Takahashi, H. Hagino, Y. Tanaka, T. Asano, and S. Noda, *High-Q photonic nanocavity with a 2-ns photon lifetime*, Conference on Quantum Electronics and Laser Science (QELS) - Technical Digest Series **15**, 17206 (2008). — p.95.
- [7] T. Yoshie, A. Scherer, J. Hendrickson, G. Khitrova, H. M. Gibbs, G. Rupper, C. Ell, O. B. Shchekin, and D. G. Deppe, *Vacuum Rabi splitting with a single quantum dot in a photonic crystal nanocavity*, Nature **432**, 9 (2004). — p.95.
- [8] H. J. Kimble, *The quantum internet*, Nature **453**, 1023 (2008). — p.95.
- [9] J. P. Reithmaier, G. Sek, A. Löffler, C. Hofmann, S. Kuhn, S. Reitzenstein, L. V. Keldysh, V. D. Kulakovskii, T. L. Reinecke, and A. Forchel, *Strong coupling in a single quantum dot-semiconductor microcavity system*, Nature **432**, 197 (2004). — p.95.
- [10] J. D. Joannopoulos, S. G. Johnson, J. N. Winn, and R. D. Meade , *Photonic Crystals: Molding the Flow of Light* (Princeton University Press, Princeton, 2008). — p.95, 96.
- [11] M. Notomi, K. Yamada, A. Shinya, J. Takahashi, C. Takahashi, and I. Yokohama, *Extremely large group velocity dispersion of line-defect waveguides in photonic crystal slabs*, Phys. Rev. Lett. **87**, 253902 (2001). — p.95, 97.
- [12] S. McNab, N. Moll, and Y. Vlasov, *Ultra-low loss photonic integrated circuit with membrane-type photonic crystal waveguides*, Opt. Express **11**, 2927 (2003). — p.95.
- [13] M. Notomi, E. Kuramochi, and T. Tanabe, *Large-scale arrays of ultrahigh-Q coupled nanocavities*, Nat. Photonics **2**, 741 (2008). — p.95.
- [14] K. Nozaki, A. Shinya, S. Matsuo, Y. Suzuki, T. Segawa, T. Sato, Y. Kawaguchi, R. Takahashi, and M. Notomi, *Ultralow-power all-optical RAM*

- based on nanocavities*, Nature Photonics **6**, 248 (2012). — p.95.
- [15] M. Notomi and H. Taniyama, *On-demand ultrahigh-Q cavity formation and photon pinning via dynamic waveguide tuning*, Opt. Express **16**, 18657 (2008). — p.95.
 - [16] E. Yüce, G. Ctistis, J. Claudon, E. Dupuy, R. D. Buijs, B. de Ronde, A. P. Mosk, J.-M. Gérard, and W. L. Vos, *All-optical switching of a microcavity repeated at terahertz rates*, Opt. Lett. **38**, 374 (2013). — p.95.
 - [17] S. Sokolov, J. Lian, E. Yüce, S. Combrié, G. Lehoucq, A. De Rossi, and A. P. Mosk, *Local thermal resonance control of GaInP photonic crystal membrane cavities using ambient gas cooling*, Appl. Phys. Lett. **106**, 171113 (2015). — p.95, 98.
 - [18] A. F. Koenderink, A. Lagendijk, and W. L. Vos, *Optical extinction due to intrinsic structural variations of photonic crystals*, Phys. Rev. B **72**, 153102 (2005). — p.97.
 - [19] S. R. Huisman, G. Ctistis, S. Stobbe, A. P. Mosk, J. L. Herek, A. Lagendijk, P. Lodahl, W. L. Vos, and P. W. H. Pinkse, *Measurement of a band-edge tail in the density of states of a photonic-crystal waveguide*, Phys. Rev. B **86**, 155154 (2012). — p.97.
 - [20] M. Spasenović, D. M. Beggs, P. Lalanne, T. F. Krauss, and L. Kuipers, *Measuring the spatial extent of individual localized photonic states*, Phys. Rev. B **86**, 155153 (2012). — p.97.
 - [21] L. Sapienza, H. Thyrrstrup, S. R. Stobbe, P. D. Garcia, S. Smolka, and P. Lodahl, *Cavity quantum electrodynamics with Anderson-Localized Modes*, Science **1027**, 1352 (2010). — p.97.
 - [22] M. Patterson, S. Hughes, S. Combrié, N.-V.-Q. Tran, A. De Rossi, R. Gabet, and Y. Jaouën, *Disorder-Induced Coherent Scattering in Slow-Light Photonic Crystal Waveguides*, Phys. Rev. Lett. **102**, 253903 (2009). — p.97.
 - [23] S. John, *Electromagnetic Absorption in a Disordered Medium near a Photon Mobility Edge*, Phys. Rev. Lett. **53**, 2169 (1984). — p.97.
 - [24] S. Combrié, Q. V. Tran, A. De Rossi, C. Husko, and P. Colman, *High quality GaInP nonlinear photonic crystals with minimized nonlinear absorption*, Appl. Phys. Lett. **95**, 221108 (2009). — p.97.
 - [25] N. Caselli, F. Intonti, C. Bianchi, F. Riboli, S. Vignolini, L. Balet, L. H. Li, M. Francardi, A. Gerardino, A. Fiore, and M. Gurioli, *Post-fabrication control of evanescent tunnelling in photonic crystal molecules*, Appl. Phys. Lett. **101**, 211108 (2012). — p.98, 100.
 - [26] F. Riboli, N. Caselli, S. Vignolini, F. Intonti, K. Vynck, P. Barthelemy, A. Gerardino, L. Balet, L. H. Li, A. Fiore, M. Gurioli, and D. S. Wiersma, *Engineering of light confinement in strongly scattering disordered media*, Nat. Mater. **13**, 720 (2014). — p.98, 100.
 - [27] C. J. Chen, J. Zheng, T. Gu, J. F. McMillan, M. Yu, G.-Q. Lo, D.-L. Kwong, and C. W. Wong, *Selective tuning of high-Q silicon photonic crystal nanocavities via laser-assisted local oxidation*, Opt. Express **19**, 12480 (2011). — p.100.

CHAPTER 9

Summary

In this thesis, theoretical, numerical and experimental studies of the resonances in photonic crystal waveguides are presented. These resonances originate from intended defects or unavoidable disorder, and they appear near the band edge of the photonic crystal waveguide.

To model light transport in a large scale couple resonator optical waveguide (CROW), we choose the multi-scale modeling (chapter 2) which is the most efficient way. It unifies microscopic modeling performed by the finite difference time domain (FDTD) method and device scale modeling with a coupled mode model. With the help of the model, we are able to optimize the transmission and delay spectrum of a larger scale CROW. In the process of the microscopic modeling for mode-gap cavities, we realize the dispersive nature of the mode profiles (chapter 3). To understand the physics and create a more accurate but efficient model, we have developed our dispersive mode (DM) model which accurately describes the dispersion without introducing any new parameter.

The characterization of the resonances in photonic crystal waveguides is done by reflection and transmission measurements (chapter 6, 7). The characterization brings surprises and stimulates our understanding. In reflection measurements, the observed Fano asymmetric lineshapes pushed us to develop a model to understand and reproduce the measured spectra. The very successful model makes us realize the lensed fiber as a measurement device plays a vital role in controlling the lineshapes. In transmission measurements, the unexpected high TM (transverse magnetic)-like signal on cavity resonances stimulates us to create a model to explain the possible physical process. Combing model and experimental data, we conclude that TE (transverse electric)/TM conversion is a substantial loss channel for cavity resonances.

In the experiment of controlling the disorder-induced resonances in photonic crystal waveguide (chapter 4, 5, 8), we realized that the same tool can be used as a probe for the mode profiles, and it is a probe which does not perturb the nanostructure. The first demonstration is done in the regime where the first order perturbation theory is valid. Later (chapter 5), we extend the possibility of this method, and make it work in the regime where the first order perturbation theory is invalid. Curiosity to observe the process of pulling a defect mode from continuum made us perform the experiments in chapter 8. Although we can not conclude that we reach that goal, we do observe amazing phenomena such as one order of increase of the Q of a disorder-induced mode, and the increase of the confinement of this mode in the direction transversal to the waveguide.

The experiments and models shown in the thesis improve our understanding of light transport in coupled photonic crystal waveguides and cavities. As powerful tools, the models can be directly applied to improve the experimental characterization and sample design. The dispersive mode (DM) model shown in the thesis can improve the design of CROWs composed of photonic crystal cavities with shallow defects. The methods presented to control and probe the disorder-induced resonances in photonic crystal waveguides constitute an essential step towards engineering functional devices in disordered photonic systems. The work shown in this thesis represents a step towards fully programmable nanophotonic circuits based on coupled resonances.

Algemene Nederlandse samenvatting

In dit proefschrift presenteren we theoretische, numerieke en experimentele studies naar resonanties in fotonische kristal golfgeleiders. Deze resonanties zijn het gevolg van geplande defecten en onvermijdelijke wanorde, en verschijnen nabij de bandkloof van de fotonische kristal golfgeleider. Voor het modelleren van lichttransport in een grootschalige coupled resonator optical waveguide (CROW) [gekoppelde resonator optische golfgeleider (GROG)], gebruiken we een multischaalmodel (hoofdstuk 2), de meest efficiënte methode. Deze methode verenigt het modelleren op een microscopische schaal in de vorm van de zogenaamde finite difference time domain (FDTD) methode met apparaat-schaal modelleren in de vorm van een coupled mode model. Met behulp van dit model zijn we in staat het transmissie- en vertragingssspectrum van een grootschalige CROW [GROG] te modeleren. Tijdens het microscopisch modelleren van resonatoren dichtbij de bandkloof, ontdekten we dat het veldprofiel van deze resonatoren dispersief is (hoofdstuk 3). Om de fysica te begrijpen en een accurater maar efficiënt model te maken, hebben we het dispersieve toestand (DT) model ontwikkeld, dat de dispersie accuraat beschrijft zonder introductie van nieuwe parameters.

De resonanties in de fotonische kristal golfgeleiders zijn gekarakteriseerd met behulp van reflectie- en transmissiemetingen (hoofdstuk 6,7), met verassende en inzichtelijke resultaten. De observatie van asymmetrische Fano resonanties bracht ons tot het ontwikkelen van een model om de gemeten spectra te reproduceren en begrijpen. Door dit succesvolle model realiseerden wij ons dat het gebruik van zogenoemde lensed fibers als meetinstrument van fundamenteel belang is voor het controleren van de resonantie. Het meten van een onverwacht hoog signaal met een onverwachte polarisatie toestand in het transmissie spectrum van resonatoren heeft ons gestimuleerd tot het maken van een fysisch model om het gedrag te beschrijven. Uit de combinatie van het model en de experimentele data concluderen we dat de omzetting van licht in transversaal magnetische toestanden naar licht in transversaal elektrische toestanden een significante verliester geeft.

In ons experiment voor het beheersen van de normaal trillingen van het licht in de fotonische kristal golfgeleider (hoofdstuk 4, 5, 8) realiseerden wij ons dat een vergelijkbare methode gebruikt kan worden om het veld van de normaal trillingen te meten, zonder de nanostructuur te verstören. De eerste demonstratie is gedaan in het regime van eerste orde storingsrekening, en later (hoofdstuk 5) breiden we de methode uit tot het regime waarin eerste orde storingrekening niet meer geldig is. Een experiment gericht op het observeren van het lostrekken van een imperfectie toestand uit het continuüm is beschreven in hoofdstuk 8. Hoewel we niet kunnen concluderen dat we dit doel behaald hebben, zien we wel

een verhoging van de Q van een orde van grootte voor de wanorde geïnduceerde toestand en vergroten we de opsluiting van de toestand in de richting transversaal tot de golfgeleider.

De experimenten en modellen uit dit proefschrift verbeteren ons begrip van het transport van licht in gekoppelde fotonische kristallen golfgeleiders en trilholtes. De modellen kunnen direct worden toegepast voor het verbeteren van de experimentele karakterisatie en voor het ontwerp van nieuwe samples. Het dispersieve toestand (DT) model, beschreven in dit proefschrift kan het ontwerp verbeteren van CROW/GROG's opgebouwd uit fotonische kristal resonatoren met resonanties nabij de bandkloof. De gepresenteerde methode voor het beheersen en meten van door wanorde geïnduceerde resonanties vormt een essentiële stap in de ontwikkeling van functionele apparaten in wanordelijke fotonische systemen. Het werk in dit proefschrift is een stap naar volledig programmeerbare nanofotonische schakelingen gebaseerd op gekoppelde resonanties.

Acknowledgments

Oscar Wilde says “There are only two tragedies in life: one is not getting what one wants, and the other is getting it”. This is one of the quotes that I could not agree with more, and I would rephrase it as “There is only one happiness: one is always close to getting what one wants”. The four years of being a PhD student is the way I obtained this happiness, because it taught me how should I identify the way of being close to getting what I want and find out the next exciting thing which I can again enjoy the feeling of being close to. The experience of these four years would not have been complete without the people who shared their lives with me and helped me on enjoying this happiness.

I would first like to express my deepest thanks to my supervisor Allard Mosk. I am very lucky that I could carry out my PhD research under his supervision. I am amazed by his vast knowledge and deep understanding of theory, experiments and numerics, and I am glad that under his supervision I managed to finish a thesis that covers all these aspects. Being his student, one experiences a very luxurious research life: luxurious in the sense that he is always willing to spare time from his busy schedule for scientific discussions which he cannot resist because of his enthusiasm for physics; luxurious in the sense that there are always many ideas generated during these discussions; luxurious in the sense that he spends a great effort on explaining physics in an intuitive and direct manner by making many cartoons and animations himself; luxurious in the sense that he gives freedom to his students to perform research which fulfills their curiosities; luxurious in the sense that his critical comments are always accompanied with compassion for his students.

I am very grateful that I had opportunities during these four years to receive invaluable advice and learn from the world-class scientists, especially: Willem Vos, Ad Lagendijk, Pepijn Pinkse, and Klaus Boller. I acknowledge their willingness to share their experiences and wisdom with me. I started to learn from Willem as early as during my interview at COPS. In these years, he made me remember that being a good physicist is not only about doing great research, but it is also about being able to present results in a clear and accurate manner and being professional in every aspect. I received many critical comments and brilliant advice from Ad and Pepijn during group meetings and coffee breaks which contributed to indispensable steps of my personal development. I also had many intriguing discussions with Klaus during the coffee breaks and the ANP meetings.

I wish to express my sincere gratitude to my committee members Willem Vos, Klaus Boller, Claudia Conti, Alfredo de Rossi and Ewold Verhagen for reading

my thesis, evaluating and giving valuable feedback which greatly improved the content of my thesis.

I am very glad that I could join one of the few projects in the group which really started from scratch. I enjoyed experiencing the process of going from an empty optical table to an extremely complicated optical setup. This fantastic experience would not have been possible without the intelligence and efforts of Sergei Sokolov. The time Sergei and I spent in the lab and office is very precious for me since I learned a lot from his criticism and persistence. In the second half of my PhD, it was great that Emre Yüce joined our project as a postdoc, and I was surprised that even after two years of being office mates, there were still many things I learned from him.

My research project received powerful support from our collaborators Alfredo De Rossi and Sylvain Combrié, and successful results would not have been possible without their input, creative ideas and invaluable samples.

I feel very fortunate that there are always brilliant postdocs and young staff members who are willing to share their expertise. In Enschede, they were Henri Nielsen and Ravitej Uppu and I do not remember how many times I just interrupted them with the problems I encountered when they were busy. However, I do remember that they were very patient on almost every occasion and showed a great deal of interest to discuss with and help me. Henri is one of the most altruistic persons I have met, who selflessly contributed to most of the projects of his colleagues with his broad theoretical, experimental and numerical knowledge. Ravi, who joined the group much after Henri, became extremely popular among PhD students due to his kindness and intelligence. In Utrecht, I am glad that Sanli Faez is around. Besides his talent in research, I also have benefited from his talent on decision making and several other things.

It is great that I shared the office with Bas Goorden when I started my PhD. The funny thing is that during discussions with him I from the physics background always like to write equations, whereas Bas from the mathematics background always like to draw pictures. I would like to thank Hasan Yimaz, accompanied by his famous and loud laughter, with whom many funny moments occurred. The wonderful friend Diana Grishina, who organized a memorable surprise birthday party for me, is always so kind. I would like to thank Yin as a Chinese colleague who made my adaptation to the life of UT and Enschede a lot easier.

In these four years, I had great fun discussing science and other interesting non-scientific topics with my colleagues, and especially received precious feedback and remarks from them: Amandev, Andreas, Bill, Dashka, Devashish, Duygu, Elahe, Evangelos, Femi, Georgios, Ivo, Jacopo, Jan, Jochen, Lyuba, Maryna, Michael, Shakeeb, Simon, Sina, Thomas, Tom, Timmo, Tristan, Vanessa and Willem Tjerkstra. Outside the group, I learned a lot from the discussions with Jennifer, Jeroen from OS, Caterina Taddei, Caterina Taballione, Peter, Jesse, Jörn and Youwen from LPNO, Dries and Peter from Nanophotonics UU.

I acknowledge Cock Harteveld for his solid support on technical issues in the lab and for his help on teaching me how to handle the issues I experienced in daily life as a foreigner. I also acknowledge Marlon Gompert for his help on computer

related issues, which is always fast and effective. I acknowledge Nilda, Nienke and Jacqueline for their assistance on paperwork, and their help simplified my PhD life a lot. I also would like to thank Cees, Dante, Floor and Paul for all the help I received after I moved to Utrecht.

I would especially like to thank Jeroen Bosch for the Dutch summary of my thesis, Pritam Pai for the improvement of the English of my thesis, Daniel Cox for showing me the techniques of Blender, and my friend Yiwei Zeng for the cover design.

Finally, I would like to thank my family for their love and support. 爸, 妈, 感谢您二位的养育之恩, 您二位几十年来的辛苦付出, 是我前进路上最坚强的后盾. 老婆, 感谢你这么多年来为我所做的牺牲, 我坚信在我们的努力下, 未来会更加美好.

- Jin